CHAPTER 8

The Quantum Chemistry of Loosely-Bound Electrons

John M. Herbert

Department of Chemistry and Biochemistry, The Ohio State University, Columbus, OH 43210, USA

INTRODUCTION AND OVERVIEW

What Is a Loosely-Bound Electron?

By some measure, the title of this chapter could have been "The quantum chemistry of weakly-bound anions," because much of it will focus on how to describe the weak binding of an "extra" electron to a stable, neutral molecule using electronic structure theory. Electron binding energies in such cases may be quite small, typically less than the largest *atomic* electron affinities (EAs)[1] (3.4 eV for F and 3.6 eV for Cl), and even less than 0.1 eV in some cases. Unlike the case where a neutral molecule, M, is ionized, an electron separated from the anion M^- does not experience an attractive $-1/r$ potential at large separations,[2,3] but rather only charge–dipole and or higher order charge–multipole interactions. Cases where the electron affinity of M is $\lesssim 0.5$ eV are the signature of a short-range valence potential that is weakly attractive at best, such that electron binding in M^- results primarily from long-range electron–molecule, charge–multipole interactions. In such cases, one expects to find an unpaired electron in M^- that is radially diffuse, much more so than in F^- or Cl^-, for example. It is in this sense that the odd electron in M^- is "loosely-bound." Moreover, the preceding discussion assumes that M^- is bound at all, but in fact we will also consider cases in which the electron

Reviews in Computational Chemistry, Volume 28, First Edition.
Edited by Abby L. Parrill and Kenny B. Lipkowitz.

is adiabatically *unbound* (higher in energy than $M + e^-$), but where the species M^- can exist as a *temporary anion resonance*, trapped behind some energy barrier that often originates from the centrifugal potential required to conserve angular moment when removing an electron from an orbital with $\ell > 0$.

We will further broaden our definition of what constitutes a loosely-bound electron to include a discussion of *solvated electrons*, which one might define as cluster anions M_N^- where the odd electron is bound collectively by the solvent molecules, insofar as the anion M^- of a single solvent molecule is not a bound species. In a small cluster, M_N^- might be weakly-bound, but depending on the number (N) and nature of the solvent molecules, the electron binding energy of M_N^- can sometimes be quite large, up to a few eV in some cases. This is still much smaller than the ionization energy of the neutral cluster M_N, and in this sense the "extra" electron may still be considered to be weakly-bound. As a definite example, consider the case $M = H_2O$. Vertical electron binding energies in $(H_2O)_N^-$ clusters, as measured by photoelectron spectroscopy, can exceed 2 eV for $N \gtrsim 100$,[4,5] and the best estimates in the bulk limit ($N \to \infty$) lie in the range of 3.3–4.0 eV.[5−10] Insofar as H_2O^- is not bound,[11] however, the unpaired electron cannot be said to be associated to any one particular water molecule and is thus "loosely-bound."

As another example of what we have categorized, for the purpose of this chapter, as loosely-bound electrons, we will consider excited electronic states of anions that possess enough energy to access an electronic continuum, or in other words, excited states where the excitation energy is greater than the electron detachment energy. Such states exist, if at all, only as temporary, "auto-ionizing" resonances. Other temporary anion resonances (viz, shape resonances and Feshbach resonances) will be explained and discussed as well. These temporary anion resonances are chemically important in the context of *dissociative electron attachment* (DEA),[12] in which resonant attachment of low-energy electrons is followed by internal conversion to a state where covalent bond dissociation is energetically feasible. DEA provides a mechanism wherein energy barriers that would be thermodynamically insurmountable on the Born–Oppenheimer potential surface for $M + e^-$ are bypassed by means of nonadiabatic transitions, leading to molecular fragmentation in the presence of electrons whose kinetic energies are "just right."

Scope of This Review

Each of the aforementioned phenomena presents special challenges for quantum chemistry, and the methods required to meet these challenges are the primary topic of this chapter. In addition, this chapter provides a discussion of the basic quantum mechanical concepts that underlie the collection of phenomena that this author has categorized as "loosely-bound electrons." A limited discussion of some of the interesting chemical systems that fall under this moniker is provided as well, although this chapter is not intended

to be a comprehensive review of the field of weakly-bound anions, solvated electrons, or anything else. Several excellent topical reviews have appeared in the past few years, to which the reader is referred for a thorough discussion of the chemistry. These include a comprehensive 2008 review of the whole field of molecular anions (experiment as well as theory),[2] and a more recent review focused on theoretical calculations.[3] Reactions induced by low-energy electrons have also been thoroughly reviewed in the past few years, including several general overviews of electron-induced reactions,[12–14] a review of biological radiation chemistry and the role of "presolvated" electrons in biological radiation damage,[13] and a review of electron attachment (EA) to DNA, focusing on electronic structure calculations.[14] Solvated electrons, both in clusters and in bulk liquids, have been reviewed recently from both a theoretical perspective[15,16] and an experimental perspective.[17–19]

This work is intended as an introduction to these topics and a tutorial guide to performing quantum chemistry calculations intended to model these types of molecular systems and phenomena. The focus here is on methods that are readily available in standard quantum chemistry software packages and thus, for example, we will discuss the calculation of resonance states using modifications of *bound-state* methodology,[20] since bound states are what one computes in traditional quantum chemistry. Alternative formalisms such as scattering theory[21–26] or the explicit treatment of the interaction of a discrete state with a continuum state[27,28] will not be discussed here. The use of complex absorbing potentials[29–31] is discussed only briefly.

Our discussion of electronic structure calculations is further limited to methods based on Gaussian basis sets rather than plane waves. This restriction is partly a matter of taste, and in fact one can make a good case that a plane-wave basis is better suited for representing the most diffuse parts of a weakly-bound anion's electron density, as compared to a basis comprised of localized, atom-centered functions. However, a more important concern (in this author's view) is the fact that Hartree–Fock exchange is prohibitively expensive to compute in a plane-wave basis. Although significant progress has been made in this respect,[32] the cost remains prohibitive unless the nonlocal exchange interaction is screened at long range.[33,34] As a result, the hybrid functionals that provide the best performance for many molecular properties are ordinarily not available in plane-wave density functional theory (DFT) calculations, which proves particularly egregious in the case of weakly-bound anions. Correlated, post-Hartree–Fock wave functions are similarly unavailable in most plane-wave codes, which is another reason to dismiss plane waves in the present context.

As the title of this chapter suggests, the discussion here is limited, for the most part, to *loosely* bound electrons, meaning that valence ionization is not considered to any significant extent. It is important to keep in mind, however, that "loosely-bound" need not mean "weakly-bound." As mentioned earlier, vertical electron detachment energies in excess of 1–2 eV are possible even

in solvated-electron clusters where the "extra" electron is not strongly associated with any particular molecular unit or chemical moiety. That said, the quantum chemistry of weakly-bound, gas-phase anions is certainly discussed herein, at a somewhat more pedagogical level as compared to previous reviews on that subject.[2,11,35] An exception is that Refs. 2 and 37 describe the underlying theory behind various post-Hartree–Fock quantum chemistry models, material that is not covered here at all (it has been covered in previous chapters in this series[36,37]). This review assumes a basic familiarity with the nomenclature of quantum chemical models and basis sets, at the level of introductory textbooks[35,38,39] or previous chapters in this series.[36,40,41] The performance of a variety of quantum chemical models, as applied to weakly-bound anions, is addressed in detail, but the inner workings of these models is not discussed here.

A unique feature of this chapter, as compared to other reviews of anion quantum chemistry that have appeared in the past decade,[2,11,42] is a greater emphasis on treating larger systems, including anions in the condensed phase. In large systems, compromises must inevitably be made in terms of the theoretical methods that can be deployed. As such, density functional methods – which have hardly been discussed at all in previous reviews of anion quantum chemistry, except briefly in Ref. 2 and in a benchmarking capacity in Ref. 43 – are discussed at length here. Previous chapters in this series provide an introduction to DFT itself,[40,41] but the focus here is on the performance of the models, not their intimate details. There has been some controversy regarding the applicability of DFT to anions,[44–46] however, which will require delving into a bit of detail.

Finally, this chapter covers not just bound-state methods but also methods that can safely be applied to *metastable* anions (i.e., temporary anion resonances), which is a far less mainstream topic.[20] For metastable anions, the emphasis of this chapter is on those methods that have been implemented in standard quantum chemistry codes and are therefore widely available to the chemistry community.

Chemical Significance of Loosely-Bound Electrons

Weakly-bound anions with electron detachment energies < 0.1 eV can be produced and detected experimentally.[2,11] At some level, it is tempting to be cynical about the significance of an anion M^- whose electron detachment energy is that small, since excitation of any vibrational mode with $\tilde{\nu} \gtrsim 800$ cm^{-1}, or some combination of rotational and or vibrational excitations adding up to ~ 800 cm^{-1}, provides enough energy to detach the electron, depending on how the modes in question couple to the weakly-bound electron and modulate the electron binding energy.[47–49] However, there are other possible fates for M^- that are more interesting, such as a nonadiabatic transition into a different anion electronic state.

Anions that are formally unbound but metastable can be chemically important. These *temporary anion resonances* are discussed in detail later

in this chapter, but a pictorial illustration of one important case is provided in Figure 1. In this particular example, the energy of the anion AB^- lies above that of neutral AB at the geometry of the latter. However, an incident electron with appropriate kinetic energy can attach (into a virtual orbital of AB) to form AB^-, but the energy of the anion that is formed lies above the dissociative asymptote of AB^-. This is an example of DEA.[12] Experimentally, this temporary anion resonance manifests as a yield of ions B^- and radicals $A^\bullet$ for incident electron energies that lie within a certain range that is defined by the Franck–Condon envelope of AB's wave function projected onto the AB^- potential surface. The thermodynamic driving force for DEA is often the large electron affinity of the B moiety, as suggested in Figure 1.

From the standpoint of radiation chemistry, DEA reactions such as these are classified as low-energy electron-induced reactions,[12,13,50] since they are driven by "secondary" (subionizing) electrons with $E < 15$ eV, rather than the fast "primary" electrons that have enough kinetic energy to generate molecular ions directly. An excellent recent overview of low-energy electron-induced reactions, from an experimental perspective, can be found in Ref. 12. One key feature of electron-induced reactions is high selectivity for cleavage of specific bonds, which need not be (and often are not) the thermodynamically weakest

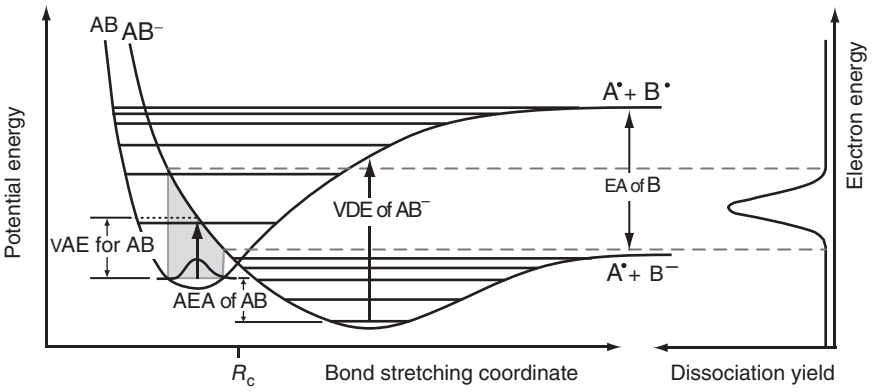

Figure 1 Schematic representation of a temporary anion resonance leading to dissociative electron attachment. Within the Franck–Condon envelope of the neutral molecule AB (shaded region), electron attachment is possible if the incident electron has an energy that matches the vertical attachment energy (VAE), equal to $E(AB^-) - E(AB)$. On the AB^- potential surface, the temporary anion possesses sufficient energy to dissociate to $A^\bullet + B^-$, and this manifests as an observed yield of products ($A^\bullet$ or B^-) in the energy window defined by the Franck–Condon envelope. (The vertical energy scales at the left and right are the same, so that the potential surfaces map directly onto the observed dissociation yield.) Important energetic quantities are indicated, including the VAE and the adiabatic electron affinity (AEA) of the molecule AB, the vertical detachment energy (VDE) of AB^-, and the electron affinity (EA) of species B. The last is the driving force, chemically speaking, that stabilizes the AB^- potential surface relative to that of AB. Adapted with permission from Ref. 12; copyright 2010 Elsevier.

bonds in a polyatomic molecule, owing to details of the nonadiabatic nature of the electron-induced reaction. This fact has been exploited in proof-of-concept experiments that use DEA to break selected chemical bonds with 100% selectivity,[51] and single-molecule specificity,[52,53] for molecules adsorbed on a solid substrate. (In these particular experiments, the reagent electrons were generated using the tip of a scanning tunneling microscope.) A longer list of examples and potential applications of reactions induced by low-energy electrons can be found in Ref. 12.

Chlorofluorocarbons (CFCs) tend to have large cross sections for DEA, owing to the large EAs of the halogen atoms, and have been common targets for laboratory studies of DEA. The DEA cross sections for CFCs are enhanced further still by several orders of magnitude relative to gas-phase values, for DEA occurring at the surface of water ice.[54–57] Laboratory experiments consist of adsorbing, for example, $CFCl_3$ at low-surface coverage onto a thin film of ice prepared on a metal substrate; solvated electrons at the ice/vacuum interface are subsequently generated by photoexcitation of the metal.[55,58,59] The reaction $CFCl_3 + e^- \rightarrow {}^{\bullet}CFCl_2 + Cl^-$ is observed even at very low surface coverage of $CFCl_3$,[55,59] suggesting a highly efficient reaction. Absent the CFC, the photogenerated electrons in these experiments are found to be stable for *minutes* at the ice/vacuum interface.[60] (For comparison, solvated electrons generated by radiolysis of bulk liquid water survive for only about 10 μs,[61] owing to fast diffusion and a variety of recombination reactions with other radiolysis byproducts.[62])

In view of this, it has been proposed that hydrated electrons generated on the surface of stratospheric ice crystals, via cosmic rays, could contribute to Cl^- formation via DEA of adsorbed CFCs.[54,56] Photodetachment of the chloride ions might then provide a mechanism to generate the Cl radicals that lead to ozone destruction. However, attempts to link these laboratory observations directly to stratospheric ozone chemistry have been strongly criticized,[63–71] although modeling does leave open the possibility that, at the very least, HCl destruction on ice crystals might be important for stratospheric chlorine chemistry.[67] More work is evidently needed to resolve this controversy.

A slight variant on the DEA picture introduced in Figure 1, but one worthy of mention in its own right, is the possibility of long-range electron capture in the gas phase into a Rydberg-type orbital of some molecule. Suppose that our molecule, M, consists of two different functional groups connected by a single bond, $M = R_1—R_2$. If an electron initially attaches to the molecule $R_1—R_2$ via some unoccupied (virtual) molecular orbital (MO) associated with the R_1 moiety, but subsequently tunnels into a σ^* orbital associated with the $R_1—R_2$ bond, then the net effect is to reduce the formal bond order for $R_1—R_2$. It may then be the case that the anion is no longer a bound state with respect to dissociation along the $R_1—R_2$ bond. The process in question can be written

$$R_1 - R_2 + e^- \rightarrow (R_1 - R_2)^- \rightarrow R_1^- + R_2^{\bullet} \qquad [1]$$

Assuming that the products $R_1^- + R_2^\bullet$ are lower in energy than the reactants ($R_1 - R_2$ plus an infinitely separated electron), then the intermediate species $(R_1 - R_2)^-$ is a temporary anion resonance, since the bound-state configuration of moieties R_1, R_2, and an extra electron is $R_1^- + R_2^\bullet$, not the anion $(R_1 - R_2)^-$. Whether reaction [1] will occur in practice depends sensitively on the barrier(s) and nonadiabatic couplings involved in the second step (nonadiabatic transition to the dissociative σ^* state), as well as the energy of the incident electron, which controls whether the temporary anion resonance can be accessed or not.

In the case of weakly-bound anions, we note that if the electron binding energy of M^- is very small, then the unpaired electron is bound very diffusely, so that it may, on average, be well-separated from the molecular core, M. This scenario is unlikely to occur except in the gas phase, where M^- is well separated from other molecules. Long-range electron capture into Rydberg orbitals, to form very weakly-bound gas-phase anions, is the mechanism that underlies the techniques known as *electron capture dissociation*[72] and *electron transfer dissociation*[73] that are used for protein sequence analysis via mass spectrometry. In these methods, capture of low-energy electrons by highly protonated, gas-phase polypeptides leads to highly specific fragmentation patterns, with cleavage of disulfide bonds and $N-C_\alpha$ bonds as the dominant fragmentation channels. Simons and coworkers[74–78] have performed quantum chemistry calculations in an attempt to understand the mechanism(s) behind this specificity, and the potential energy curves shown in Figure 2 illustrate the DEA phenomenon. In these calculations,[74] the molecule is actually a cation (consistent with the aforementioned experiments), namely, $M^+ = H_3CS—S(CH_2)_2NH_3^+$. EA directly to the $\sigma^*(S - S)$ orbital is energetically feasible at the parent cation's geometry, with a resulting potential curve that is indeed dissociative along the S—S coordinate. However, the cross section for this direct attachment process is found to be small. Instead, EA to excited Rydberg states of the $—NH_3^+$ moiety appears to offer a substantially enhanced cross section that also ultimately results in S—S dissociation, via a DEA mechanism.[77]

Moving from the gas phase into solution, there is evidence that very low-energy electrons can damage DNA,[79–81,13] via a DEA mechanism somewhat analogous to that discussed earlier.[82,83] In this context, "low energy" means electrons whose kinetic energies are less than the ~4 eV bond energies of the single bonds that are ruptured in DNA single-strand breaks. (In the context of radiation chemistry, electrons in the range 0–20 eV are typically classified as "low-energy" electrons, since this is the energy distribution of secondary electrons formed from primary ionization events,[84,13] but here we are focusing on the low end of this range.) Experimental studies of very low-energy ($E < 3$ eV) EA to gas-phase nucleobases show high site selectivity in the ion yields. For example, in thymine and uracil, there is a resonance around $E \approx 1$ eV corresponding to the dissociation of the N1—H bond (where the base would attach to the sugar in DNA) and a somewhat higher energy

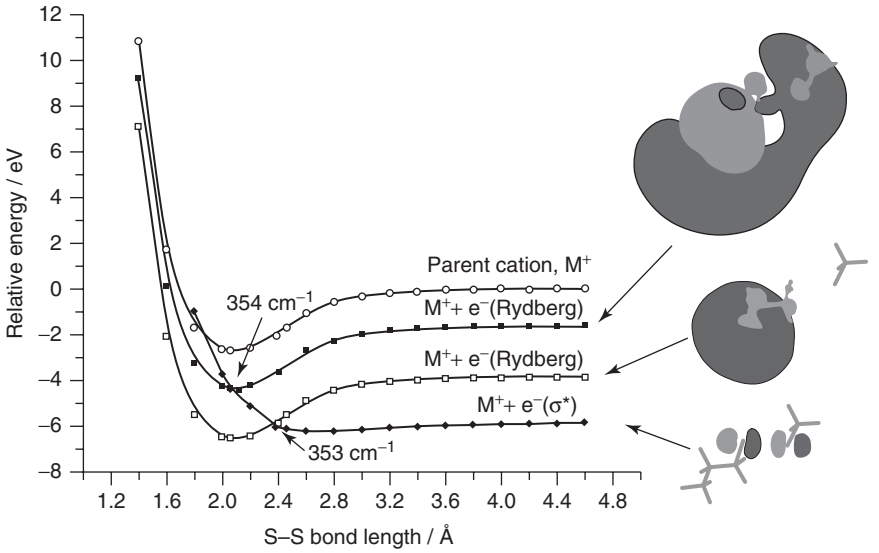

Figure 2 Potential energy curves along the S—S coordinate, for the protonated model peptide $M^+ = H_3CS—S(CH_2)_2NH_3^+$ and electron-attached states thereof. Shown are states in which the electron attaches to either of two different Rydberg orbitals localized on the $—NH_3^+$ moiety and the state that results from direct e^- attachment to the σ^*(S—S) orbital. Orbital isosurfaces were computed at $R = 3.6$ Å and contain 60% of the orbital density in each case. Estimated nonadiabatic couplings between the Rydberg states and the σ^* state are shown as well. Adapted with permission from Ref. 74; copyright 2006 Elsevier.

resonance corresponding to N3–H dissociation. Notably, the former is absent when the N1 site is methylated,[85] or even deuterated,[86] suggesting that the lowest energy electrons might generate H atoms in DNA, but would not lead directly to the loss of the nucleobase.

A mechanism for single-strand breaks induced by electrons with $E \lesssim 2$ eV has been proposed by Simons[82] on the basis of theoretical calculations. The first step is formation of a temporary anion resonance involving electron capture by a π^* orbital of the nucleobase to form an anion radical, $(\text{nucleobase})^{\bullet-}$. Subsequently, the anion may undergo a nonadiabatic transition to a dissociative σ^* state involving a sugar–phosphate C—O bond,[82,14] and theoretical estimates of the nonadiabatic transition rate suggest that this process is feasible within the lifetime of the temporary anion resonance.[75,77,74,78] This mechanism is consistent with experimental results for gas-phase deoxyribose, in which near-zero kinetic energy electrons were found to dissociate C—O bonds of the sugar.[87] However, direct experimental identification of these putative $(\sigma^*)^-$ temporary anion resonances remains debatable,[21,88,23,26,89] because they tend to have shorter lifetimes as compared to $(\pi^*)^-$ resonances and are thus subject to a greater degree of lifetime broadening.

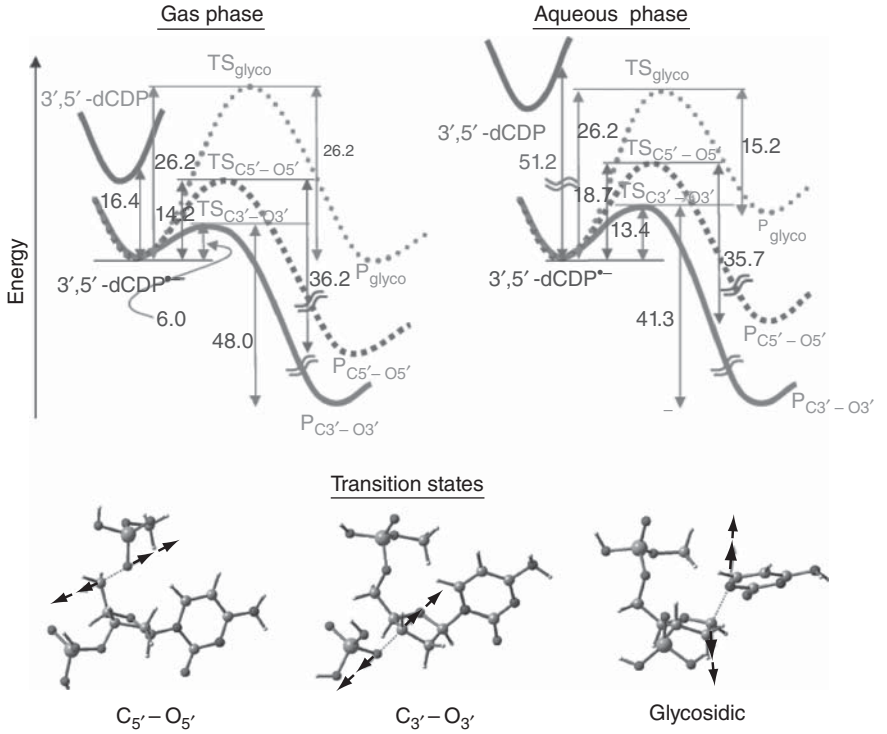

Figure 3 Pathways for three possible single-strand breaks in the radical anion of 2′-deoxycytidine-3′,5′-diphosphate, dCDP$^{•-}$. The upper panels show computed minimum-energy pathways in the gas phase and in a polarizable continuum model of aqueous solvation, while the lower panels depict the calculated transition states corresponding to rupture of the 5′ sugar—phosphate C—O bond, the 3′ sugar—phosphate C—O bond, or the glycosidic C—N bond, with arrows to emphasize the direction of bond scission. Adapted with permission from Ref. 90; copyright 2010 Oxford University Press.

Figure 3 shows some computed minimum-energy pathways for single bond ruptures in the radical anion of the nucleoside deoxycytidine diphosphate, dCDP$^{•-}$.[90] Pathways leading to dissociation of either the 3′ or the 5′ sugar–phosphate C—O bond, and also the glycosidic C—N bond, have been located, but the computed energetics suggest that the latter pathway is inaccessible with the energy available from forming dCDP$^{•-}$ from its dCDP precursor. The lower barrier of the 3′ pathway relative to the 5′ pathway and the high barrier to C—N bond cleavage are all qualitatively consistent with experimental studies in which DNA was bombarded by electrons in the 6–15 eV range.[80,81] In those experiments, the relative yield of 3′ cytidine strand breaks to 5′ strand breaks increased significantly as the energy of the incident electrons was decreased, and products corresponding to glycosidic bond cleavage were not detected.[80,81]

A possible precursor for DEA reactions occurring in condensed media is the solvated electron, and as such this species (in various solvents, but especially water) has been studied extensively.[91,17,18,15,16,13] Solvated electrons are generated in high yield by radiolysis of the solvent,[13] but are also generated by photoionization of common UV chromophores such as indole,[92] the chromophore in tryptophan. In that case, geminate recombination of the ion pair (a solvated electron and an indole cation radical) is slower than the diffusion limit,[92] such that these photogenerated solvated electrons may have a chemical role to play in solution-phase photochemistry. In the gas phase, finite cluster analogues of the solvated electron serve as interesting model systems for understanding how a solvent accommodates an excess charge.[93–95,16,19]

Challenges for Theory

Systems containing loosely-bound electrons pose special challenges for electronic structure calculations that are absent in calculations of cations, neutral molecules, or even strongly-bound valence anions. For an anion, separation of an electron from the molecular framework leaves behind a charge neutral molecule or radical, so that an "outgoing" electron does not feel a $-1/r$ Coulomb potential, as it would were an electron removed from a neutral molecule, leaving a cationic core. Rather, the long-range electron–molecule potential decays as $-1/r^2$ (charge-dipole) or faster.[2,3] The result, which is discussed quantitatively later in this chapter, is that the anion's electron density is significantly more diffuse as compared to that of a neutral molecule or cation. This is true for strongly-bound anions as well as weakly-bound ones, but the radial extent of the electron density increases exponentially as the electron binding energy decreases. This places special demands on the basis sets that are used to describe weakly-bound anions.

In addition, for a weakly-bound anion it may be necessary to consider the possibility that the molecule's vibrational motion could access regions of the potential energy surface where the anion is no longer thermodynamically stable with respect to electron ejection (autodetachment). For weakly-bound anions in the gas phase, autodetachment induced by rotational motion may also need to be considered.[2]

In terms of the level of electronic structure theory that is required, calculation of EAs, or, in other words, electron detachment energies for anions, tends to be more demanding than calculation of ionization potentials (IPs), if for no other reason than that the former tend to be smaller in magnitude than the latter. As evidence for this, one need look no further than the periodic table: atomic EAs are bounded above by that of chlorine, at 3.6 eV,[1] whereas atomic IPs range from 5.4 eV for Li up to 17.4 eV for fluorine and larger still for the noble gases.[96] A few examples for atoms and small molecules are shown in Table 1, illustrating that IPs tend to be $\gtrsim 8–10$ eV whereas EAs are typically ~ 3 eV. (Even for molecules, a comprehensive review of experimental EAs from photoelectron spectroscopy reveals only a very few examples larger than 4–5 eV.[43])

Table 1 Experimental Adiabatic Electron Affinities (AEAs) and Ionization Potentials (IPs) for Some Atoms and Small Molecules[a]

	IP (eV)	EA (eV)		IP (eV)	EA (eV)		IP (eV)	EA (eV)
C	11.26	1.26	OH	12.97	1.83	S_2	9.37	1.70
Cl	12.97	3.62	P	10.49	0.75	SH	10.36	2.31
Cl_2	11.50	2.41	PH	10.15	1.01	Si	8.15	1.38
O	13.61	1.46	PH_2	9.81	1.27			
O_2	12.09	0.47	S	10.36	2.08			

Reprinted with permission from Ref. 97; copyright 2003 American Chemical Society.
[a]This is the "EA13/03" database of Ref. 97 and estimated vibrational zero-point energies have been removed from the experimental data.

Moreover, EAs are *intensive* quantities, as are IPs, whereas both the total electronic energy and the correlation energy are extensive. Thus, as molecular size increases the EA that one is attempting to calculate represents a diminishing fraction of the total energy.[98,99,2] Simons[2] has used this fact to argue in favor of the so-called *equation-of-motion* (EOM) methods[98,99] (also known as *Green's function*[100] or *electron propagator*[101−104] methods), in which EAs and IPs are computed directly, in a single calculation, not evaluated as an energy difference. This is accomplished by means of a perturbative or cluster-type expansion of the EA or IP itself.

On the other hand, the correlation energy is *always* growing with system size, and therefore one *always* faces the problem that intensive energy differences such as bond dissociation energies or barrier heights are shrinking in comparison to the total correlation energy, as molecular size increases. The problem is intrinsic to large-molecule quantum chemistry and is the reason why only size-extensive methods such as coupled-cluster (CC) theory and many-body perturbation theory are appropriate for large systems. Methods that lack size-extensivity, such as truncated configuration interaction approaches, will recover a diminishing fraction of the correlation energy as the number of electrons increases. In the context of EA or IP calculations, the key is to use size-extensive quantum chemistry methods that are carefully calibrated to provide a balanced description of both the neutral and the ionized molecule.

On the topic of electron correlation and balanced approximations, another challenge in the application of quantum chemistry to weakly-bound anions is that the "zeroth order" estimate of the electron affinity, namely, the so-called *Koopmans' theorem* (KT) estimate[35] ($EA \approx -\varepsilon_{LUMO}$) is typically a worse approximation than is the analogous KT estimate for the IP ($IP \approx -\varepsilon_{HOMO}$). This has to do with an error cancellation in the latter estimate that is not present in the former, where errors arising from neglect of electron correlation and neglect of orbital relaxation have the same sign, whereas for IPs these errors have opposite signs. This underscores the need for high-level, correlated descriptions of molecular anions, which adds to the cost. Special problems in the density-functional description of anions, arising

from self-interaction associated with the half-filled orbital of an extra-valence anion, complicate matters further, although the present situation is much better than it has been in the past, due to recent progress in functional development.

Finally, the calculation of temporary anion resonances poses a challenge for quantum chemistry because the metastable anion M^- lies higher in energy (at a fixed molecular geometry) as compared to $M + e^-$, where the electron is an outgoing plane wave. Attempts to compute the energy of M^- using standard, bound-state quantum chemistry methods are therefore susceptible to *variational collapse*, wherein the wave function for what is ostensibly M^- collapses to the wave function for $M + e^-$ as the basis set approaches completeness.[20] Finite-basis calculations thus afford a deceptively seductive but ultimately unrealistic description of M^-,[2] and modifications to standard quantum chemical methods are required to compute accurate energetics for the metastable anion.[20]

TERMINOLOGY AND FUNDAMENTAL CONCEPTS

This section defines and explains some basic chemical and quantum-mechanical concepts concerning anions. Bound anions (where M^- is lower in energy than M, at the minimum-energy geometry of the former) are considered first, and subsequently we discuss metastable anions, also known as temporary anion resonances. For easy reference, a list of acronyms is provided at the end of this chapter.

Bound Anions

Attachment and Detachment Energies

We begin with a careful exposition of the various energy differences associated with attaching or removing an electron. For negative ions in general, one of the key experimental observables that is directly accessible from *ab initio* calculations is the *vertical detachment energy* (VDE), sometimes called the *vertical electron binding energy*. This quantity is defined pictorially in Figure 1 as the energy gap between the ground-state energy of the anion (call it M^-) at its equilibrium geometry and the value of the neutral molecule's potential energy surface at the anion geometry. Note that the ground-state energy of the anion should properly include the anion's zero-point vibrational energy, as indicated in Figure 1. That said, a vertical transition from the anion's minimum-energy geometry need not land on a vibrational state of the neutral molecule, potentially leading to the appearance of a vibrational progression in the anion's photoelectron spectrum. In the example of Figure 1, the $v = 0$, $v = 1$, and $v = 2$ states of AB are likely to be accessed via photodetachment from the $v = 0$ state of AB^-.

Insofar as one is able to map out potential energy surfaces for both M and M^-, one could compute such a vibrational progression by evaluating the appropriate Franck–Condon factors, $\langle \psi_{\text{anion}}(v = 0) | \psi_{\text{neutral}}(v) \rangle$. On the other hand, taking a classical-mechanical view of the nuclear motion, it is often convenient to define the VDE as a continuously varying function of molecular geometry:

$$\text{VDE}(\mathbf{R}) = E_{\text{neutral}}(\mathbf{R}) - E_{\text{anion}}(\mathbf{R}) \quad [2]$$

Here, both energies are evaluated at the same geometry, **R**. For $\mathbf{R} = \mathbf{R}_{\text{anion}}$, this definition coincides with the "experimental" definition of the VDE that is suggested in Figure 1, provided that zero-point corrections are included in $E_{\text{anion}}(\mathbf{R}_{\text{anion}})$, by computing vibrational frequencies for the anion. However, we allow for arbitrary **R** in the definition used here, since Eq. [2] can be used to sample the VDE along a molecular dynamics trajectory. In such a calculation, a histogram of the fluctuations in VDE(**R**) provides a semiclassical explanation for the width of the photoelectron spectrum.[105] The semiclassical picture suggests that Eq. [2] can be used to find and delineate regions of the anion's potential energy surface where the electron would be expected to autodetach, that is, regions where $\text{VDE}(\mathbf{R}) \leq 0$.

Note that Eq. [2] defines the VDE, which excludes relaxation of the neutral species following electron detachment. Including that relaxation energy defines the *adiabatic* electron detachment energy, which is more often called the *adiabatic electron affinity* (AEA),

$$\text{AEA} = E_{\text{neutral}}(\mathbf{R}_{\text{neutral}}) - E_{\text{anion}}(\mathbf{R}_{\text{anion}}) \quad [3]$$

The AEA is also depicted pictorially in Figure 1, as is the vertical *attachment* energy (VAE), which is defined analogously to the VDE but starting from the ground state of the neutral molecule:

$$\text{VAE} = E_{\text{anion}}(\mathbf{R}_{\text{neutral}}) - E_{\text{neutral}}(\mathbf{R}_{\text{neutral}}) \quad [4]$$

One note of caution about terminology: the phrase "electron affinity" by itself (as opposed to AEA) is used somewhat ambiguously in the literature, in the sense that the EA in question might be the AEA, or it could be the EA for a vertical process. We caution against this ambiguous usage. In contrast, the vertical EA and the VDE are two different names for precisely the same energetic quantity, and the use of one term over the other is simply a matter of taste.

In principle, the AEA can be determined experimentally from the onset of the photoelectron spectrum.[43] In practice, however, large differences between the anion and neutral geometries, arising from electron penetration into antibonding orbitals of the neutral molecular framework, leading to reduced formal bond orders in the anion, can give rise to unfavorable Franck–Condon factors that make the AEA difficult to determine.[2] Indeed, the schematic potential energy surfaces in Figure 1 suggest that the $M^-(v = 0) \rightarrow M(v = 0)$

transition will be difficult to locate, experimentally. (The paucity of bound excited states for anions also limits the available experimental techniques to determine EAs.[2]) In such cases, theoretical calculations may be the only means to determine the AEA. In cases where the photoelectron spectrum cannot be vibrationally resolved and fit to a Franck–Condon progression, the VDE is usually taken to be the location of the maximum spectral intensity.

Classification of Molecular Anions

The diffuse nature of an anion's electron density can be understood by examining the asymptotic behavior of the potential energy function for removing an electron from either a neutral molecule, M, or else an anion, M^-. Such potential functions are illustrated schematically in Figure 4(a), and we consider the neutral case first. Ionization of the neutral molecule leaves behind a cationic core and thus asymptotically the potential energy function for this process looks like an attractive Coulomb potential between the outgoing electron and the cation, $V(r) \sim -1/r$. (At short range, the potential ultimately becomes repulsive due to the other valence electrons.) This deep potential well can support a large number of bound states, whose energies can be fit to the formula

$$E_n = -\frac{Z_{\text{eff}} R_H}{(n-\delta)^2} \qquad [5]$$

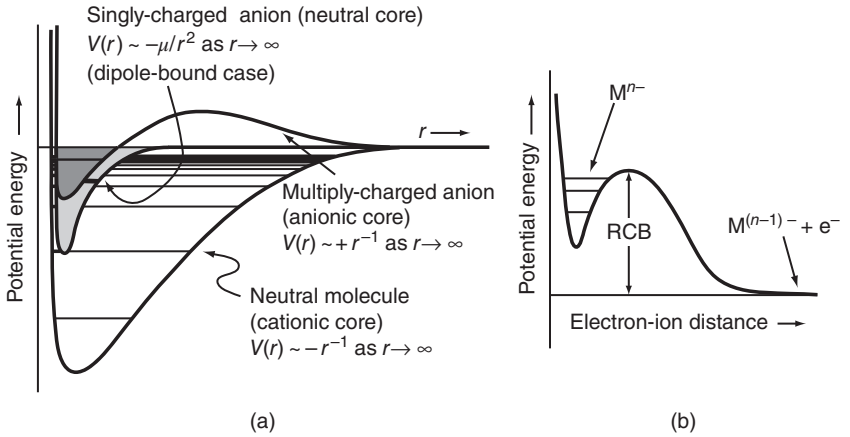

Figure 4 (a) Schematic depictions of the one-electron potential energy function for removing a valence electron from a neutral molecule, a singly-charged anion, or a (stable) doubly-charged anion. The bound-state energy levels represent Rydberg states, and although the figure is qualitative it correctly suggests that anions typically have very few bound Rydberg states. (b) Alternative potential for electron ejection from a multiply-charged anion M^{n-}, in the case where this species is metastable, being trapped behind a repulsive Coulomb barrier (RCB). Panel (a) is based on a similar figure in Ref. 2; copyright 2008 American Chemical Society. Panel (b) is based on a figure in Ref. 106; copyright 2000 American Chemical Society.

where Z_{eff} is some effective charge, $R_H = 13.6$ eV is the Rydberg constant, and δ is known as the *quantum defect*.[107] In analogy to the Rydberg series for the hydrogen atom, these states are known as *Rydberg states*, and it is clear from the figure that they constitute a series of increasingly diffuse excitations (as n increases) of one electron about a cationic core.

Removing an electron from M^- leaves a charge-neutral core. The monopole therefore vanishes in a multipole expansion of the electron–molecule ($M + e^-$) Coulomb interaction, hence there is no strongly attractive $-1/r$ potential at long range, as there is in the $M^+ + e^-$ case. The long-range form of the potential for $M + e^-$ reflects higher order charge–multipole interactions, the longest range of which is the charge–dipole interaction, $V(r) \sim -\mu/r^2$, if M possesses a nonzero dipole moment, μ. [If M has no dipole moment but a nonzero quadrupole moment, Q, then the asymptotic form of the potential is a charge–quadrupole interaction, $V(r) \sim -Q/r^3$.] The $M + e^-$ potential well in Figure 4(a) is much shallower than that for $M^+ + e^-$, consistent with the observation that IPs for neutral atoms and molecules are large compared to EAs. As such, the anion typically possesses few (if any) bound Rydberg states.[2]

In view of this discussion, it is tempting to conceptualize the weakly-bound anions of polar molecules as *dipole-bound* anions.[11] Solution of the Schrödinger equation for an electron interacting with a point dipole reveals that bound states are obtained for dipole moments $\mu > 1.625$ debye,[108,109] with no further molecular structure required. (In practice this threshold should be modified to something like $\mu \gtrsim 2.4$ debye,[11] owing to the possibility of rotational-to-electronic energy transfer,[110–112] but the point remains that a sufficiently large dipole moment alone is enough to bind an electron.) As discussed in detail in Ref. 2, however, it is difficult to fully disentangle the long-range charge–dipole interactions from shorter-range valence-type interactions involving the Coulomb and exchange potentials established by the occupied MOs, which can also stabilize electron binding. A detailed mathematical analysis of these valence interactions has been given by Simons.[42,3]

As a result of these competing interactions, the distinction between a valence anion and a dipole-bound anion is sometimes ambiguous. For example, the acetonitrile (CH_3CN) molecule has a calculated dipole moment of 3.94 debye,[113] well above the threshold value, and an experimental VDE of 0.012 eV.[114] These values might suggest that electron binding will be extremely weak unless the dipole moment is extremely large, since CH_3CN already has a sizable dipole moment as small molecules go, yet barely binds an extra electron. At the same time, the $(BeO)_2^-$ anion has been classified as quadrupole-bound,[115] since the dipole moment of the D_{2h} $(BeO)_2$ framework vanishes by symmetry. One might therefore expect a smaller VDE for $(BeO_2)^-$ as compared to dipole-bound cases, yet the computed VDE for $(BeO)_2^-$ is 1.1 eV![115] Clearly, short-range valence attractions must contribute significantly to the stabilization of $(BeO)_2^-$.

Even in cases where it seems safe to classify M^- as a dipole-bound anion, the balance of long-range charge–dipole interactions and short-range valence interactions means that there is no clear correlation between the magnitude of the neutral molecule's dipole moment (call it μ_0) and the VDE of its anion. For example, whereas $\mu_0 = 3.94$ debye for CH_3CN^- (computed at the MP2 level),[113] and the experimental VDE of this anion is a mere 0.012 eV,[114] the water dimer anion exhibits a smaller value of μ_0 ($\lesssim 2.0$ debye at the MP2 level[116]), yet a *larger* experimental VDE (≈ 0.045 eV).[117,118]

The water dimer anion also provides a simple example of a system where vibrational motion can promote autodetachment. Figure 5 shows one-dimensional potential energy scans of $(H_2O)_2^-$ and $(H_2O)_2$ along the so-called "flap angle" that connects *cis* and *trans* isomers of the dimer. The *cis* isomer of the anion is stabilized by an enhanced dipole moment, but this isomer is destabilized in the neutral dimer owing to slightly larger steric repulsion. The ground vibrational state of $(H_2O)_2^-$ is bound by ≈ 0.045 eV, but the $v_{\text{flap}} = 1$ state is much closer to the neutral $v_{\text{flap}} = 0$ energy and might autodetach if nonadiabatic effects were considered. (The semiclassical picture is that motion along the flap angle coordinate may access the *trans* geometry, where autodetachment is more likely.)

Consider also the case of $(\text{uracil})^-$. This anion exhibits both a diffuse, dipole-bound state and a valence anion state, the latter characterized by a

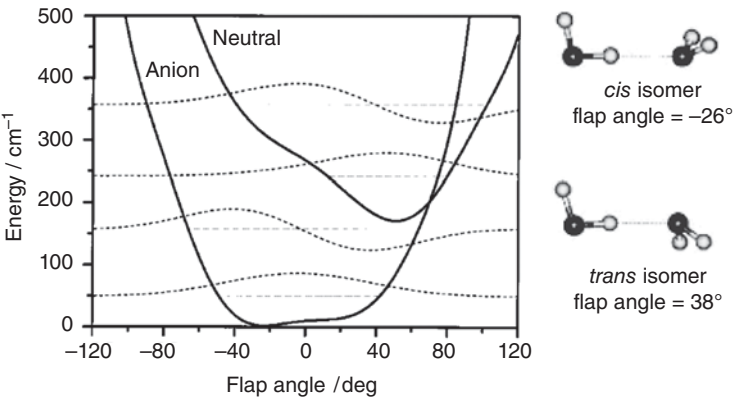

Figure 5 Solid curves: potential energy scans for $(H_2O)_2^-$ and $(H_2O)_2$ along the "flap angle" coordinate, with the other coordinates relaxed. (The *cis* and *trans* structures of the anion, shown at right, suggest the nature of the flap angle.) Calculations were performed at the CCSD(T) level with a large, diffuse basis set,[119] and harmonic zero-point corrections for all coordinates except the flap angle are included in these potentials. In the absence of zero-point corrections, both the *cis* and *trans* isomers of $(H_2O)_2^-$ are local minima, but the latter minimum (at 38°) disappears on zero-point correction. Broken curves: lowest two vibrational wave functions ($v_{\text{flap}} = 0$ and 1) for these one-dimensional potentials. Adapted with permission from Ref. 119; copyright 1999 American Institute of Physics.

half-filled π^* orbital that is bound fairly closely to the molecular framework. Calculations suggest that the two anion states are nearly isoenergetic, although the dipole-bound anion has a much smaller VDE.[120,121] This can be understood in terms of the schematic potential energy surfaces that are depicted in Figure 6(a). The dipole-bound state of $(\text{uracil})^-$ is classified as such because it has essentially the same geometry as neutral uracil, and the dipole-bound anion is characterized by a highly diffuse electron situated at the positive end of the neutral molecule's dipole moment, largely outside of the region of space occupied by neutral uracil's valence electrons. The photoelectron spectrum of $(\text{uracil})^-$ [Figure 6(b)] is typical of what is observed for a dipole-bound anion, namely, a single narrow peak, corresponding to the origin transition, with *much* weaker features at higher energies.[122] The lack of a significant Franck–Condon progression in this case is a consequence of the essentially identical geometries of uracil and dipole-bound $(\text{uracil})^-$. As such, the vibrational wave functions are nearly the same for both species, so when the anion is prepared in its ground

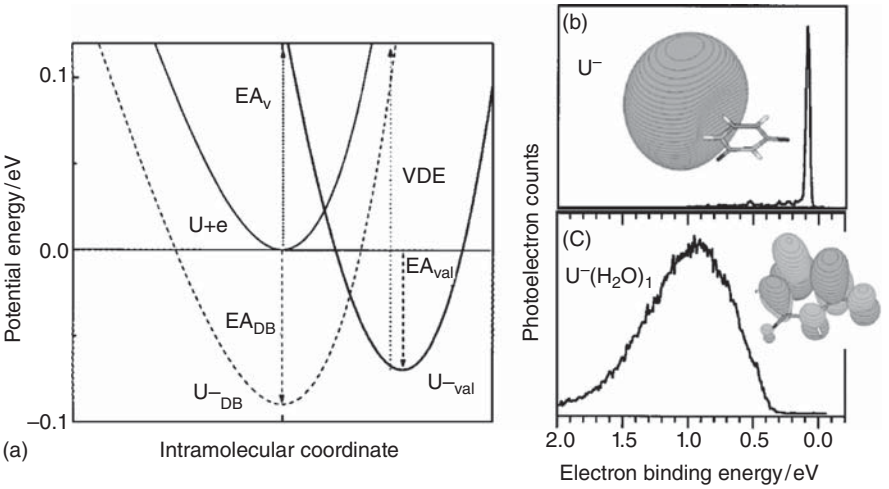

Figure 6 (a) Schematic illustration of the neutral uracil (U) potential surface, labeled U+e, the dipole-bound anion (U^-_{DB}) potential surface, and the valence anion (U^-_{val}) potential surface. The intramolecular coordinate involves out-of-plane displacement of the uracil ring atoms, leading to a nonplanar geometry for U^-_{val}. (b) Photoelectron spectrum of the dipole-bound state of U^-, along with an isosurface plot of the singly occupied molecular orbital (SOMO) for U^-_{DB}. The nearly identical geometries for U and U^-_{DB} lead to a very narrow spectrum. (c) Photoelectron spectrum for $[U(H_2O)]^-$ and isosurface plot of the SOMO for U^-_{val}. The spectrum illustrates both the larger binding energy of the valence anion, as compared to the dipole-bound state, as well as the much greater spectral width resulting from distortion of U^- away from a planar geometry. Panel (a) is reprinted with permission from Ref. 120; copyright 1998 American Chemical Society. Spectra in (b) and (c) are reprinted with permission from Ref. 122; copyright 1998 American Institute of Physics. Orbital isosurfaces plots are reprinted with permission from Ref. 123; copyright 2004 the PCCP Owner Societies.

vibrational state, only the origin transition is observed with any appreciable intensity.

In contrast, the valence anion character of the $(\pi^*)^-$ state can be deduced, computationally, from the nonplanar nature of the anion's geometry, which results from the lifting of aromaticity due to an odd number of π electrons. As a result of geometric distortion, the VDE of the valence anion is significantly larger than that of the dipole-bound state, as indicated in Figure 6(a), even though these two anions are very close in energy. Electron attachment to form the dipole-bound state, which can occur at or near the minimum-energy geometry of neutral uracil, has been suggested as the initial step in a DEA mechanism that involves subsequent internal conversion to the valence anion state, followed by bond cleavage.[124,125]

While theory predicts U^-_{DB} and U^-_{val} to be nearly isoenergetic, only the dipole-bound state is observed in the experiments reported in Ref. 122 [Figure 6(b)]. The thermodynamics of which isomers are stable provides no information about how these species are actually formed in a molecular beam experiment, and nonthermal ensembles are probably common in anion photoelectron spectroscopy.[126–129] In the experiments of Ref. 122, the valence anion state *was* observed (to the exclusion of the dipole-bound anion signal) in a complex with a single water molecule, $[(\text{uracil})(H_2O)]^-$. The photoelectron spectrum of this complex [Figure 6(c)] is much broader, owing to the differences in the geometries of the anion and the neutral molecule that lead to nontrivial Franck–Condon factors, even if individual vibrational states of uracil cannot be resolved. Later, under different source conditions, the valence anion state *was* observed for bare uracil,[130] which highlights the fact that anion spectroscopy can be particularly sensitive to the source conditions of the molecular beam.

Finally, let us consider the case of multiply-charged anions, M^{n-}. One possible potential energy curve for a multiply-charged anion is sketched in Figure 4(a) for the case where M^{n-} is stable (lower in energy than $M^{(n-1)-} + e^-$). This potential is repulsive at medium-range distances since it correlates asymptotically to separating two negatively charged species. At short range, however, there may be stabilizing valence interactions leading to a local potential minimum. On the other hand, these stabilizing interactions may be insufficient to lower the potential well below the asymptotic $M^{(n-1)-} + e^-$ energy; Figure 4(b) depicts a case where they are not. In this case, the multiply-charged anion is metastable only. Insofar as M^{n-} can be formed, it exists only because it is trapped behind a repulsive Coulomb barrier (RCB). This species will persist only until such time as an electron is able to tunnel through the RCB.

Although multiply-charged anions are ubiquitous in polar solvents, where the internal Coulomb repulsion of M^{n-} is offset by highly favorable electrostatic and induction interactions with the solvent molecules, multiply-charged anions have historically been difficult to prepare in gas-phase experiments that could directly probe the $M^{(n-1)-} + e^-$ interaction potential. Recently, however,

it has been demonstrated that such anions can be prepared using electrospray ionization,[131,132] and photoelectron spectra at different excitation energies place experimental bounds on the magnitude of the RCB. For the citrate trianion, $C_3H_5O(COO)_3^{3-}$, whose three negatively charged carboxylate moieties are separated by ≈ 6 Å, the result is 1.9 eV < RCB < 2.5 eV.[133] Unbranched dicarboxylate dianions, $^{-}O_2C(CH_2)_nCO_2^{-}$, allow for systematic variation of the RCB, and these species are found to be stable on the timescale of a time-of-flight photoelectron spectroscopy experiment (∼0.1 s) for $n \geq 3$.[134,135] This is consistent with back-of-the-envelope calculations suggesting that two negative charges separated by $\lesssim 4$ Å will be unstable;[2] in the $n = 3$ dicarboxylate, the two terminal carbon atoms are separated by ≈ 5 Å (assuming typical bond lengths), whereas in the $n = 2$ case the separation is < 4 Å. Interestingly, the $n = 2$ (succinate) dianion is rendered stable on complexation with just a single water molecule, and the photoelectron spectrum of this complex has been reported.[134,135] Calculations suggest that a complex containing 2–3 water molecules is necessary to stabilize HPO_4^{2-} but ∼16 water molecules are required to stabilize PO_4^{3-}.[136]

Cluster Anions and Solvated Electrons

The examples of the succinate–H_2O complex and the uracil–H_2O valence anion state that were discussed earlier demonstrate that solvent molecules can play a critical role in anion binding, even in a gas-phase experiment, and thus cluster anion photoelectron spectroscopy[94,19] warrants some discussion in its own right. More dramatic examples of the role of solvent in electron binding belong to a broad class of systems known as *solvated electrons*. From a gas-phase point of view, one might define a solvated electron as any cluster anion M_N^- (or mixed cluster anion; the molecules need not all be the same) for which the molecular anion M^- is not a bound species, or at least is much more weakly-bound than is the cluster anion M_N^-. As such, electron binding is a collective phenomenon, and this collective binding can be quite strong for sizable clusters. For example, whereas $(H_2O)_2^-$ has a VDE of only 0.045 eV,[117,118] for $(H_2O)_N^-$ with $N \sim 80$–100, one can find isomers with VDEs > 2.0 eV.[4,5] Due to the collective nature of electron binding in clusters, the VDE is the primary observable of merit; AEAs are essentially impossible to determine for cluster anions, due to solvent reorganization on electron detachment. Indeed, it is not even clear whether the concept of an AEA is meaningful in such cases, since removing the solute (an electron) creates a qualitatively different system (a neat solvent cluster rather than a solvated-electron cluster).

Much of the interest in these clusters is driven by the importance of the aqueous electron in bulk water, e^-(aq). This species, along with $H^\bullet$ and $HO^\bullet$, is one of the primary radical intermediates that is formed on water radiolysis[84,17,50,18,13] and can be detected following radiolysis of ammonia, alcohols, and organic amines as well.[50] Figure 7 provides an overview of the sequence of events involved in water radiolysis, which is initiated either

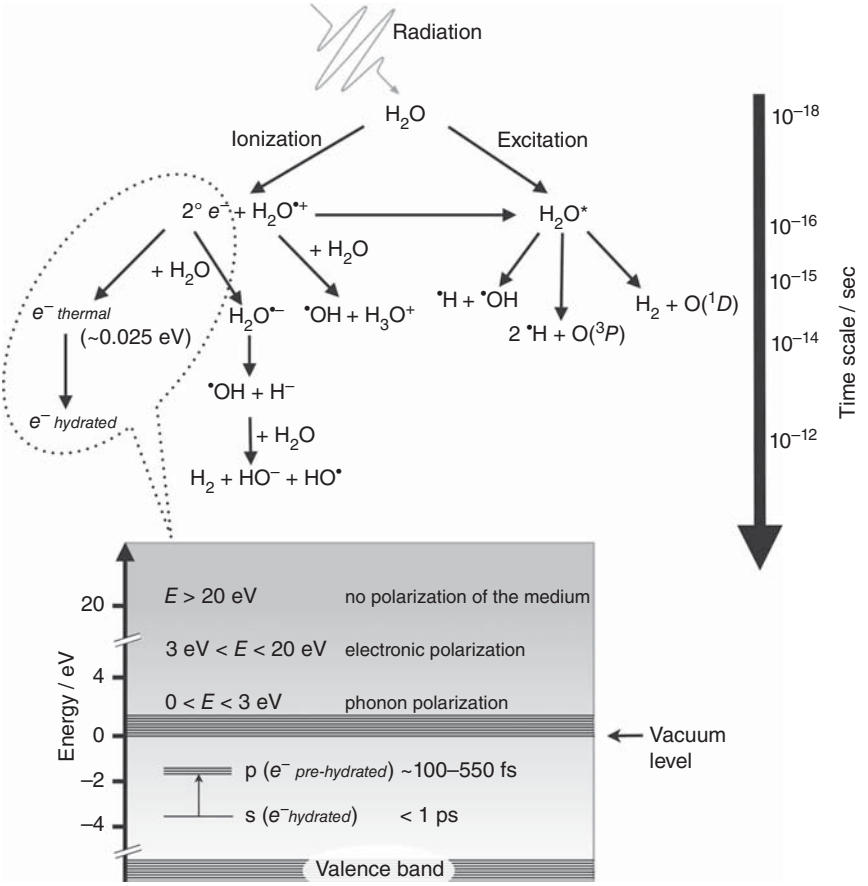

Figure 7 Upper scheme: schematic overview of water radiolysis, wherein ionizing radiation generates three primary radical intermediates, e^-(aq), H$^\bullet$, and HO$^\bullet$. Lower panel: schematic energy diagram for an electron interacting with liquid water but modified to eliminate the conduction band of water in the lower panel, because other studies[137,138] indicate that the conduction band lies no more than ~0.1 eV below the vacuum level, whereas the original figure in Ref. 13 places the conduction band much lower in energy. (Adapted with permission from Ref. 13; copyright 2012 American Chemical Society.)

by electronically-excited water molecules or else water cation radicals that are generated either by absorption of ionizing radiation or else via collisions with high-energy "primary" electrons.[13] Following the track on the left in Figure 7, the initial ionization event leads to the formation of lower energy "secondary" (2°) electrons, which subsequently thermalize by dissipating energy into vibrational modes of the solvent and ultimately become solvated in a deep potential well. The depth of this well (relative to the vacuum level, corresponding to a free electron) can be estimated by extrapolation of VDEs for the highest-binding isomers of gas-phase $(H_2O)_N^-$ clusters. This

extrapolation yields estimates of 3.4 eV[139] and ~4 eV,[5] depending on the experimental data set used. Direct experimental measurements of the VDE for e^-(aq), using liquid microjet photoelectron spectroscopy,[140] afford values ranging from 3.3 to 3.7 eV.[7−10] A detailed theoretical calculation, including the effects of electronic relaxation on vertical detachment and extrapolating to an infinitely large simulation cell, affords a value of 3.7 eV.[141]

The lower panel of Figure 7 provides a rough energy-level structure for an "excess" electron in water that is consistent with the estimated VDEs quoted earlier. This diagram is labeled according to the conventional interpretation of the structure of e^-(aq),[15,16,142,143] namely, that the ground state of the fully hydrated species can be conceptualized as a particle in a quasi-spherical solvent void, whose ground-state wave function exhibits pseudo-s symmetry. Within this picture, the states responsible for the strong electronic absorption at ~1.7 eV (720 nm), which is the most characteristic feature of e^-(aq),[15] are quasi-degenerate p-type states, as suggested in the lower panel of Figure 7. Although this picture is quite entrenched and appears to be consistent with plane-wave DFT simulations performed in the liquid phase,[144−146] the cavity model has been questioned both historically[147−149] as well as recently.[150−156] Alternative structural models are a solvent–anion complex,[149] a $HO^- \cdots H_3O$ complex,[147,148] a hydronium radical ($H_3O^\bullet$) that exhibits charge-separated biradical character on hydration,[150−153] and a delocalized wave function with a buildup of water density inside said wave function.[154,156] These alternative proposals have proved controversial,[157−162] and more work is needed to definitively resolve this question, because at present both the cavity and noncavity models explain *certain* features of the spectroscopy of the species called e^-(aq), but each is inconsistent with other features.[15,162,156,163]

Cluster analogues of solvated electrons, M_N^-, have been studied extensively for a variety of polar and nonpolar solvents, as discussed in numerous recent reviews.[15,16,19,94,164] A key aspect of cluster ion spectroscopy is the attempt to determine how the solvent network accommodates the ionic solute, which in this case is an extra electron. Figure 8 shows VDE data, obtained from photoelectron spectroscopy, for some representative solvated-electron clusters. (Experimentally, the VDE is taken to be the energy at which the rather broad photoelectron spectrum is peaked.) Figure 8 employs the common practice of plotting cluster anion VDEs versus $N^{-1/3}$, where N denotes the cluster size. The reason for this convention is that the cluster radius, R, should be proportional to $N^{+1/3}$ for a spherical cluster, and by taking $R \propto N^{+1/3}$ in conjunction with a dielectric continuum treatment of the spherical solvent cluster, one obtains a VDE proportional to R^{-1} or $N^{-1/3}$.[167−170]

Let us consider this in a slightly more detail. Although the result $\mathrm{VDE}(N) \propto N^{-1/3}$ can be derived from continuum dielectric theory under a variety of assumptions,[167−170] a simple model is the following. Consider a single point charge $-e$ centered in a cavity of fixed radius, a, representing the excluded volume of the solvent void inhabited by the solvated electron.

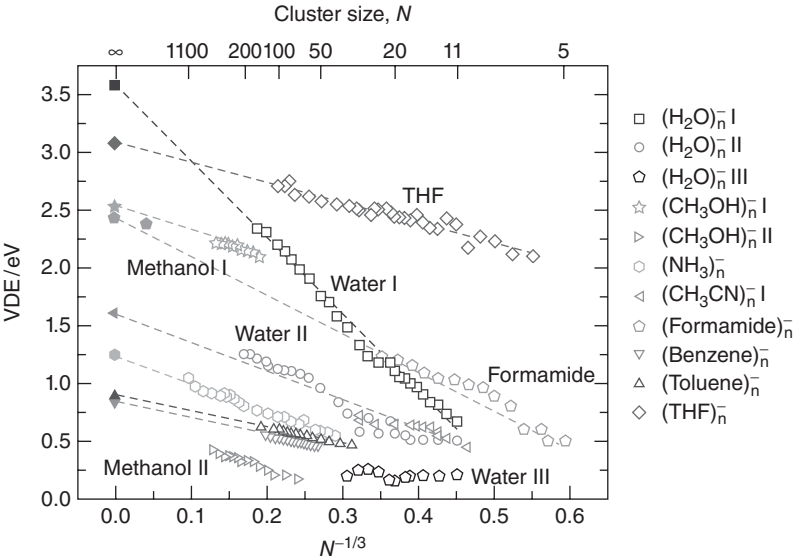

Figure 8 VDEs for various cluster anions M_N^- as a function of $N^{-1/3}$. For water, three distinct isomeric series are observed, which are labeled I, II, and III,[4] and for methanol, two isomers (I and II) are observed.[165] For acetonitrile, two isomers are observed[166] but only one is plotted here. Reprinted with permission from Ref. 19; copyright 2012 American Chemical Society.

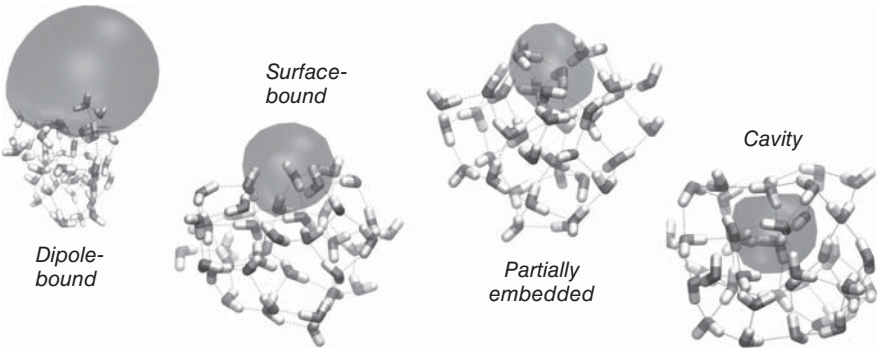

Figure 9 Illustration of the four distinct electron binding motifs identified in $(H_2O)_N^-$ clusters on the basis of one-electron QM MM simulations, for the case $N = 40$. The isosurfaces that are depicted encapsulate 70% of $|\psi|^2$. Reprinted from Ref. 95; copyright 2011 American Chemical Society.

[See, for example, the cavity isomer of $(H_2O)_{40}^-$, at the far right in Figure 9.] This cavity is assumed to be carved out of a spherical, homogeneous dielectric material whose radius is R and is characterized by a dielectric constant, ε_s. The solvation (free) energy for the $-e$ charge is the VDE for this model. The

mathematical result, for $R \gg a$ and given in atomic units, is[170]

$$\mathrm{VDE}(R) = \mathrm{VDE}(\infty) - \frac{1}{2R}\left(1 + \frac{1}{\varepsilon_\infty} - \frac{2}{\varepsilon_s}\right) \quad [6]$$

This leads immediately to the desired result:

$$\mathrm{VDE}(N) = \mathrm{VDE}(\infty) + AN^{-1/3} \quad [7]$$

Experimentally, the parameter A corresponds to the slope of one of the best-fit extrapolations in Figure 8. It should be noted that the $N^{-1/3}$ proportionality in Eq. [7] can be derived *without* the assumption that the electron inhabits a cavity, provided only that the electron's wave function is spatially localized.[167–169]

The two dielectric constants in Eq. [6] warrant some discussion. The quantity ε_s, which is sometimes called simply "the dielectric constant" (often denoted ε instead of ε_s) is more precisely the *static* or zero-frequency dielectric constant. (Even more precisely, it is the scalar electric permittivity relative to that of vacuum,[171] and is therefore dimensionless.) This quantity includes the effects of both orientational and electronic polarization. For a vertical ionization process, however, the solvent's orientational degrees of freedom are frozen, but the electron densities of individual solvent molecules can adjust on the same timescale on which the ionization process occurs. Such considerations lead to a correction involving the optical (infinite-frequency) dielectric constant, $\varepsilon_\infty = n_{\mathrm{refr}}^2$, where n_{refr} denotes the solvent's index of refraction.[172]

Values of ε_s vary widely from one solvent to the next, due to a particular solvent's ability (or lack thereof) to reorient permanent dipole moments of individual solvent molecules. Considering some examples at 25 °C, we have $\varepsilon_s = 78$ (water), 21 (acetone), 4.8 (chloroform), and 2.3 (benzene). Optical dielectric constants, on the other hand, are much more similar between different solvents: $\varepsilon_\infty = 1.78$ (water), 1.85 (acetone), 2.09 (chloroform), and 2.25 (benzene). From Eq. [6], one might anticipate that electronic polarization effects are most significant in polar solvents, for which $\varepsilon_s \gg \varepsilon_\infty$, and this is indeed the case. For electron solvation in bulk water, for example, continuum models more sophisticated than Eq. [6], as well as atomistic simulations using a polarizable solvent model, afford an estimate of ≈ 1.4 eV for the *electronic reorganization energy* that accompanies vertical detachment.[141] In other words, the predicted VDE is reduced by ≈ 1.4 eV (and brought into quantitative agreement with experiment[141]) when the solvent's electronic degrees of freedom are allowed to adjust to electron detachment, at fixed nuclear positions.

Returning to the VDE data in Figure 8, one can see that methanol cluster anions exhibit two distinct isomeric series. This implies that there are two peaks in the photoelectron spectra, whose peak positions exhibit different slopes, A, with respect to $N^{-1/3}$. (The relative intensities of the two peaks can be changed by modifying the backing pressure of the carrier gas, which effectively changes

the temperature of the molecular beam, thus demonstrating that the two features are indeed distinct isomers.[4,19]) On the basis of theoretical calculations, these two isomeric series have been attributed to a surface-bound electron and a cavity-bound electron.[16] Note, however, that *both* the "methanol I" and "methanol II" data series in Figure 8 appear to be linear as a function of $N^{-1/3}$. In fact, one can construct a continuum electrostatics model such that, in large clusters, the VDE for a *surface-bound* electron is also proportional to $N^{-1/3}$.[170] Thus, one cannot directly infer structure from the linearity of the data in Figure 8.

Caution is warranted especially in the case of water cluster anions, as there has been much debate regarding the nature of the electron binding motifs in these systems.[4,5,93,95,173–177] Water cluster anions exhibit at least three[4] – and possibly four[5] – distinct isomeric series, depending on experimental conditions, and it is not altogether clear that the "water I" data in Figure 8 actually correspond to a single isomeric species.[5,95] In a recent study that relies on one-electron quantum mechanics/molecular mechanics (QM/MM) calculations using an electron–water pseudopotential model,[141,95] our group has suggested four distinct binding motifs,[95] examples of which are illustrated in Figure 9 for the case of $(H_2O)_{40}^-$. From left to right in the figure, the four categories of isomers that we have identified are the following:

- A weakly dipole-bound cluster anion that predominates when an extra electron is attached to a cold, equilibrated, neutral water cluster.
- A surface-bound electron with a somewhat larger VDE (and correspondingly less diffuse wave function) that can be reached from the dipole-bound state following modest rearrangement of some surface water molecules, so that several dangling O—H moieties coordinate to the e^- wave function.
- A considerably more strongly-bound "partially embedded" surface isomer. In this case, rearrangement of water molecules at the cluster surface has resulted in a partial solvation shell.
- A fully internalized, cavity-bound isomer.

VDEs computed on the basis of quantum classical molecular dynamics simulations at finite temperature correctly reproduce the *N*-dependent trends observed experimentally and are in semiquantitative agreement with the absolute VDEs determined from photoelectron spectroscopy[4,5] for cluster anions in the size range $20 \leq N \leq 200$.[95] These simulations suggest that the "water I" data in Figure 8 may actually represent a transition between a surface-bound and a partially embedded isomer, whereas somewhat higher-binding cavity isomers are observed (according to the calculations) only in certain experiments,[5] where the clusters are annealed in an ion trap prior to interrogation.[95] On the other hand, the predictions of one-electron models have been shown to be somewhat sensitive to the fine details of how the electron–molecule

pseudopotential is constructed.[15,159–161] As such, it is probably too early to say that the identities of the isomers in $(H_2O)_N^-$ photoelectron spectroscopy have been definitely determined.

One final example of a solvated-electron cluster is that of acetamide cluster anions, $(CH_3CONH_2)_N^-$. For these clusters, photoelectron spectra reveal the presence of two isomers, and on the basis of calculations these are attributed to the two-electron binding motifs depicted in Figure 10.[178] One of these isomers consists of coplanar, ladder-like arrangements of acetamide units, with electron binding occurring at the free (non-hydrogen-bonded) N—H moieties. The other isomer consists of a folded form that one might begin to call a solvated electron. One might anticipate that the highly-ordered ladder-like isomers would be present in small clusters only, with the more globular structures prevailing in larger clusters, but precisely the opposite is observed in the experiments. For $n \geq 9$, the feature that is attributed to the folded isomer is entirely absent.[178]

All of these examples underscore the need for theoretical calculations to aid in the identification of various solvated-electron isomers and binding motifs.

Metastable (Resonance) Anions

The discussion earlier implicitly assumes that the anion M^- is bound, that is, lower in energy than the neutral molecule M at the geometry of M^-. At the heart of dissociative electron detachment, however, are temporary anion resonances that are metastable only with respect to autodetachment. This is the case, for example, when the anion M^- is formed at the neutral molecule's geometry in the example depicted in Figure 1. Here, the anion is higher in energy at the neutral molecule's most stable geometry.

To motivate the discussion of temporary anion resonances, we first discuss the basic quantum mechanics of the resonance phenomenon, using a piecewise constant potential that facilitates analytic results. This is a standard graduate-level quantum mechanics exercise, but the results should be qualitatively informative to readers who have not seen them.

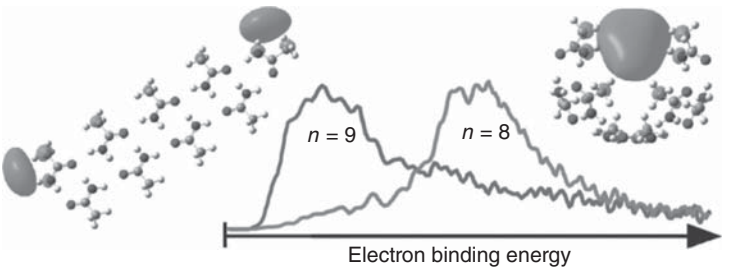

Figure 10 Calculated SOMOs for two different electron binding motifs in $(acetamide)_9^-$, on the left, and $(acetamide)_8^-$, on the right, superimposed with the corresponding photoelectron spectra. Reprinted from Ref. 178; copyright 2012 American Chemical Society.

Basic Quantum Mechanics

Consider the symmetric double square barrier potential that is plotted in Figure 11:

$$V(x) = \begin{cases} 0, & x < -\frac{1}{2}L - w \\ V_0, & -\frac{1}{2}L - w \le x \le -\frac{1}{2}L \\ 0, & -\frac{1}{2}L < x < \frac{1}{2}L \\ V_0, & \frac{1}{2}L \le x \le \frac{1}{2}L + w \\ 0, & x > \frac{1}{2}L + w \end{cases} \quad [8]$$

For a particle incident from the left, the wave function should have the form

$$\psi_{\mathrm{I}}(x) = A_{\mathrm{I}} \exp(ik_{\mathrm{I}}x) + B_{\mathrm{I}} \exp(-ik_{\mathrm{I}}x) \quad [9]$$

in region I, and the outgoing wave function should have the form

$$\psi_{\mathrm{V}}(x) = A_{\mathrm{V}} \exp(ik_{\mathrm{V}}x) \quad [10]$$

in region V.

The one-dimensional *probability current density* is defined as[179]

$$j[\psi] = \frac{i\hbar}{2m}\left(\psi \frac{\partial \psi^*}{\partial x} - \psi^* \frac{\partial \psi}{\partial x}\right) \quad [11]$$

For a wave function of the form $\psi(x) = A \exp(ikx)$, one obtains $j = |A|^2(\hbar k/m)$. As such, the *transmission probability*, T, for transit through the double-barrier in Figure 11 is appropriately defined as the ratio of the

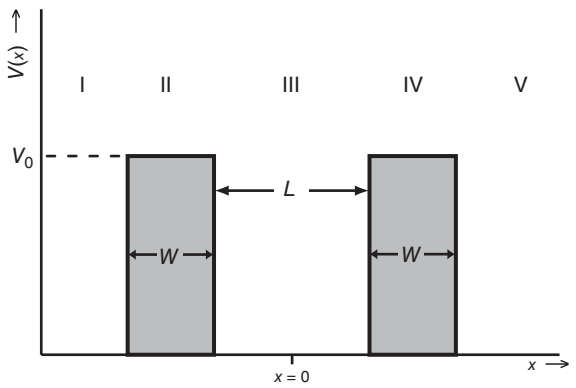

Figure 11 Potential energy function for a symmetric double square barrier. The regions labeled I–V represent the different piecewise constant values of $V(x)$.

probability flux exiting the rightmost extent of the potential ($x = L/2 + w$) to that entering the left-most extent of the potential ($x = -L/2 - w$):

$$T = \frac{j[A_V \exp(ik_V x)]}{j[A_I \exp(ik_I x)]} = \frac{k_V |A_V|^2}{k_I |A_I|^2} \quad [12]$$

This ratio is dependent on the energy of the incident particle, $E = (\hbar k_I)^2/2m$, and can be obtained by matching piecewise functions $\psi(x) = A \exp(\pm ikx)$ and their first derivatives in regions I–V, where each piecewise function is obligated to satisfy the time-independent Schrödinger equation. For the potential in Figure 11, and for solutions with $E < V_0$, the result is[180,181]

$$T(E) = \left[1 + \frac{V_0^2 M^2 \sinh^2(\alpha w)}{4E^2(V_0 - E)^2}\right]^{-1} \quad [13]$$

where

$$\alpha = \frac{1}{\hbar}\sqrt{2m(V_0 - E)} \quad [14]$$

is the inverse tunneling wavelength into the classically forbidden barrier regions and

$$M(E) = 2(\sqrt{E(V_0 - E)})\cosh(\alpha w)\cos(kL) - (2E - V_0)\sinh(\alpha w)\sin(kL) \quad [15]$$

The incident wave vector, $k = (2mE)^{1/2}/\hbar$, is set by the energy of the incident particle, E.

The function $T(E)$ in Eq. [13] is plotted in Figure 12 for several values of w and L but a common value of V_0. When the barrier is wide ($w = 10$ bohr in Figure 12), there is very little transmission except around a sequence of narrow resonances, for which $T(E) \to 1$; these occur as $M(E) \to 0$. When the tunneling length scale α^{-1} is small compared to the barrier width w (which is the case for this particular set of parameters), then $\tanh(\alpha w) \approx 1$, and the condition $M(E) = 0$ becomes

$$\frac{2\sqrt{E(V_0 - E)}}{2E - V_0} = \tan(kL) \quad [16]$$

This is similar to the condition that defines the bound-state energy levels for a particle trapped in a finite square well of width L and depth V_0.[180] Indeed, if we narrow the barriers to $w = 4$ bohr, but leave the distance between them unchanged at $L = 20$ bohr, then the resonances in $T(E)$ broaden, due to additional tunneling through the narrower barriers, yet these resonances remain peaked around the same particle-in-a-square-well energy levels. On the other hand, decreasing L shifts these resonances to higher energies and results in a smaller number of them, consistent with the behavior of the square-well energy levels as a function of L, for a square-well potential with a finite binding energy, V_0.

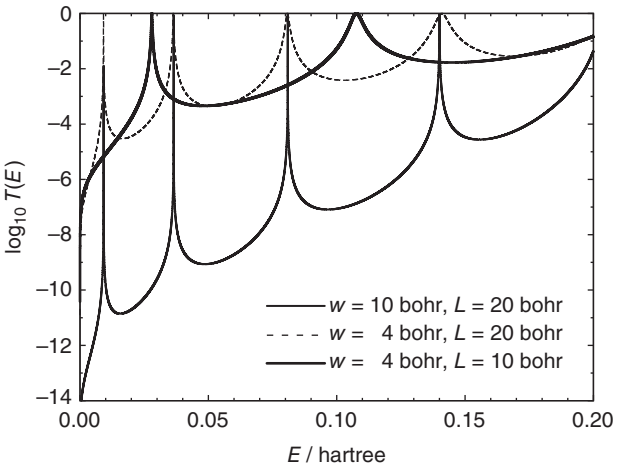

Figure 12 Transmission probability, $T(E)$, through the double-barrier potential in Figure 11, as a function of the incident particle's kinetic energy. The particle has the mass of an electron, and the barrier height is $V_0 = 0.2$ hartree.

This simple, analytically-solvable example captures the essence of the resonance phenomenon: incident particle energies that match, or nearly match, bound-state energy levels of a particular potential can become trapped, even if such states are asymptotically unstable. In a time-dependent picture, an incident particle whose kinetic energy matches a bound-state energy level can be captured for some finite period of time, before ultimately tunneling out of this potential. Importantly, the incoming particle's wave function e^{ikx} must be precisely matched to the wave function inside the potential well (or double-barrier, in this example), as shown in Figure 13.

Classification of Temporary Anion Resonances

Temporary anion resonances can be broadly classified according to two criteria. First, does the electron attach to the ground state of the molecule M, or is M excited in the process? If M remains in its ground state, then the resonance is classified as a *single-particle resonance*, since excitation of M's electrons can be ignored in a qualitative treatment. In contrast, a *core-excited* or *target-excited* resonance involves electronic excitation of M, for example,

$$e^- + M[(\pi)^2(\pi^*)^0] \rightarrow M^-[(\pi)^1(\pi^*)^2] \qquad [17]$$

which provides a mechanism for the attachment of higher-energy electrons, since the $M \rightarrow M^*$ excitation of the molecular "core" serves as a sink for electron kinetic energy. The second criterion is whether the separated species ($M + e^-$) are higher or lower in energy as compared to their complex (M^-). In other words, is the AEA of the molecule, M, positive or negative? If M^- lies higher in energy, the resonance is classified as a *shape resonance* whereas if M^- lies below

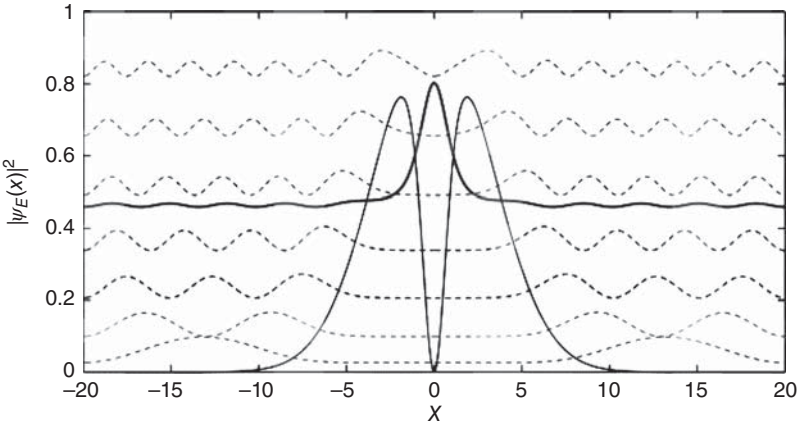

Figure 13 Illustration of a resonance state for a smooth double-barrier potential. At most energies $E = (\hbar k)^2/2m$, the continuum states $\psi_E(x)$ are affected by the presence of the barriers but not in a way that prevents significant transmission of the particle from left to right, or that results in significant accumulation of probability between the barriers. Such states are indicated by the dashed plots of $|\psi_E(x)|^2$. For certain incident energies, however, a resonance is observed (solid wave function). The vertical axis plots the particle's probability density, $|\psi_E(x)|^2$, but the plots are offset vertically according to the value of E. Reprinted from Ref. 182; copyright 2012 Elsevier.

$M + e^-$ it is classified as a *Feshbach resonance*. These definitions are most easily understood using simple one-dimensional potentials, as discussed later.

We first discuss the origin of anion shape resonances, which can be understood as follows. From the Schrödinger equation for the hydrogen atom, one learns that the electron experiences an effective radial potential of the form

$$U_{\text{eff}}(r) = U(r) + \frac{\hbar^2 \ell(\ell+1)}{2\mu r^2} \qquad [18]$$

where $U(r) = -1/r$ is the bare Coulomb potential (in atomic units), and the second term is a *centrifugal potential* arising from the conservation of angular momentum. The same form of the potential can be expected if we try to add an electron to a MO with angular momentum quantum number ℓ, except that in the molecular case the potential $U(r)$ would involve Coulomb and exchange operators for the valence electrons, averaged over MOs.[3] An effective electron–molecule potential with correct asymptotic behavior is sketched in Figure 14(a). A bound state of this potential with energy level ε is actually only metastable, in the sense that it lies above the asymptotic $(M + e^-)$ value of the potential but may be trapped temporarily by the centrifugal potential, if the attachment process involves an orbital with nonzero angular momentum [$\ell > 2$, in the example of Figure 14(a)]. Whether or not this occurs depends sensitively on the details of $U(r)$; for example, one may add an electron to a π^* orbital of O_2 to obtain a *bound* O_2^- anion, yet the lowest $(\pi^*)^-$ state of N_2^- is

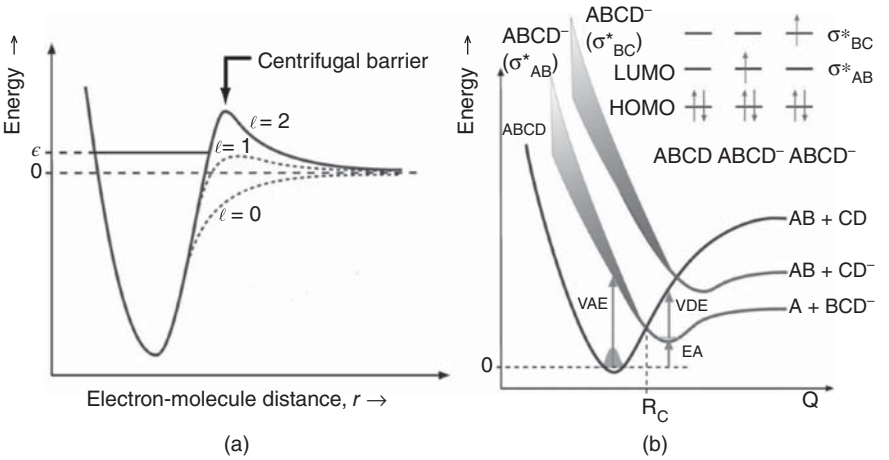

Figure 14 Schematic illustration of the origin of an anion shape resonance. (a) An electron–molecule interaction potential, illustrating the centrifugal barrier for various values of the angular momentum quantum number, ℓ. (b) Single-particle shape resonances arising from electron attachment to either the LUMO or LUMO+1 of molecule ABCD. Both orbitals are assumed to be of σ^* type, and the coordinate Q represents stretching of either the A—B or B—C bond. Shaded regions indicate energy widths arising from lifetime broadening. Adapted from Ref. 83; copyright 2008 Elsevier.

unbound, even though the centrifugal potential corresponds to $\ell = 1$ in either case.[2] As always, much of the beauty as well as the complexity of molecular physics lies in the fact that molecules are not all the same; subtle shifts in the energy-level structure afford qualitatively different properties.

Shape resonances are cases where the species in question (M^-) lies above its own continuum ($M + e^-$), but is trapped behind some barrier. [Note in Figure 14(b) that M^- is higher in energy than $M + e^-$ at the geometry of the neutral molecule, M.] Although we have stated this definition in terms of an anion shape resonance, cases not involving anions exist as well. For example, Ar_2 exhibits "orbiting" shape resonances, as do some simple atom–diatom (A + BC) scattering experiments.[183] In these cases, the rotational energy of the complex lies above the asymptotic dissociation threshold, yet the complex is trapped behind a centrifugal barrier arising from the orbital angular momentum.

For temporary anion resonances, VAEs can be measured experimentally by means of electron transmission spectroscopy,[2,184,185] in which an atomic or molecular sample is bombarded by a beam of electrons having well-defined kinetic energy. A change in current, due to attenuation of the electron beam, can then be detected as the kinetic energy of the electrons is tuned through a resonant VAE.

A simple one-dimensional picture of a single-particle anion shape resonance is depicted in Figure 14(b) for the hypothetical molecule ABCD. In this

example, electron attachment to either the LUMO or the LUMO+1 of ABCD results in a temporary $(\sigma^*)^-$ anion. This species can decay either by autodetachment, which corresponds to the electron–molecule coordinate in Figure 14(a), or else by bond dissociation. Two different bond dissociation coordinates are mapped out in Figure 14(b), depending on which σ^* orbital captures the electron. Although qualitative, these sketches are realistic in the sense that the orbitals available for electron attachment in closed-shell molecules are typically antibonding orbitals with fairly small bond dissociation energies. In certain cases, these σ^* states might be dissociative,[82] meaning that they fail to bind any vibrational levels at all. Single-particle shape resonances tend to be found at low incident electron energies ($\lesssim 5$ eV), else M would likely be electronically excited by electron attachment. In addition, the presence of readily available exit channels, including both autodetachment and bond fission, means that shape resonances are typically very short-lived, with lifetimes on the order of 10^{-12}–10^{-14} s,[12,83,185] and often closer to 10^{-14} s.[185]

As a result of these short lifetimes, electron attachment energies for anion shape resonances are considerably broadened by the time-energy uncertainty principle.[83,183] For a finite lifetime Δt, the resonance energy is subject to broadening according to[179]

$$(\Delta E)(\Delta t) \gtrsim h \qquad [19]$$

For $\Delta t = 1$ ps, this corresponds to a so-called "natural" line width $\Delta E \gtrsim 0.004$ eV, suggesting that a lifetime of ~ 1 ps constitutes an upper bound beyond which we need not worry too much about lifetime broadening. For $\Delta t = 10^{-14}$ s, however, the line width $\Delta E \gtrsim 0.4$ eV is certainly not negligible. As suggested by the diagrams in Figure 14(b), broadening increases as the separation between anion and neutral potential surfaces increases.

Figure 15 illustrates a pair of core-excited resonances, again involving the hypothetical molecule ABCD, which is now electronically excited on electron attachment. One of the temporary anion states suggested in the figure is a core-excited shape resonance and the other is a core-excited Feshbach resonance. The former is very much like the shape resonances discussed earlier, and thus we expect it to be short-lived. Since the resonance involves M*, however, the incident electron energies might be more like ~ 5–15 eV,[12] which can be understood as the ~ 0–5 eV of a single-particle shape resonance plus a typical molecular electronic excitation energy of something like 5–10 eV. As a point of terminology, core-excited resonances involving electronic excitation are sometimes called *auto-ionizing* resonances, since M^- in its excited electronic state is metastable with respect to autodetachment.

In the particular scenario illustrated in Figure 15, one obtains very different energetics depending on the orbital to which the electron attaches. For one particular electron-attached configuration, the anion $ABCD^{*-}$ lies below the neutral excited species, ABCD*, making this a Feshbach resonance. Because ABCD* is energetically inaccessible in this case, the autodetachment channel is closed and thus Feshbach resonances are sometimes called *closed-channel*

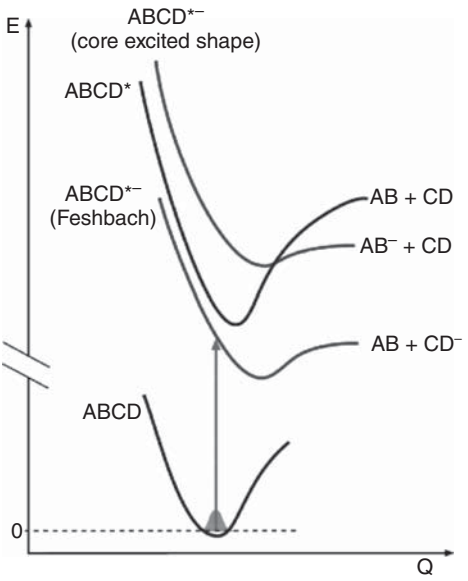

Figure 15 One-dimensional picture of a core-excited shape resonance and a core-excited Feshbach resonance. The two anion states differ in whether the electron attaches to an orbital associated with AB or with CD. Reprinted from Ref. 83; copyright 2008 Elsevier.

resonances. (Similarly, shape resonances are sometimes called *open channel resonances*.) Furthermore, the Feshbach resonance state cannot collapse to the ground state of neutral ABCD except via a two-electron process, whereas other decay mechanisms discussed so far for temporary anion resonances all involve one-electron processes. In a MO picture, the two-electron process requires the weak coupling between Slater determinants that arises from electron correlation, which is small in comparison to the determinantal energy levels themselves, hence the two-electron process is much slower. Feshbach resonances thus tend to be longer lived as compared to shape resonances.[186]

Next consider that a minimal set of requirements for DEA consists of the following.[12]

1. A resonance lifetime $\gtrsim 10^{-14}$–10^{-12} s.
2. A transient negative ion state that is dissociative in the Franck–Condon region of the neutral species.
3. At least one fragment of the dissociation products that has a positive EA, so that the dissociation channel is energetically allowed.

These requirements are fulfilled by the Feshbach resonance illustrated in Figure 15. (The final requirement, energetic accessibility, is fulfilled relative to the excited state ABCD*.) These requirements are also fulfilled by the

scenario depicted in Figure 1, which we may classify as a single-particle Feshbach resonance. Such states have sometimes been called *vibrational Feshbach resonances*. Note that in this case the anion is necessarily formed in a vibrationally excited state.

The distinction between a Feshbach resonance and a shape resonance for a negative ion can be stated succinctly in terms of whether M^- lies above (shape) or below (Feshbach) the energy of the neutral molecule, M. Stated differently: in the shape resonance case, M^- lies above its own continuum (that corresponding to $M + e^-$), while in the Feshbach case, M lies below this continuum. An example is shown in Figure 16, where we consider two isomeric forms of *p*-coumaric acid, which is a simplified chemical model of the chromophore in photoactive yellow protein.[187,188] For both the phenolate and the carboxylate isomers of this chromophore, the $S_1(\pi\pi^*)$ bright state lies above the adiabatic electron detachment threshold, hence the electronically excited state should be considered a resonance. However, the two isomers exhibit very different detachment processes. In the phenolate isomer (left side of Figure 16), the lowest detachment threshold corresponds to removing an electron from one of the π orbitals involved in the $\pi \rightarrow \pi^*$ ($S_0 \rightarrow S_1$) excitation, and in that sense the S_1 state lies above its own continuum and may be classified as a core-excited shape resonance. One expects the $^1\pi\pi^*$ state to be short-lived in this case. Meanwhile, for the carboxylate isomer (right side of Figure 16), the lowest

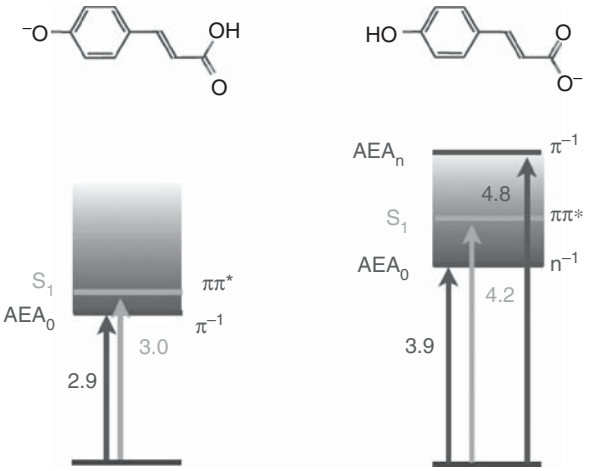

Figure 16 Schematic view of $S_0 \rightarrow S_1$ excitation in *p*-coumaric acid in its phenolate (a) or carboxylate (b) isomeric form. (Energies are given in electron volts.) In either case, the S_1 state lies above the anion's adiabatic detachment threshold and is thus embedded in a continuum of electron-detached states. The core-excited $\pi\pi^*$ resonance may be classified as a shape resonance (on the left) or a Feshbach resonance (on the right) depending on whether the low-lying continuum corresponds to detachment from the π system (a″ orbital) or from an a′ orbital that is not involved in the $\pi \rightarrow \pi^*$ excitation. Adapted with permission from Ref. 186; copyright 2013 American Institute of Physics.

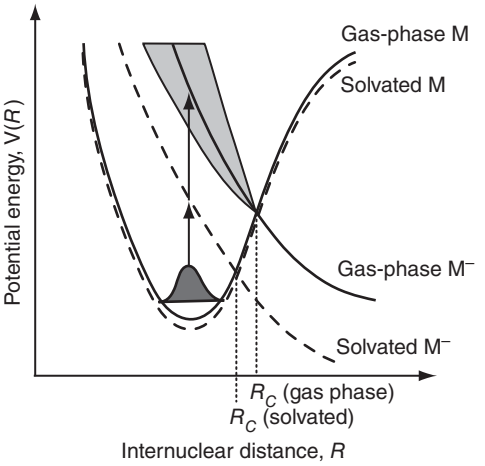

Figure 17 Qualitative depiction of how solvation might alter the solution-phase potentials (broken curves) of M and M^-, relative to the corresponding gas-phase potentials (solid curves). The shaded region indicates the resonance width of the gas-phase anion. Adapted with permission from Ref. 187; copyright 2004 Elsevier.

detachment threshold corresponds to removing an electron from an orbital with a′ symmetry that is not involved in the $\pi \rightarrow \pi^*$ transition. In this case, e^- detachment from the π system (indicated as π^{-1} in Figure 16) lies above S_1. From S_1, electron detachment from the a′ orbital is a two-electron process, and the carboxylate case is an example of a core-excited Feshbach resonance.

Finally, it bears mention that where anions are involved, solvation effects can often have a qualitative impact on the basic physical picture, especially in polar solvents where M^- is likely to be dramatically stabilized with respect to M. Polar solvation might, for example, convert an open channel, core-excited resonance $(M^*)^-$ into a core-excited Feshbach resonance by dragging the $(M^*)^-$ potential curve below that of M^*. In such a case, the solution-phase anion resonance would be expected to have a significantly longer lifetime as compared to its gas-phase analogue.[186]

Even in cases where solvation is not enough to stabilize the anion with respect to the neutral molecule, the solution-phase environment can have important consequences. Figure 17 depicts schematic potential energy curves for M and M^- in both the gas phase and in solution, with the environment stabilizing M^- much more than it stabilizes M. On forming the anion M^- from the neutral molecule, an autodetachment channel is available for $R < R_c$. Taking a semiclassical view of electron attachment, the resulting anion spends less time in the autodetachment region $R < R_c$ in solution than it does in the gas-phase case. This enhances the lifetime of the solvated anion relative to the gas-phase species, and possibly allows it to escape the region $R < R_c$ without suffering autodetachment.[186]

QUANTUM CHEMISTRY FOR WEAKLY-BOUND ANIONS

In this section, we discuss the ways in which weakly-bound anions place special demands on quantum chemistry calculations. It is presumed, in this discussion, that the anion M^- is a bound species (VDE > 0) at the molecular geometry in question, such that the application of bound-state quantum chemistry methodology is appropriate. Referring to the situation in Figure 1, bound-state methods are appropriate for the description of the anion AB^- only for $R > R_c$. For $R < R_c$, the neutral molecule is lower in energy, and application of bound-state methods to M^- is not appropriate. Electronic structure methods for temporary anion resonances are discussed later in this chapter.

Gaussian Basis Sets

Atom-Centered Basis Sets

For calculations involving anions, one should use basis sets augmented with additional diffuse basis functions. However, the diffuse exponents for standard augmented basis sets were optimized to describe small molecular anions[189] (CH_3^-, NH_2^-, OH^-, etc.) and or atomic anions,[189,190] so while these basis sets may be appropriate for describing *valence* anions, they are inadequate for the description of dipole-bound or other loosely-bound electrons. This criticism applies to all of the standard, singly-augmented basis sets, including Pople-style basis sets such as 6-31+G*, 6-31++G**, and their triple $-\zeta$ analogues, as well as the Dunning-style correlation-consistent basis sets aug-cc-pVXZ, for X = D, T, Q, …. (The aug-cc-pVXZ basis set will sometimes be abbreviated aXZ in this work.) That these basis sets are inadequate to describe weakly-bound anions can be seen clearly in Figure 18(a), which depicts the convergence of calculated VDEs for an isomer of $(H_2O)_{12}^-$ for which the VDE ≈ 0 in the basis set limit. Setting aside the density-functional calculations, which strongly overbind the electron for reasons discussed later in this chapter, we see that the VDE converges to about zero only after *four* diffuse shells have been added.

In the calculations reported in Figure 18, exponents for the additional diffuse shells are chosen in an *even-tempered* manner, meaning they are arranged in a geometric progression (differing by a common scaling factor), starting from the smallest exponent in the standard 6-31++G* basis set. Use of a geometric progression is intended to reduce numerical linear dependencies that may hamper self-consistent field (SCF) convergence,[192] although such problems are ultimately inevitable as system size grows, especially when numerous diffuse shells are required. In cases where the anion SCF calculation proves difficult to converge, one may try either using the neutral molecule's MOs as an initial guess for the anion's MOs, or alternatively, converge the anion SCF calculation

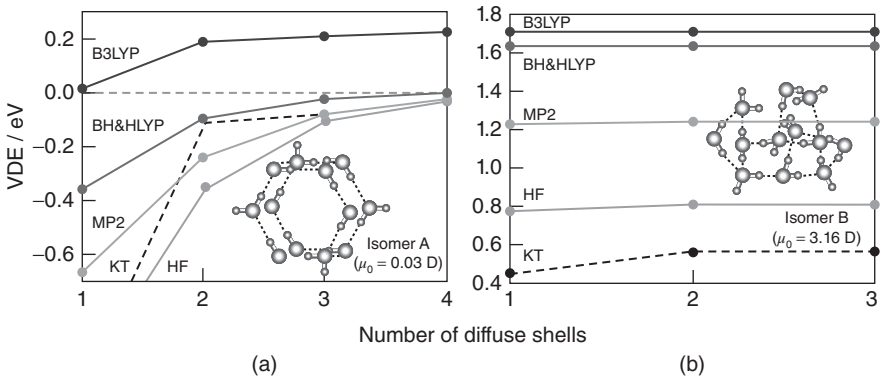

Figure 18 VDEs computed at various levels of electronic structure theory for two different isomers of $(H_2O)_{12}^-$, as a function of the number of diffuse shells included in the basis. The basis set is 6-31(1+,*n*+)G*, meaning one set of diffuse sp functions for the oxygen atoms and *n* sets of diffuse exponents (with exponents comprising a geometric progression) for the hydrogen atoms. The quantity μ_0 is the dipole moment of the underlying neutral $(H_2O)_{12}$ cluster, and "KT" denotes the Koopmans' theorem result, $-\varepsilon_{SOMO}$. Reprinted with permission from Ref. 191; copyright 2005 American Chemical Society.

in a less diffuse basis set and then use these MOs (in conjunction with basis-set projection) as an initial guess for the MOs in the target basis set.

The valence basis sets that one wishes to augment are not always even-tempered themselves, so Schaefer and coworkers[193,43] recommend choosing the scaling factor, κ, according to

$$\kappa = \frac{1}{2}\left(\frac{\zeta_1}{\zeta_2} + \frac{\zeta_2}{\zeta_3}\right) \qquad [20]$$

where $\zeta_1 < \zeta_2 < \zeta_3$ are the smallest (most diffuse) s- and p-function exponents in the valence basis set. The diffuse exponents are then taken to be $\kappa\zeta_1, \kappa^2\zeta_1, \kappa^3\zeta_1, \ldots$. Often, the exponents contained in the valence basis set are such that κ is roughly 1/4–1/3. Taking oxygen atom as an example, the formula in Eq. [20] affords $\kappa^{-1} = 3.65$ for 6-31G*, which is not so different from the ratio $\zeta_2/\zeta_1 = 3.20$ that is actually used for the diffuse exponent in 6-31+G*, where ζ_1 was optimized for Hartree–Fock calculations on valence anions.[189] Skurski et al.[192] have studied the addition of even-tempered diffuse functions in a systematic way, for applications involving very weakly-bound anions, and they recommend scaling the orbital exponents by a factor of 1/3–1/5, that is, $\kappa^{-1} = 3$–5. In the Q-Chem program,[194,195] for example, a scaling factor of $\kappa^{-1} = 3.2$ is used, by default, for additional diffuse functions in Pople-style basis sets.

This leaves open the question of how many additional diffuse basis functions should be included, and clearly the convergence behavior with respect to diffuseness of the basis set is very different for the weakly-bound

$(H_2O)_{12}^-$ isomer in Figure 18(a) than it is for the more strongly-bound isomer in Figure 18(b). To understand just how diffuse the basis needs to be, consider that at large electron–molecule separation (when the loosely-bound electron is far from the nuclei), the asymptotic form of the wave function is $\psi(r) \sim e^{-r/\lambda}$ where

$$\lambda = \frac{\hbar}{\sqrt{2m \times \mathrm{VDE}}} \qquad [21]$$

This is a rigorous and general result,[196,197] for both ground and excited states (provided that VDE is understood to be the detachment energy for the electronic state in question),[196] but can be understood using simple arguments. As $r \to \infty$, the electron tunnels out of whatever potential is responsible for its binding. For a simple model involving a square-well potential whose well depth is V_0, the characteristic length scale for the decay of the wave function into the classically forbidden region is

$$\lambda = \frac{\hbar}{\sqrt{2m(V_0 - E)}} \quad \text{(square well)} \qquad [22]$$

and it seems reasonable to replace $V_0 - E$ with the VDE. Alternatively, consider that the asymptotic behavior of the Hartree–Fock wave function also has the form of a decaying exponential, with[198]

$$\lambda = \frac{\hbar}{\sqrt{2m(-\varepsilon_{\mathrm{HOMO}})}} \quad \text{(Hartree–Fock)} \qquad [23]$$

For a bound anion, the value $-\varepsilon_{\mathrm{HOMO}} > 0$ furnishes the KT estimate of the VDE,[35] as discussed later in this chapter. Each of these arguments suggests that the VDE is directly related to the radial extent of the wave function.

Making a leap and replacing the wave function everywhere with its asymptotic form $\psi(r) \propto e^{-r/\lambda}$, with $\lambda = \hbar/(2m_e \times \mathrm{VDE})^{1/2}$ as suggested above, one may then compute the expectation value $\langle r \rangle$ for this wave function. The value thus obtained should provide at least a crude estimate of the mean electron–molecule distance. The mathematical result is

$$\langle r \rangle_{\mathrm{SOMO}} \approx \frac{3\hbar}{2\sqrt{2m_e \times \mathrm{VDE}}} \qquad [24]$$

This is an exact result for $\psi(r) \propto e^{-r/\lambda}$ but is only a crude approximation to the actual anion's wave function. It should work best for the singly-occupied molecular orbital (SOMO), hence the notation $\langle r \rangle_{\mathrm{SOMO}}$ in Eq. [24]. This result has been quoted previously,[2] albeit without the detailed justification presented herein. For what follows, we note that a computationally convenient form of Eq. [24] is

$$\langle r \rangle_{\mathrm{SOMO}} / \text{Å} \approx \frac{2.928}{\sqrt{\mathrm{VDE/eV}}} \qquad [25]$$

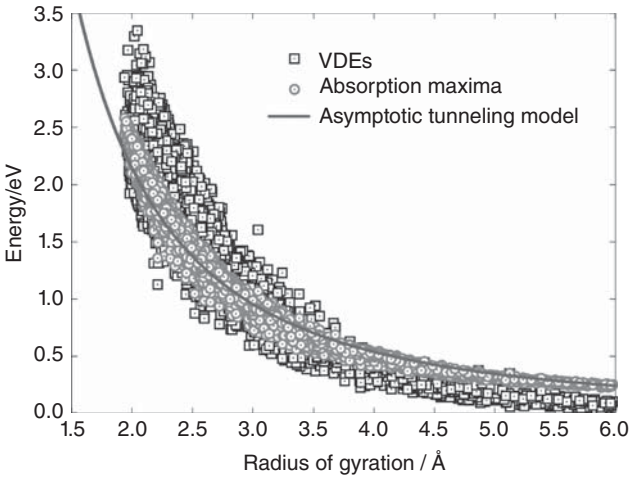

Figure 19 VDEs and electronic absorption maxima for $(H_2O)_N^-$ clusters ($20 \leq N \leq 200$), computed using a one-electron QM MM model[141] on a real-space grid. The "asymptotic model" denotes the VDE versus $\langle r \rangle$ relationship expressed in Eq. [25]. Adapted with permission from Ref. 95; copyright 2011 American Chemical Society.

The distance estimate in Eqs. [24] and [25] is derived only from the asymptotic form of the wave function, but data for a large number of $(H_2O)_N^-$ clusters suggest that this estimate is actually quite reasonable. Figure 19 plots VDEs for $(H_2O)_N^-$ clusters versus the *radius of gyration*, r_g, for a large number of cluster isomers ranging in size from $N = 20$ to $N = 200$.[95] The radius of gyration is defined as

$$r_g = \langle (\mathbf{r} - \langle \mathbf{r} \rangle) \cdot (\mathbf{r} - \langle \mathbf{r} \rangle) \rangle^{1/2} \qquad [26]$$

where the expectation value is with respect to some particular orbital, wave function, or density, as appropriate; r_g is a measure of the size of the probability distribution in question. The data in Figure 19 were computed using a one-electron QM MM model[141,95] rather than all-electron quantum chemistry (so r_g measures the size of the one-electron wave function), but this model has been shown to afford an accuracy of ~ 0.1 eV for VDEs as compared to MP2 benchmarks for clusters as large as $N = 32$.[141] Importantly, the one-electron wave function in these QM MM calculations is represented on a real-space grid as opposed to an atom-centered basis set, so there should be no question about whether a compact Gaussian basis set might skew the results for a diffusely-bound electron. The data in Figure 19 demonstrate that the quadratic relationship VDE $\propto r_g^{-2}$ that is suggested by Eqs [25] and [26] offers a fairly reasonable fit of the VDE data, especially for VDEs $\lesssim 1$ eV. (Note that the approximations underlying Eqs. [24] and [25] are expected to break down

when the VDE is large, because in such cases it is no longer justified to replace the entire wave function with its asymptotic form.)

To understand the implications for the selection of diffuse Gaussian exponents, consider that the full width at half maximum (FWHM) of a primitive Gaussian function of the form $\exp(-\zeta r^2)$ is

$$\mathrm{FWHM}(\zeta) = 2\left(\frac{\ln 2}{\zeta}\right)^{1/2} \approx \frac{1.665}{\zeta^{1/2}} \qquad [27]$$

Combining this with the estimated extent of the SOMO in Eq. [25] suggests that one ought to choose the smallest diffuse exponent such that

$$\frac{\zeta}{a_0^{-2}} \ll 0.09 \times (\mathrm{VDE/eV}) \qquad [28]$$

where a_0 denotes the bohr radius. (Gaussian exponents are traditionally quoted in atomic units.) The diffuse s function on the oxygen atom has an exponent $\zeta = 0.0845\ a_0^{-2}$ for the 6-31+G* basis set and $\zeta = 0.07896\ a_0^{-2}$ in the case of aug-cc-pVDZ (abbreviated "aDZ" hereafter). These values correspond to FWHMs of 3.03 and 3.14 Å, respectively. According to Eq. [28], or reading from the plot in Figure 19, one would expect such a basis to be appropriate only if the VDE is $\gtrsim 1$ eV. The $(H_2O)_{12}^-$ isomer depicted in Figure 18(b), for example, exhibits an MP2-level VDE of ≈ 1.2 eV, and in fact this VDE does appear to be converged with only a single set of diffuse basis functions, that is, a standard, singly-augmented valence anion basis set.

For a species like $(H_2O)_2^-$ where the VDE is < 0.05 eV,[199−201] Eq. [28] suggests choosing $\zeta \ll 0.0045\ a_0^{-2}$. This suggests that three or perhaps four additional diffuse shells, constructed as suggested above, would be required for such a species, depending on the choice of κ. (One might also worry about the quality of the quadrature grid that is used in density-functional calculations that employ very diffuse basis functions, but this does not seem to be an issue, and the default grids in various software programs appear to be sufficient, even when three or four diffuse shells are included.[191,202]) This estimate of three to four diffuse shells turns out to be similar to a recommendation previously provided[191] on the basis of a systematic study of VDEs for small $(H_2O)_N^-$ cluster anions, using 6-31(m+,n+)G* basis sets that include m sets of diffuse sp functions on the oxygen atoms and n sets of diffuse s functions on the hydrogen atoms, using a scaling factor $\kappa^{-1} = 3$. In the study in Ref. 191 the 6-31(1+,3+)G* basis set was found to be sufficient to afford VDEs at the MP2 and CCSD(T) levels that were, in most cases, within ~ 0.01 eV of the VDEs obtained in more diffuse basis sets. An exception was when the VDE was very small ($\lesssim 0.05$ eV), in which case the accuracy was estimated to be 0.03–0.04 eV.

On the other hand, 6-31(1+,3+)G* is not appropriate for high-accuracy calculations of the most weakly-bound anions. To converge VDEs to within ~ 0.001 eV of the basis-set limit, Skurski et al.[192] have shown that seven

diffuse shells (using $\kappa^{-1} = 3.2$) are required, for systems such as CH_3CN^- and $(H_2O\cdots NH_3)^-$ whose VDEs are both ≈ 110 cm^{-1} or 0.014 eV. This corresponds to smallest exponents on the order of 10^{-5} a_0^{-2}. Similar recommendations have been made by Gutowski et al.[113,203–205] For high-accuracy calculations, these authors employ aug-cc-pVDZ augmented further with either five or seven additional diffuse sp and diffuse d shells, depending on the value of κ, such that the smallest exponent is $\sim 10^{-5}$ a_0^{-2}. It is suggested that $\kappa^{-1} = 3.2$ is adequate if the neutral molecule's dipole moment, μ_0, is ≥ 6 debye, whereas $\kappa^{-1} = 5.0$ is more appropriate for $\mu_0 \sim 3.0$–4.5 debye.[205] The choice to augment aug-cc-pVDZ, as opposed to the roughly comparable 6-31++G** basis, originates in the observation that VDEs computed using Pople-style basis sets behave somewhat erratically as the number of diffuse shells is increased.[192,202]

Whether one chooses to apply this "enhanced augmentation" to 6-31+G* or to aug-cc-pVDZ, the fact that reasonable VDEs can be obtained using basis sets of double-ζ quality, using correlated wave functions, ultimately rests on a cancellation of errors, albeit a well-justified one. When VDEs for $(H_2O)_N^-$ clusters are computed at the MP2 level, for example, the differences between results obtained in the 6-31(1+,3+)G* and 6-311(1+,3+)G* basis sets are $\lesssim$ 0.01 eV.[206] No reasonable electronic structure theorist would expect such a cancellation in, say, a bond dissociation energy, or even an ionization energy for a closed-shell molecule computed at the same level of theory. The difference is the somewhat smaller correlation energy that is associated with the unpaired electron, which is better separated from the other electrons and therefore less strongly correlated. This is discussed in more detail later.

Although the convergence of VDEs provides a convenient means to evaluate basis set quality, one might object that if accurate VDEs are not the focus of a particular study, then the added computational cost of multiple diffuse shells is unwarranted. The danger in this reasoning – that compact basis sets might suffice, if only the computed VDEs can be ignored – is that overly compact basis sets *cannot* be trusted to describe the relative energetics of both dipole-bound anions *and* valence anions. Some molecules and clusters possess both types of states, at different geometries, and one must therefore consider whether a too-compact basis set – even one that might be quite reasonable for describing an anion whose VDE is large – may bias the calculation. Ignoring VDEs is also perilous because it leaves the user with no means to decide whether the anion in question is actually bound at the geometry in question, and whether that fact might change along a molecular dynamics trajectory, for example. If the anion is not bound, then the results of any bound-state quantum chemistry calculation are dubious at best.

As an example of how the lack of adequately diffuse basis functions can skew an entire potential energy surface, consider the case of $(H_2O)_2^-$. Calculations for this system on the basis of only singly-augmented basis sets suggest a stationary point corresponding to a $OH_2\cdots e^-\cdots H_2O$ structure,[207–210] in

which the two water molecules are arranged in either C_{2h} or D_{2d} symmetry, and the excess electron is apparently coordinated directly to all four O—H moieties. In an early paper that reported such a structure for $(H_2O)_2^-$, it was argued that inclusion of additional, more diffuse basis functions for the geometry optimization was not necessary, because the addition of such functions failed to change the contours of the SOMO in any qualitative way.[208] However, calculations using a more appropriate basis set, with three diffuse shells on each atom, later demonstrated that the $OH_2 \cdots e^- \cdots H_2O$ binding motif is unstable with respect to dissociation of the complex.[119,211] Using reasonable basis sets, the only stable structure identified for $(H_2O)_2^-$ corresponds to a dipole-bound $H_2O \cdots HOH \cdots e^-$ structure, with the electron bound to the positive-dipole end of a hydrogen-bonded water dimer.[211]

Considerations for the Condensed Phase

Convergence of the VDEs for $(H_2O)_{12}^-$ in Figure 18(b) suggests that when the VDE is larger, additional diffuse functions beyond the traditional set designed for valence anions (6-31++G*) do not alter the VDE by much. In condensed-phase systems, the presence of atomic centers is ubiquitous enough that one or a few diffuse shells may actually be enough to provide a converged wave function, even for solvated-electron systems where the unpaired electron resides in a solvent void (cavity) that lacks atoms, but which may be adequately covered via atom-centered basis functions. This is illustrated in Figure 20, which depicts a time-dependent density functional theory[215] (TD-DFT) calculation of the electronic absorption spectrum of e^-(aq), using the 6-31+G* basis set.[212] Comparison to the experimental spectrum[139] shows nearly quantitative agreement, despite the use of an atom-centered basis set with only a single diffuse shell. The odd electron in these calculations inhabits a void in the solvent, and the ground-state orbital depicted in Figure 20(b) clearly spans this cavity, despite the lack of multiple diffuse shells. Careful convergence tests, with respect to the diffuseness of the atom-centered basis set as well as the size of the QM region in these QM MM calculations, reveal that the 6-31+G* basis is sufficient to converge the first few excited states (including, at least, the three $1s \rightarrow 1p$ states), although basis-set effects are larger for more highly excited states.[162]

That the singly-augmented 6-31+G* basis appears to be sufficient for these e^-(aq) calculations is fortunate, because the multiply-augmented basis sets discussed above increasingly suffer from numerical linear dependencies as the system size grows. This is problematic in larger clusters, as linear dependencies tend to hamper SCF convergence and may be catastrophic in calculations designed to model condensed-phase systems. Convergence problems can sometimes be mitigated using tight thresholds for shell-pair formation and integral evaluation, but the computational cost may increase substantially as a result.

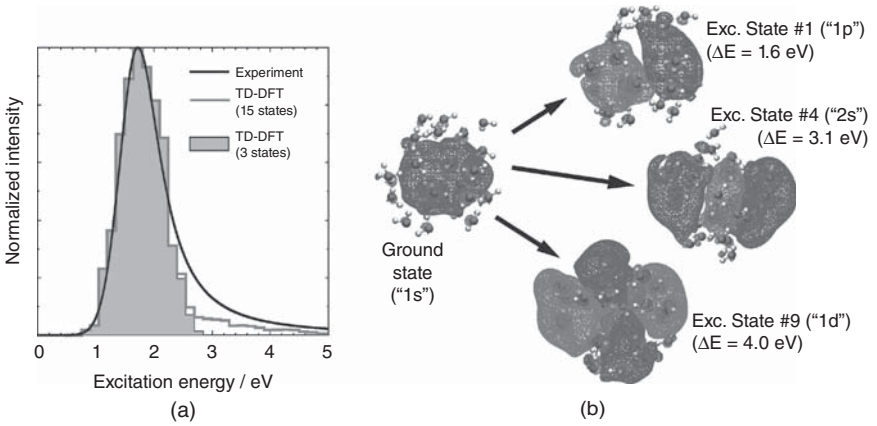

Figure 20 (a) Simulated absorption spectrum for $e^-(aq)$,[212] based on TD-DFT calculations at the LRC-μBOP/6-31+G* level, in comparison to the experimental spectrum from Ref. 139 (The LRC-μBOP functional is described in more detail later in this chapter; see Ref. 163 regarding the choice of functionals in TD-DFT). (b) Natural transition orbitals[213] (NTOs) for several excited states of this system,[15] with state labels 1s, 1p, and so on, corresponding to a "particle in a spherical box" model.[214] (For the particle in a spherical box eigenfunctions, the principal quantum number does not constrain the angular momentum quantum number, as it does for the more familiar example of the hydrogen atom, hence the lowest excited states of this system are 1p states, not 2p states.[214]) These plots demonstrate that the 6-31+G* basis adequately covers the cavity formed in the solvent; in particular, a cavity-centered SOMO is obtained for the ground state. Adapted with permission from Ref. 212; copyright 2010 American Chemical Society.

Gaussian basis sets designed specifically for condensed-phase calculations do exist, in which basis-function parameters have been optimized using a metric designed to minimize the appearance of linear dependencies.[216] However, these basis sets lack the diffuse functions needed to describe loosely-bound electrons. For *ab initio* molecular dynamics simulations of $(H_2O)_{32}^-$, Jungwirth and coworkers[217] found it necessary to augment such condensed-phase basis sets with an additional 1000 Gaussian functions centered on a $10 \times 10 \times 10$ Cartesian grid. The width of these functions was chosen to be ≈ 2.5 times the spacing between their centers.[218]

To appreciate another problem with highly diffuse basis sets, one must first understand that it is common practice to use MOs from the neutral molecule – call it M, as above – as an initial guess for the SCF calculation on M^-. This choice can greatly accelerate the anion calculation since the closed-shell SCF cycles are 50% less expensive and often provide an excellent guess if the anion is weakly-bound and only slightly perturbs the MOs of the neutral molecule. Moreover, insofar as both the M and M^- calculations are required to compute the VDE, nothing is lost by first computing the SCF wave function for M. However, for $(H_2O)_N^-$ isomers with *very* small VDEs

($\lesssim$ 0.1 eV, in this author's experience), such a guess occasionally converges to a different SCF solution, as compared to an unbiased guess for $(H_2O)_N^-$!

In addition, attempts to optimize the geometry of M^- sometimes access geometries in which the anion is unbound, which may lead to convergence failure in the SCF calculation. The regions of the potential surface where this problematic behavior occurs can be expected to proliferate as the VDE of M^- approaches zero. Such problems are usually avoided – for all the wrong reasons – by the use of overly compact basis sets, which is perhaps why the literature is rife with weakly-bound anion calculations using inappropriate basis sets. The VDEs reported in these studies are certainly incorrect, and the structures may be bogus as well.

Floating Centers

The discussion up to this point has considered only atom-centered Gaussian basis sets, possibly augmented by an expensive Cartesian grid of Gaussian functions. To avoid problems with linear dependencies, at modest cost, while still providing highly diffuse basis sets that can be used, for example, to describe dipole-bound anions of small molecules, one can employ *floating-center* basis functions. Here, a standard augmented basis set is further augmented with a set of diffuse functions placed on some alternative center that is treated as an atom with zero nuclear charge (a so-called "ghost atom"). The floating-center approach is effective for small, weakly-bound anions such as CH_3CN^- and $(H_2O\cdots NH_3)^-$, although diffuse basis functions of d symmetry are required to converge VDEs.[192] Analytic models of electron binding to a point dipole suggest that d functions in a single-center expansion should be even more important for systems with larger dipole moments,[219] although calculations on $(H_2O)_N$ clusters show that diffuse, atom-centered d functions have very little impact on VDEs.[191] Presumably, this is because the greater asymmetry of these clusters, as compared to CH_3CN^- or a point dipole model, allows linear combinations of diffuse s and p functions to mimic the angular flexibility that would otherwise be provided by diffuse d functions. It stands to reason that in a single-center expansion, functions with higher angular momentum will be necessary, as compared to what is required when using a multicenter expansion.

When the size of the nuclear framework of the molecule or cluster is small compared to the extent of the diffuse basis functions, it probably does not matter much where the floating center is positioned. In applications to $(H_2O)_6^-$, for example, Sommerfeld et al.[128] place a single set of diffuse functions on one oxygen atom, using an even-tempered progression out to a maximum FWHM of 80 Å. It is reported that the VDE depends only weakly on which oxygen atom is chosen as the center of this expansion.[128]

In a large molecule or cluster, however, a single floating center cannot be expected to replace atom-centered diffuse basis functions. In the absence

of these atom-centered functions, the floating-center approach is fundamentally unbalanced because some regions of space will be better covered by basis functions than other regions. Unless the electronic structure of the anion in question is well understood in advance, this technique is potentially dangerous for larger molecules of clusters because it necessarily biases the spatial location of the SOMO toward whatever region of space is best described by the floating center(s).[220] If using floating centers in larger systems, one should at the very least optimize their positions in any geometry optimization. (That is, the energy should be minimized with respect to the coordinates of *all* centers that support basis functions, including any ghost atoms.) In this context, it is worth noting that the presence of the floating centers will lead to artifactual vibrational frequencies, although these can be eliminated by increasing the (fictitious) mass of the ghost atom(s) so that their motion decouples from the actual vibrational degrees of freedom.[192]

Even so, the use of ghost atoms for larger molecules or clusters may present a biased description of the potential energy surface. It may be difficult to make a good *a priori* guess as to what the location of the floating center(s) should be, and geometry optimization only guarantees finding a *local* minimum with respect to the placement of these centers. A different initial guess for the position of the floating center(s) might easily lead to a prediction of an electron localized in a different region of space.

Orbital Isosurfaces

Given the extremely diffuse nature of the SOMO in a weakly-bound anion, an important but frequently overlooked consideration is how this orbital should be plotted for visual inspection and interpretation. Various software is available to render isocontour plots of MOs,[221–226] and an *isosurface* for the orbital ϕ is defined as the locus of points for which $\phi(\mathbf{r}) = c$, for some user-specified numerical value, c. A diligent author will faithfully report the value of c that was used to generate the isosurface, and while this does allow others to reproduce the same plot, it is basically meaningless from the standpoint of any physical interpretation. Moreover, any hand-waving arguments based on the spatial extent of the orbital thus plotted are dubious, insofar as the orbital can easily be made to appear larger or smaller by choosing a smaller or larger value of c, respectively.

While these comments pertain to orbital isosurface plots in general, the situation is particularly dire for diffuse electrons. In such cases, one should demand to know what fraction of the orbital density $|\phi|^2$ is encapsulated within a given isosurface plot. In other words, we need to know the fractional electron value,

$$f = \int_{\mathbf{r}\in V} d\mathbf{r}|\phi(\mathbf{r})|^2 \qquad [29]$$

that exists within the volume V defined by the orbital isosurface.

Figure 21 presents an example illustrating the danger of reporting isocontour plots with arbitrarily chosen contour values. Plotted in this example are

the Hartree–Fock/6-31(1+,3+)G* SOMOs for an isomer of $(H_2O)_{20}^-$ and an isomer of $(H_2O)_{24}^-$ that both have VDEs of ≈ 1 eV (MP2 level),[15] but which exhibit very different electron binding motifs. In one case, the electron is bound at the surface of the cluster and its wave function extends mostly into vacuum, whereas in the other case the electron resides in cavity formed within the cluster, wherein H_2O molecules have reoriented to point their O—H moieties toward the excess electron. In the latter case, it is tempting to conceptualize the excess electron as a small, quasi-spherical "ball of charge" in water, and the surfaces in Figure 21 demonstrate that it is possible to choose a value of c such that an isocontour plot reinforces this "ball of charge" (or particle-in-a-box[15]) picture. However, such a plot encompasses no more than 75% of the total probability density $|\phi_{SOMO}|^2$. When > 90% of the probability density is plotted, it becomes apparent that the SOMO extends well beyond the first solvation shell, for the cavity-bound electron, whereas in the surface-bound case the SOMO extends a considerable distance out into vacuum but does not penetrate the interior of the cluster to any significant extent.[206] Condensed-phase calculations of e^-(aq) in a solvent cavity also indicate that only ∼50% of the spin density $(\rho_\alpha - \rho_\beta)$ is contained within the cavity.[146]

This example demonstrates that isocontour values c chosen with no knowledge of the corresponding value of f may present a highly distorted physical picture. Similarly, the ubiquitous practice of side-by-side comparison

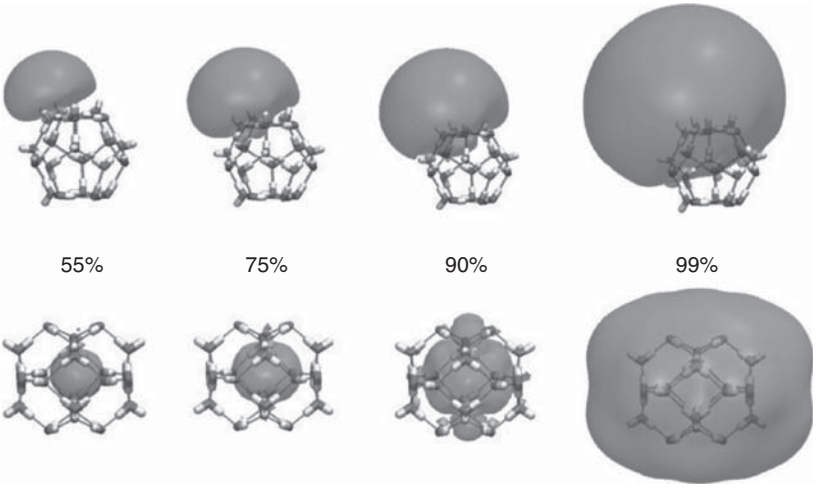

Figure 21 A series of isosurfaces computed at the Hartree–Fock/6-31(1+,3+)G* level that encompass ever-greater fractions of the SOMO for a surface-bound state of $(H_2O)_{20}^-$ top and a cavity-bound state of $(H_2O)_{24}^-$ bottom. The fraction f of the SOMO density, $|\phi|^2$, that is included within these surfaces is noted in the center. Both isomers exhibit VDEs of ≈ 1 eV at the MP2/6-31(1+,3+)G* level.[15] Reprinted with permission from Ref. 206; copyright 2008 American Chemical Society.

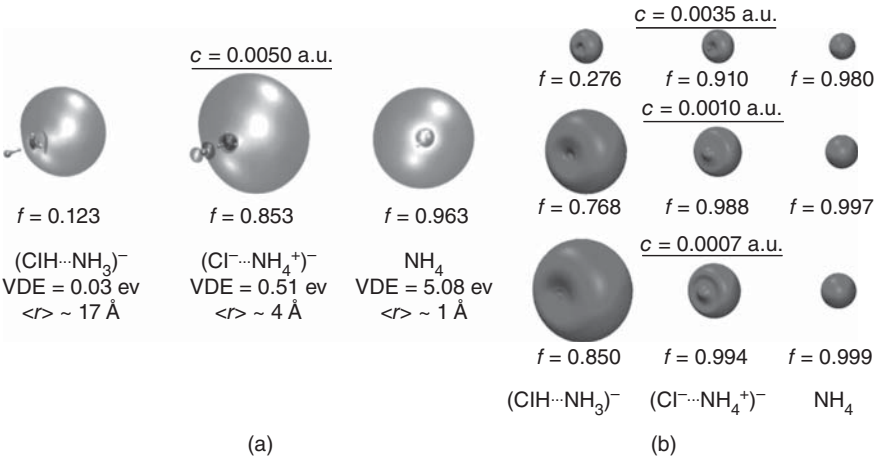

Figure 22 Isocontour plots of the SOMOs for three different loosely-bound electron systems studied in Ref. 227: the $(NH_3 \cdots HCl)^-$ dimer anion, the proton-transferred $(NH_4^+ \cdots Cl^-)^-$ isomer of the same dimer, and the charge-neutral NH_4 radical. (The last of these may be viewed as a Rydberg anion state of NH_4^+.) Panel (a) shows each SOMO plotted using a common isocontour value, $c = 0.005\ a_0^{-3/2}$. The corresponding fractions, f, of $|\phi_{\mathrm{SOMO}}|^2$ are also listed, along with an estimate of the electron–molecule distance for an electron in the SOMO, as determined using Eq. [25]. In panel (b), these SOMOs are plotted for three different isocontour values, c, and the corresponding values of f are listed as well. Adapted with permission from Ref. 228; copyright 2008 American Chemical Society.

of different orbitals plotted using the same isocontour value may be an unfair comparison, if the radial extent of the orbitals in question is quite different. Because the radial extent is governed by the VDE, comparing common isocontours for systems with very different VDEs is not appropriate. An example is shown in Figure 22, which plots isocontours of the SOMO for three species with very different VDEs. When plotted side-by-side using a common value of c, the SOMO isosurfaces for these three systems can convey misleading information about which of the orbitals is the most diffuse. For example, choosing either $c = 0.0035\ a_0^{-3/2}$ or $c = 0.0050\ a_0^{-3/2}$ (see Figure 22), the SOMO for $(Cl^- \cdots NH_4^+)^-$, a species whose VDE is only 0.03 eV,[227] appears to be slightly larger than the SOMO for the proton-transferred $(ClH \cdots NH_3)^-$ isomer of the same cluster, whose VDE is 0.51 eV.[227] However, the fraction of the electron that is contained in the two isosurfaces is quite different: > 85% of the density for the more strongly-bound species but < 30% of the electron density for the weaker binding isomer.

In view of these examples, side-by-side comparison of orbital isosurfaces for different molecules, clusters, or orbitals is appropriate only when comparing common values of f, not c.[229,228,206,15] Unfortunately, this wisdom has yet to percolate into common practice. When plotting several MOs from the

same molecule, this issue may be less pronounced because $\varepsilon_{\mathrm{SOMO}}$ controls the asymptotic decay of *all* occupied Hartree–Fock MOs, not just the SOMO (see Eq. [23]).[198] Nevertheless, best practice is to use consistent values of f whenever plotting orbitals side-by-side or when making "intuitive" arguments on the basis of the spatial extent of an orbital.

Whereas isocontour plots for arbitrary values of c are easy to generate from the output of most electronic structure programs, using readily available software,[221−226] plotting isoprobability contours for a specified value of f entails additional effort because volumetric data are required. Specifically, the function $\phi(\mathbf{r})$ must be computed on a grid and then integrated according to Eq. [29]. (In principle, this integration could be done internally within an electronic structure program, but to the best of this author's knowledge, no widely-used quantum chemistry package has yet implemented this feature.) Many electronic structure programs will output orbital and density data in the form of a so-called Gaussian cube file,[230] which has become something of an "industry standard" for storing volumetric data, insofar as this format can be read by a variety of visualization programs.[224,231,221] Nevertheless, the precise specification for "cube file" data does not appear to have been published in the literature.

This situation is rectified in Figure 23(a), which provides the format specification. The header portion of this file specifies the number of atoms (NAtoms) as well as their atomic numbers ($Z1$, $Z2$, …), coordinates ($x1$, $y1$, $z1$, $x2$, …), origin (*X*Origin, *Y*Origin, *Z*Origin), and axes of the volumetric grid. The number of cells (voxels) in each Cartesian dimension is specified as NVoxX, and so on, and the axes of each voxel must also be specified, so the values *X*Axis*X*, *X*Axis*Y*, and *X*Axis*Z*, for example, determine the orientation of the first (*X*) axis of the voxel relative to the molecular frame. The length of these vectors specifies the size of the voxel. Often, the voxel axes are simply aligned with the molecular frame, in which case the three axis vectors constitute a 3×3 diagonal matrix whose diagonal entries represent the spacings between grid points. (Note that all distances are in units of bohr.) Following the atomic coordinates come the volumetric data, also in atomic units. The snippet of code in Figure 23(b) suggests how these data values are arranged; note in particular the line break after each batch of Z points, one of which can be seen in the penultimate line of Figure 23(a).

Next, given an appropriately formatted cube file, the freely available OpenCubMan program[228] can be used to convert between c (isocontour value) and f (fraction of the electron encapsulated by the specified isocontour), and vice versa. Figure 24, which plots the radial decay of the SOMOs for the two weakly-bound cluster anions from Figure 22, illustrates how the algorithm works. Given a cube file representing $\phi_{\mathrm{SOMO}}(\mathbf{r})$ evaluated on a regular Cartesian grid, the algorithm first sorts the values of $\rho_{\mathrm{SOMO}}(\mathbf{r}) = |\phi_{\mathrm{SOMO}}(\mathbf{r})|^2$ into descending order, then numerically integrates ρ_{SOMO} starting from its maximum value, until the first point where the numerical integral equals or

(a)

```
Comment line #1
Comment line #2
NAtoms  XOrigin  YOrigin  ZOrigin
NVoxX   XAxisX   XAxisY   XAxisZ
NVoxY   YAxisX   YAxisY   YAxisZ
NVoxZ   ZAxisX   ZAxisY   ZAxisZ
Z1 0.00000 x1 y1 z1
Z2 0.00000 x2 y2 z2
       ...
ZN 0.00000 XN YN ZN
6.35606E-07  6.70235E-07  7.05477E-07  7.41220E-07  7.77344E-07  8.13717E-07
8.50200E-07  8.86644E-07  9.22893E-07  9.58785E-07  9.94153E-07  1.02883E-06
3.99687E-07  3.72104E-07  3.45449E-07  3.19779E-07  2.95144E-07  2.71584E-07
2.49128E-07  2.27797E-07
6.63832E-07  6.99866E-07  7.36503E-07  7.73622E-07  8.11090E-07  8.48765E-07
```

(b)

```
for (int i=0; i < Nx; i++){
    for (int j=0; j < Ny; j++){
        for (int k=0; k < Nz; k++){
            printf("%13.5E",data[i][j][k]);
            if (k % 6 == 5) printf("\n");
        }
        printf("\n");
    }
}
```

Figure 23 (a) Format specification for the "cube file" for storing volumetric data format. The file consists of a header that specifies the nuclei and the grid, followed by the data values at the grid points. All data are given in atomic units. (b) Inset: a snippet of C code that writes the data values in the appropriate order and format. This specification is consistent with that output of the Q-Chem electronic structure program[194,195] and has been tested for reading and visualization using the Visual Molecular Dynamics (VMD) program.[224] The column of zeros in the header file in panel (a) represents information that is not presently used by VMD.

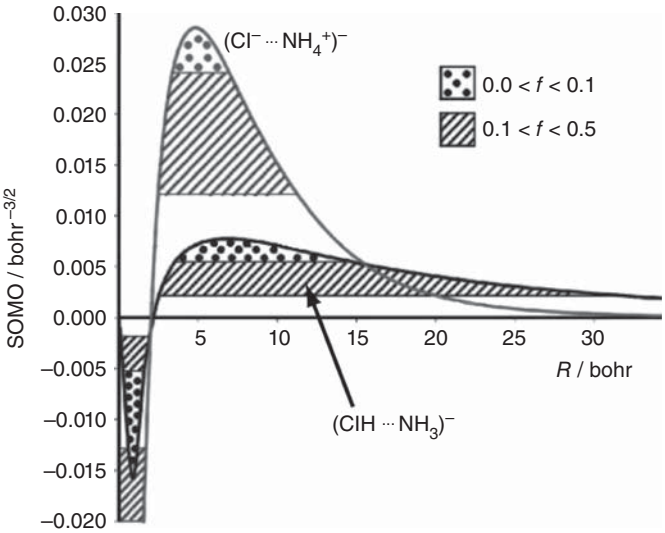

Figure 24 Radial plots of the SOMOs for the two weakly-bound anions from Figure 22, illustrating the $f \rightarrow c$ algorithm of Ref. 228. The dotted regions would be encapsulated by a 10% isoprobability contour and the hashed regions by a 50% isoprobability contour. Adapted with permission from Ref. 228; copyright 2008 American Chemical Society.

exceeds f. The value of $\phi_{\mathrm{SOMO}}(\mathbf{r})$ at that point is reported as the contour value, c.[228]

With a bit of experimentation, this procedure can be used to plot an isoprobability contour corresponding to a desired value of f, provided that the volumetric data are output on a sufficiently fine grid. For coarse grids, one may find that the process $f \rightarrow c \rightarrow f$ or $c \rightarrow f \rightarrow c$ does not yield completely self-consistent results (i.e., the final value may be slightly different from the initial value), but such discrepancies should disappear as the volumetric grid density increases.

Wave Function Electronic Structure Methods

Importance of Electron Correlation

Simple textbook results for IPs and EAs serve as a starting point for thinking about quantum chemistry calculations. If we assume that the nonionized molecule is described by a Hartree–Fock wave function, and furthermore if we neglect any relaxation of the MOs on electron attachment or detachment – that is, if we use the neutral molecule's MOs to construct a Slater determinant for the ionized species, removing an electron from the HOMO or adding an electron to the LUMO – then the corresponding approximate IP and EA expressions are known as KT:[35]

$$\mathrm{EA} \approx {}^{N}E^{N+1} - E_{\mathrm{LUMO}} = -\epsilon_{\mathrm{LUMO}} \qquad [30]$$

$$\mathrm{IP} \approx {}^{N-1}E_{\mathrm{HOMO}} - {}^{N}E = -\epsilon_{\mathrm{HOMO}} \qquad [31]$$

Here, ${}^{N}E$ represents the Hartree–Fock energy for the N-electron system, and the energies of the determinants formed either by adding an electron to the LUMO or removing one from the HOMO are denoted as ${}^{N+1}E_{\mathrm{LUMO}}$ and ${}^{N-1}E_{\mathrm{HOMO}}$, respectively. The fact that these energy differences are equal to (minus) orbital energies is an exact result within the model described above; the approximations (with respect to actual EAs and IPs) involve neglect of orbital relaxation and neglect of electron correlation.

A recent review article[2] suggests that the accuracy of KT results is typically ± 0.5 eV for both IPs and EAs, but often the accuracy for IPs is better than that for EAs owing to favorable error cancellation in the case of IPs. To understand this, consider that neglect of orbital relaxation must necessarily destabilize the ionized species (relative to an exact calculation), since the Hartree–Fock method is variational. At the same time, the correlation energy is extensive and therefore tends to be larger for the species that contains more electrons. This correlation energy will probably stabilize the species in question, relative to the Hartree–Fock prediction, by allowing electrons to avoid one another more successfully. For the IP case, then, orbital relaxation would decrease (stabilize) ${}^{N-1}E_{\mathrm{HOMO}}$, while electron correlation is expected to decrease ${}^{N}E$ to a greater extent than it decreases ${}^{N-1}E_{\mathrm{HOMO}}$. The two errors thus partially cancel one

another. Szabo and Ostlund[35] report small-molecule examples for which KT IPs afford values within 0.1 eV of experiment. For the DNA nucleobases, KT IPs evaluated using modest basis sets are also found to be within 0.15 eV of experimental values.[232]

In the case of EAs, however, the species where orbital relaxation is neglected (the anion) is also the species having the larger correlation energy, so if both effects are included then the net result is to move ${}^{N}E$ further away from ${}^{N+1}E_{\mathrm{LUMO}}$. As such, errors in KT EAs tend to be much larger than errors in IPs, perhaps $\sim$1 eV for EAs.[3] Empirical scaling of the KT EAs has been suggested,[232,124] although it is probably appropriate only across a narrow range of similar molecules. For example, the anion resonances in a series of substituted cyanoethylenes,[233] which can be determined experimentally by electron transmission spectroscopy,[184,185,2] are a good fit to the expression

$$\mathrm{VAE}_{\mathrm{expt}} = 0.74\varepsilon - 2.0 \text{ eV} \qquad [32]$$

Here, $\varepsilon > 0$ is an orbital energy (equal to the KT prediction of the VAE), computed in Ref. 233 at the Hartree–Fock/3-21G level. The VAEs measured experimentally and used to fit Eq. [32] range from 2 to 10 eV, meaning that the corresponding Hartree–Fock orbital energies lie in the range $\varepsilon \sim 5$–16 eV, according to Eq. [32]. In other words, the combination of orbital relaxation, electron correlation, and finite-basis effects (since 3-21G is far from the basis-set limit) modifies the KT prediction for the VAEs by 3–6 eV!

That said, and while KT EAs do still find some utility in stabilization calculations of temporary anion resonances (as discussed later in this chapter), for bound states of M^- there is little reason to rely on KT since Hartree–Fock calculations are nowadays computationally facile on large molecules, often in large basis sets. It is therefore easy to compute a "ΔSCF" value for the EA, which includes the effects of orbital relaxation, simply by computing separately the Hartree–Fock energies of M and M^-, *assuming that the latter is bound*. (If it is not, then neither the KT nor the ΔSCF value of the EA is reliable.) This raises an important point, namely, that one obtains a positive EA from KT only when $\varepsilon_{\mathrm{LUMO}} < 0$, and for very weakly-bound anions there may be no virtual orbitals with negative orbital eigenvalues. Simons[3] suggests that the orbital relaxation obtained in a ΔSCF calculation often amounts to $\sim$0.5 eV, whereas EAs predicted using KT might have errors of $\sim$1 eV, with the other 0.5 eV representing the effects of electron correlation. To do better than this for the calculation of EAs and/or VDEs, a correlated level of theory is required.

Much has been made of the critical role of electron correlation effects in the description of weakly-bound anions.[113,205,234,11,2,3] As with any electronic structure problem, electron correlation is always quantitatively important and occasionally qualitatively important. Cases where correlation is qualitatively important include certain anions with very small VDEs, where dipole binding effects alone (which might be reasonably well-described at the Hartree–Fock

level) do not afford a positive VDE, even for anions whose existence can be confirmed experimentally. Such examples will be discussed in due course, but it should be noted at the outset that cases where electron correlation changes the sign of the VDE almost always correspond to cases where the VDE is very small (< 0.1 eV). In such cases, an estimate VDE ≈ 0 that might be obtained at the Hartree–Fock level represents a rather small absolute error, quantitatively speaking.

This distinction brings to mind the infamous example of the dipole moment of the carbon monoxide molecule, a historically important problem whose story is told in Ref. 235. To summarize: the experimentally-determined dipole moment is ≈ 0.1 D and exhibits $C^{\delta-}O^{\delta+}$ polarization, whereas Hartree–Fock calculations in reasonable basis sets predict $\mu \approx 0.3$ D but with the opposite polarization.[236] Depending upon one's point of view, this is either an egregious, qualitative error in Hartree–Fock theory (wrong sign for μ!), or else a reasonable prediction that differs from experiment by only about 0.4 D. (Stated differently, Hartree–Fock theory *correctly* predicts that the CO dipole moment is small.) The VDEs of weakly-bound anions exist in a similar state of ambiguity. Since "chemical accuracy" (usually regarded as ∼1 kcal/mol or ≈ 0.04 eV) is achieved only with high-level treatments of electron correlation, one cannot expect that electron binding in any species whose VDE $\lesssim$ 0.04 eV will be described even qualitatively correctly in the absence of high-level treatments of electron correlation. On the other hand, an estimate of VDE ≈ 0 for such a species represents an error of $\lesssim$ 0.04 eV.

As pointed out previously in this chapter, VDEs are intensive quantities whereas the correlation energy is extensive. As such, it is sometimes argued that calculation of VDEs is especially difficult and sensitive to correlation effects.[2] Note, however, that other important chemical properties also do not scale with system size; reaction barriers, for example, tend to lie in the range 1–50 kcal/mol and depend on the local bonding environment more so than the overall system size. Similarly, electronic excitation energies for organic chromophores may be modulated in a chemically significant way by their environment, yet these excitation energies span a range of a few electron volts, largely independent of system size. In light of these facts, it is not altogether clear that calculation of VDEs is intrinsically more difficult than calculation of other chemically important energy differences.

Coupled-Cluster Theory

Rather than "walking up" the hierarchy of correlated wave function models, let us start from the top, with CC methods. For tutorial reviews of CC theory, see Refs. 38 and 39. Here, we simply note that the CCSD(T) method,[237] that is, CC theory with single and double excitations described self-consistently, and triple excitations treated perturbatively, is widely considered to be the "gold standard" of single-reference quantum chemistry. In conjunction with high-quality basis sets, this method often achieves "chemical accuracy" of $\lesssim$ 1 kcal/mol

for a variety of molecular properties and energy differences, including difficult ones like atomization energies where one cannot rely on error cancellation in computing the energy difference.[238] A self-consistent treatment of the triple excitations (CCSDT) is usually a small correction ($\ll 1$ kcal/mol).[238]

In defense of the assertion that EAs are fundamentally *not* significantly more challenging as compared to other energy differences in electronic structure theory, we first wish to make the case that the CCSD(T) method's reputation as an excellent benchmark level of theory is no less appropriate in the context of EAs and VDEs for weakly-bound anions. Considering EAs for the atoms H through Cl, where experimental values range from 0.28 eV for boron up to 3.61 eV for chlorine, complete-basis CCSD(T) results are in excellent agreement with experiment, with the largest deviation being 0.051 eV for Cl.[239] Notably, chlorine has the largest spin-orbit correction (estimated at −0.037 eV) and the largest relativistic correction (estimated at −0.015 eV) of any of the atoms H—Cl in the periodic table, and when these corrections are included, the discrepancy with experiment is reduced to < 0.0004 eV.[239] Errors in EAs for the 3d transition metal atoms, computed at the CCSD(T)/CBS level (where "CBS" denotes extrapolation to the complete basis set limit), are < 0.3 eV (or < 7 kcal/mol) in all cases. These errors are comparable in magnitude to the relativistic corrections.[240] Corrections for connected triple excitations ($E_{\mathrm{CCSDT}} - E_{\mathrm{CCSD(T)}}$) are no larger than 0.034 eV, and corrections for perturbative quadruple excitations ($E_{\mathrm{CCSDT(Q)}} - E_{\mathrm{CCSDT}}$) are < 0.01 eV.[240]

Although not directly relevant to CC theory *per se*, we mention in this context the performance of composite methods, including the W1 and W2 methods,[241,242] the Gaussian-3 (G3) method,[243−245] and the CBS-4 and CBS-Q methods.[246−249] These methods are "composites" in the sense that they combine the results of a variety of different levels of electronic structure theory, including vibrational zero-point energy and spin-orbit corrections, in an effort to design an overall computational strategy that can achieve $\lesssim 1$ kcal/mol accuracy for equilibrium thermochemistry. (The W1 and W2 methods even target "spectroscopic accuracy" of ~ 1 kJ/mol.[241,250]) For main group atoms and small molecules, the W1 and W2 methods predict AEAs with an accuracy of < 0.1 eV as compared to experiment.[242] The accuracy for AEAs predicted by the G3 method is 1.0–1.5 kcal/mol, or again better than 0.1 eV,[251,245] and the CBS-4 and CBS-Q methods perform similarly.[246] (Error statistics for several of these composite methods are summarized in Table 2.) The point of this brief digression about composite methods is to reinforce the idea that, as with CC methods, electronic structure models that are known to be accurate for thermochemistry are also accurate for AEAs.

Composite methods are designed for *equilibrium* thermochemistry, not for mapping out potential energy surfaces, so we now return to a discussion of CC methods and consider some cases involving prediction of VDEs for weakly-bound anions. Consider the case of $(H_2O)_2^-$, for example. The best available calculation for the VDE of the *trans* isomer (depicted in Figure 5)

Table 2 Error Statistics for Adiabatic EAs Computed by Various Composite Methods, for the 27 Atoms and Small Molecules in the G2-1 Data Set[a]

Method	Reference for Theory	Errors (eV)			
		Mean	MAD[b]	RMS[c]	Max[d]
G3[e]	243	0.031	0.049	0.065	0.182
G3(MP2)[e]	244	0.035	0.058	0.076	0.195
CBS-4M[e]	246	−0.006	0.111	0.136	0.312
CBS-QB3[e]	246	0.031	0.055	0.065	0.117
W1[f]	241	0.009	0.016	0.019	0.051
W2[f]	241	0.008	0.012	0.014	0.039

[a] 252
[b] Mean absolute deviation (MAD).
[c] Root mean square (RMS) deviation.
[d] Maximum error for any of the 27 atoms.
[e] Error statistics taken from Ref. 246.
[f] Error statistics taken from Ref. 242.

is one performed at the CCSD(T)/aug-cc-pVDZ(6s6p6d) level, where the parenthetical indicates six additional diffuse shells on a floating center.[234] This calculation predicts a VDE of 0.039 eV, which should be compared to values of 0.045 ± 0.006 eV[199,200] and 0.030 ± 0.0004 eV[201] obtained from photoelectron spectroscopy. For the *cis* isomer, a CCSD(T)/aug-cc-pVDZ(5s5p5d) calculation affords a VDE of 0.013 eV,[234] in comparison to an experimental value of 0.017 eV,[253,254] the latter measured by field detachment of $(H_2O)_2^-$ in rare-gas clusters and extrapolated to the limit of zero rare-gas atoms. Table 3 provides several other examples, along with an energy decomposition that is discussed later in this chapter. Of the examples in Table 3, the largest difference between theory and experiment occurs in the case of $(HF)_2^-$, for which Jordan and Wang[11] cite "sizable discrepancies" between theory and experiment. CCSD(T)/aug-cc-pVDZ(5s5p5d) calculations for this dimer anion afford a VDE of 387 cm^{-1} (0.048 eV),[203] as compared to the experimental value of 508 cm^{-1} (0.063 eV).[255] These comparisons to experiment establish the limit of what it is possible to achieve with *ab initio* theory.

As with atomic EAs, comparisons to higher-level calculations suggest that correlation effects on VDEs beyond the CCSD(T) level are quite small for molecular anions.[113,203,204] Consider, for example, the notoriously challenging HNC^- and HCN^- anions,[234,256,257] whose binding energies are only ≈ 0.004 eV and ≈ 0.002 eV, respectively, with the VDE for HCN^- arising almost entirely from electron correlation effects.[256] For these two species, VDEs computed at the CCSD(T) level and the CCSDT level agree to within 0.001 eV.[257] The $(H_2O)_6^-$ anion provides another example: here, the VDE computed at the CCSD(T) level[258] lies within the statistical error bars of a quantum Monte Carlo (QMC) calculation,[259] the latter of which is free of basis-set artifacts and does not require truncation of the excitation level.

Table 3 Decomposition of *Ab Initio* VDEs into Physically Meaningful Components[a]

	Contributions to the VDE (cm^{-1})				
Energy Component	CH_3CN^-[b]	$C_3H_2^-$[b]	$(H_2O)_2^-$[c]	$(HF)_2^-$[d]	$(HF)_3^-$[e]
KT	53	55	111	165	950
ΔE_{relax}	3	8	7	14	104
$\Delta E^{(2)}_{disp}$	57	70	114	177	625
$\Delta E^{(2)}_{non\text{-}disp}$	−38	5	−10	−73	−227
$\Delta E^{(3)}$	4	−38	0	−3	−24
$\Delta E^{(4)}$	8	34	20	27	93
ΔE_{HO}	21	39	100	81	145
VDE[CCSD(T)][f]	108	173	312	387	1666
VDE(expt)[g]	93	171 ± 50	363 ± 48	508 ± 24	1613 ± 2420

[a]Reprinted with permission from Ref. 11 (copyright 2003 Annual Reviews); notation is explained in the text.
[b]From Ref. 113.
[c]From Ref. 234.
[d]From Ref. 203.
[e]From Ref. 204.
[f]Basis set is aDZ(7s7p8d) for CH_3CN^- and $C_3H_2^-$, aDZ(5s5p5d) for $(HF)_2^-$, and aDZ(4s4p4d) for $(HF)_3^-$.
[g]References to the experimental literature can be found in the relevant theory papers.

Thus, CCSD(T) calculations with basis sets as described above are capable of reproducing experimental VDEs within the accuracy of the experiments, and further electron correlation effects are typically smaller than experimental precision, even in cases where the latter is quite good. The cost of CCSD(T) calculations, however, grows as $O(N^7)$ with respect to system size, N, which quickly becomes prohibitive. Therefore, it is important to understand how more modest treatments of electron correlation can be expected to perform. The convergence of VDEs with respect to the treatment of electron correlation, using basis sets that should be saturated with respect to diffuseness, is illustrated in Table 4 for several small $(H_2O)_N^-$ isomers. Two different isomers of $(H_2O)_6^-$ are considered, with VDEs of 0.42 and 0.78 eV at the CCSD(T) level.[260] Note that VDEs computed at the MP2 level for the same two isomers, which are also listed in Table 4, differ from the CCSD(T) values by only 0.06 eV (15%) and 0.03 eV (3%), respectively.

The very weakly-bound $(H_2O)_4^-$ isomer in Table 4 exhibits a larger MP2 error: 0.14 eV or 73%. That the MP2 error tends to be larger for less strongly-bound isomers is a general trend that will we see again later. From the KT results ($-\varepsilon_{LUMO}$), it is clear that this particular anion is nearly unbound at the Hartree–Fock level. According to Eq. [23], the asymptotic decay of the SCF wave function goes like $\sim \exp(-\varepsilon_{SOMO} r)$, so if $\varepsilon_{SOMO} > 0$ then the SCF

Table 4 VDEs for Several $(H_2O)_N^-$ Isomers Obtained Using Various Wave Function Models[a]

	VDE (eV)		
		$(H_2O)_6^{-c}$	
Model	$(H_2O)_4^{-b}$	Isomer 1	Isomer 2
Koopmans' Theorem[d]	0.002	0.233	0.045
Hartree–Fock	0.003	0.259	0.254
MP2	0.051	0.361	0.750
CCSD	0.166	0.399	0.717
CCSD(T)	0.191	0.422	0.777
EOM-EA-CCSD	0.192	0.418	0.744
EOM-EA-CCSD(2)[e]	0.192	0.415	0.744
ADC(2)	0.192	0.400	0.748

[a]Reprinted with permission from Ref. 260; copyright 2012 American Chemical Society.
[b]Basis set is aug-cc-pVTZ(6s6p6d).
[c]Basis set is aug-cc-pVDZ(7s7p).
[d]VDE $= -\epsilon_{\mathrm{SOMO}}$.
[e]Uses MP2 amplitudes to construct the cluster operator.

wave function is not normalizable, and the application of perturbation theory is probably not appropriate, since the reference state is qualitatively wrong. In the particular example of the weakly-bound $(H_2O)_4^-$ isomer in Table 4, ϵ_{SOMO} remains slightly negative (bound), but clearly the Hartree–Fock determinant is approaching a regime where perturbation theory should be viewed with skepticism. CC wave functions, on the other hand, are far less sensitive to the choice of reference determinant,[261] and indeed the CCSD result (treating the singles and doubles self-consistently, as opposed to perturbatively) is a reasonable approximation to CCSD(T), much more along the lines of what is observed for the more strongly-bound $(H_2O)_6^-$ isomers.

Since the "(T)" correction is itself perturbative, one might reasonably question CCSD(T) results in cases where MP2 theory goes awry. Results quoted earlier for $(H_2O)_2^-$ and HCN^- suggest that this is not an issue, however, presumably due to the superior reference state provided by the $\exp(\hat{T}_1)$ orbital rotation[261] in CCSD. A more direct assessment is possible using CC methods that do not rely on the weakly-bound anion as the reference state. One such method is the "electron attachment" version[262] of equation-of-motion (EOM) CC theory with single and double excitations.[263] This method, which goes by the acronym EOM-EA-CCSD, uses the CCSD wave function for the closed-shell neutral molecule, M, as a reference state to compute the cluster operator $\hat{T} = \hat{T}_1 + \hat{T}_2$, and is therefore free of any concern regarding whether or not ϵ_{SOMO} for M^- is bound. The ground state of M^- is then obtained by configuration interaction with respect to the similarity-transformed Hamiltonian,

$$\hat{\bar{H}} = e^{-\hat{T}} \hat{H} e^{\hat{T}} \qquad [33]$$

in a "two-particle, one-hole" (2p1h) basis.[262] For $(H_2O)_4^-$, EOM-EA-CCSD and CCSD(T) results are nearly identical (see Table 4), which suggests that the CCSD(T) method is a reasonable one even for weakly-bound anions. Evidently, for this particular example the $\exp(\widehat{T}_1)$ orbital rotation operator is able to deal with any inadequacy in the reference state.

This *quantitative* agreement between EOM-EA-CCSD and CCSD(T) results may be fortuitous, however. An EOM-CCSD study of small-molecule EAs (in the range of 0.4–3.8 eV) found that the accuracy of EOM-EA-CCSD and EOM-IP-CCSD EAs is generally no better – and perhaps slightly worse – than the accuracy of a ΔCCSD approach, with the accuracy of the latter method being ≈ 0.3 eV.[262] This underscores a point made earlier: it is not completely clear whether EOM, Green's function, or electron propagator methods are intrinsically more accurate than standard methods that compute $E_{\text{neutral}} - E_{\text{anion}}$, assuming that: (i) each of the methods in question is extended to the same level of many-body theory, and (ii) size-extensive methods are employed for all calculations. Moreover, whereas the EOM-EA-CCSD calculations in Table 4 were performed in an effort to avoid a potentially problematic anion reference state,[260] it was noted in Ref. 262 that the EOM-IP-CCSD values in that study were in slightly better agreement with experiment as compared to the EOM-EA-CCSD results, by 0.05–0.10 eV on average. The EOM-IP-CCSD approach consists of a ground-state CCSD calculation on the anion, followed by an EOM calculation involving removal of an electron. Thus, the "IP" version of the method (EOM-IP-CCSD) uses orbitals optimized for the anion.

Similar accuracy (0.2–0.3 eV for valence ionization energies below ~20 eV) is available using propagator methods in conjunction with triple-ζ basis sets.[102,103] These propagator methods are known in the literature as the outer valence Green's function (OVGF) and partial-third order (P3) approximations.[102,103] With modern semidirect batching algorithms, these methods exhibit only fifth-order scaling ($o\nu^4$, where o and ν denote the number of occupied and virtual orbitals, respectively, whereas EOM-CCSD methods scale as $o^2\nu^4$), although long calculation times (due to numerous batches) or else large amounts of memory (to reduce the number of batches) may be required.[101] That said, where point-group symmetry is available, molecules as large as fullerenes (C_{60} to C_{144}), porphyrins, and phthalocyanines [e.g., $(C_{32}H_{12}N_8NiO_{12}S_4)^{4-}$] have been considered.[264–266]

Perturbation Theory

When the VDE of M^- is small, changes in the treatment of electron correlation can have qualitative effects, analogous to the case of carbon monoxide's dipole moment.[235] A significant development in the study of (very) weakly-bound anions was the recognition, in the late 1990s, that electron correlation effects sometimes do play a qualitatively important role in electron binding,[113,204,205,234] in the sense that they may make the difference

between electron binding or not binding. To interpret the physical origins of electron binding, Gutowski and coworkers[192,204,205] introduced a perturbative decomposition of the VDE, similar in spirit to the perturbative theory of intermolecular interactions[267,268] but with the loosely-bound electron serving as one of the "molecules." The method requires calculations involving triple excitations [MP4 and CCSD(T)] and is therefore applicable to small systems only, especially in view of the basis-set requirements for high-accuracy calculations. In a series of publications, Gutowski et al.[113,204,269,205,234] showed that (second-order) electron–molecule dispersion interactions – which are wholly electron correlation effects – make a significant contribution to the VDEs of a variety of dipole-bound anions, some of which are analyzed in Table 3.

Dispersion interactions are absent at the Hartree–Fock level and appear for the first time in second-order perturbation theory. Gutowski et al.[204,205] proposed that a subset of the terms in the MP2 correlation energy could be ascribed to dispersion interactions between the loosely-bound electron and the core molecular species, namely

$$\Delta E^{(2)}_{\text{disp}} = -\frac{1}{2}\sum_{i}^{\text{occ}}\sum_{ab}^{\text{virt}} \frac{|\langle \phi_a \phi_b || \phi_i \phi_{\text{SOMO}} \rangle|^2}{\varepsilon_a + \varepsilon_b - \varepsilon_i - \varepsilon_{\text{SOMO}}} \qquad [34]$$

This second-order dispersion correction represents the terms in the MP2 correlation energy that involve coupling of the transient dipoles induced by simultaneous excitation of the SOMO and one of the occupied MOs (ϕ_i) of the core molecular species. Because the electron repulsion integrals in Eq. [34] are antisymmetrized, $\Delta E^{(2)}_{\text{disp}}$ includes second-order exchange-dispersion interactions as well, in the language of symmetry-adapted perturbation theory.[268]

For each of the anions in Table 3 except $(HF)_3^-$, this second-order dispersion energy is larger than the VDE predicted by KT, and in all of the cases examined in Table 3 it is larger than the remaining terms in the MP2 correlation energy ($\Delta E^{(2)}_{\text{non-disp}}$). Thus, with the possible exception of $(HF)_3^-$, one can say that electron–molecule dispersion is actually more important in stabilizing these particular weakly-bound anions than is the electron–dipole interaction, and as such, these are cases where correlation effects are *qualitatively* important. Much of this importance is captured already at second order in perturbation theory. The third- and fourth-order corrections to the VDE ($\Delta E^{(3)}$ and $\Delta E^{(4)}$ in Table 3) are fairly small, as is the "higher-order" correction, ΔE_{HO}, that is assessed as the difference between fourth-order perturbation theory and a benchmark VDE computed at either the CCSD(T) or CCSDT level.[11] For each of the weakly-bound anions in Table 3, the sum total of corrections to the VDE beyond second-order perturbation theory is no larger than 0.03 eV.

These higher-order effects are the largest in $(HF)_3^-$, which also has the largest VDE of any of the anions considered in Table 3. Much larger VDEs can be realized in larger $(HF)_N^-$ clusters,[11,270] and Table 5 shows the results

of a perturbative energy decomposition for some examples. All of these are high-symmetry clusters in which the positive ends of the molecular dipoles have been oriented toward a common point, in an effort to construct small clusters with large VDEs. In the VDE decomposition, one important observation is that $\Delta E^{(2)}_{\rm disp}$ is larger than the orbital relaxation correction ($\Delta E_{\rm relax}$) in every case, where the latter is defined as the difference between the KT estimate of the VDE and the ΔSCF value. Gutowski et al.[205] argue that $\Delta E_{\rm relax}$ should approximate the second-order induction correction, that is, $\Delta E_{\rm relax}$ is the leading-order polarization correction, and insofar as this is true, the ratio

$$\text{ratio} = \frac{\Delta E^{(2)}_{\rm disp}}{\Delta E_{\rm relax}} \qquad [35]$$

provides an estimate of the relative importance of dispersion versus induction. For the weakly-bound $(HF)_2^-$ isomer in Table 5, one obtains a ratio of 10.5, echoing the large ratios found in other weakly-bound anions such as $(H_2O)_2^-$ (ratio = 16.3) and CH_3CN^- (ratio = 19.0).[11] However, for the more strongly-bound $(HF)_N^-$ clusters in Table 5, this ratio is more like 1.5, meaning that both the induction and dispersion corrections are quite substantive.

These observations led to a significant change in the thinking about dipole-bound anions, whose very name implies electrostatic binding and summons notions of charge–dipole models.[271,219] On the other hand, the second-order dispersion and non-dispersion corrections have opposite signs and thus partially cancel, for all of the $(HF)_N^-$ clusters in Table 5 as well as many of the weakly-bound anions in Table 3. Moreover, as the VDE increases so, too, does the fraction of the VDE that comes from electrostatic and second-order induction effects ($\Delta E_{\rm relax} - \varepsilon_{\rm LUMO}$), and higher-order correlation effects constitute a smaller fraction of the VDE in larger clusters. In fact, the total fraction of the VDE arising from electron correlation gets smaller as the VDE gets larger, as shown in the left-most column of Table 5. To some extent, this reflects the intensive nature of the VDE versus the extensive nature of the correlation energy, even if the clusters in Table 5 are much too small to probe the thermodynamic limit.

Still, the correlation contribution to the VDE for $(HF)_6^-$, while only 7.6%, is hardly negligible at 0.2 eV. Note, however, that the third-order corrections and the "higher-order" correction have similar magnitudes but opposite signs, so that $|\Delta E^{(3)} + \Delta E^{(4+HO)}| \leq 0.015$ eV for each of the $(HF)_N^-$ clusters in Table 5, even for the dimer anion whose VDE is only 0.053 eV. This suggests that perhaps progress can be made in larger molecular and cluster anions by application of MP2 theory, even in cases where the VDE is rather small. In fact, MP2/6-31(1+,3+)G* VDEs for both $(H_2O)_N^-$ clusters[191,270] and $(HF)_N^-$ clusters[270] are consistently found to be only ~0.030 eV smaller than CCSD(T)/6-31(1+,3+)G* values. Considering also the basis-set error, it is suggested that the MP2 values are probably in error only by ~0.03–0.05 eV.[191,270,202]

Table 5 Decomposition of *ab Initio* VDEs for $(HF)_N^-$ Clusters into Physically Meaningful Components[a]

	Point	Energy Components (eV)							% e^-
N	Group	KT	ΔE_{relax}	$\Delta E^{(2)}_{disp}$	$\Delta E^{(2)}_{non\text{-}disp}$	$\Delta E^{(3)}$	$\Delta E^{(4+HO)}$	VDE	Corr.[b]
	$D_{\infty h}$	0.012	0.004	0.042	−0.017	−0.000	0.013	0.053	70
	D_{3h}	0.244	0.159	0.427	−0.212	−0.017	0.032	0.633	36
	T_d	0.808	0.404	0.685	−0.427	−0.026	0.032	1.477	18
	D_{3h}	1.358	0.497	0.754	−0.513	−0.022	0.026	2.100	12
	O_h	1.931	0.556	0.797	−0.584	−0.018	0.010	2.691	8

[a]Adapted with permission from Ref. 11 (copyright 2003 Annual Reviews).
[b]Percentage of the VDE arising from electron correlation.

For $(H_2O)_N^-$ and $(HF)_N^-$ clusters, second-order many-body perturbation theory (MBPT2) based on Kohn–Sham (KS) orbitals, which we will call the MBPT2(KS) method, has been used to gauge the sensitivity of MP2 theory to the choice of reference determinant.[270,260] The functional used in Refs. 261 and 271 is Becke's "half and half" exchange functional[272] (BH&H) in conjunction with the Lee–Yang–Parr (LYP) correlation functional:[273]

$$E_{xc}^{\mathrm{BH\&HLYP}} = 0.5E_x^{\mathrm{HF}} + 0.5E_x^{\mathrm{B88}} + E_c^{\mathrm{LYP}} \qquad [36]$$

Here, E_x^{HF} and E_x^{B88} denote the Hartree–Fock exchange energy and Becke's 1988 exchange functional,[274] respectively. The MBPT2(BH&H LYP) method has been applied to compute VDEs for a sizable database of $(H_2O)_N^-$ cluster isomers,[270] and in all but one case the canonical MP2 and the MBPT2(KS) values of the VDE were found to differ by no more than 0.15 eV. The outlier is a case where the Hartree–Fock determinant is unbound, and therefore the subsequent application of perturbation theory is ill-conceived.

Although it is not clear how general this MBPT2(KS) approach might be for other weakly-bound anions, for $(H_2O)_N^-$ clusters the bounds on the VDE that are obtained by MP2 calculations (lower bound) and MBPT2(BH&H LYP) calculations (upper bound) have recently been tested against benchmark results obtained using the ADC(2) method (second-order algebraic diagrammatic construction).[275,276] ADC(2) is a Green's function technique that, while based on second-order MBPT, is derived from a perturbative expansion of the VDE itself and should therefore be less circumspect than MP2 for very weakly-bound anions. Results for the $(H_2O)_4^-$ and $(H_2O)_6^-$ clusters considered previously (Table 4) show that VDEs computed at the ADC(2) level lie very close to EOM-EA-CCSD results and within 0.03 eV of CCSD(T) results. Table 6 compares ADC(2) and MBPT2 results for three isomers of $(H_2O)_{24}^-$. The Hartree–Fock SOMO eigenvalues for these three isomers are $\varepsilon_{\mathrm{SOMO}} =$ +0.03 eV (unbound), −0.05 eV (very weakly-bound), and −0.5 eV (moderately strong binding). ADC(2) results are shown in four high-quality basis sets, and variations in the VDE as a function of basis set are on the order of 0.05–0.08 eV. Despite the wide range of SOMO eigenvalues exhibited by these three isomers, the ADC(2) results are bracketed in each case by the MP2 and MBPT2(BH&H LYP) values of the VDE computed in the 6-31(1+,3+)G* basis set. In other words, the ordering of the computed VDEs is

$$\mathrm{MP2} < \mathrm{ADC(2)} < \mathrm{MBPT2(BH\&HLYP)} \qquad [37]$$

Since it is of interest to avoid the $O(N^6)$ cost of ADC(2) or EOM-EA-CCSD calculations in favor of the $O(N^5)$ cost of MBPT2 calculations, we note that the range of VDEs established by the MP2 and MBPT2(KS) results is ∼0.2 eV for the two cases where the Hartree–Fock wave function is bound. These bounds can be improved by the empirical scaling

Table 6 VDEs (in eV) for Isomers of $(H_2O)_{24}^-$, Computed at Various Levels of Theory[a]

		Isomer[b]		
Method	Basis set	$4^{14}6^4$B	$5^{12}6^2$C	$4^6 8^6$B
$-\varepsilon_{SOMO}$ (Hartree–Fock)	6-31(1+,3+)G*	−0.027	0.054	0.544
MP2	6-31(1+,3+)G*	0.004	0.136	0.575
MP2, correlation, scaled[c]	6-31(1+,3+)G*	0.004	0.192	0.601
ADC(2)	aDZ(7s7p)	0.147	0.132	0.626
ADC(2)	aDZ(6s6p6d)	0.162	0.194	0.636
ADC(2)	aTZ′(7s7p)[d]	0.199	0.170	0.687
ADC(2)	aTZ′(6s6p6d)[d]		0.212	
$-\varepsilon_{SOMO}$(BH&HLYP)	6-31(1+,3+)G*	−0.136	0.027	0.136
MBPT2 (BH&HLYP)	6-31(1+,3+)G*	0.346	0.362	0.726
MBPT2 (BH&HLYP), scaled[e]	6-31(1+,3+)G*	0.302	0.316	0.632

[a]MP2 and MBPT2 results from Ref. 270; ADC(2) results from Ref. 260.
[b]Isomer labels from Ref. 270.
[c]MP2 correlation energies scaled by 1.053 (see Ref. 270).
[d]The aTZ′ basis (Ref. 260) removes the most diffuse shell from aug-cc-pVTZ (aTZ).
[e]MBPT2(KS) total energies scaled by 0.8715 (see Ref. 270).

of the MBPT2 energies based on CCSD(T) results for small cluster anions, as described in Ref. 270. Upon scaling in this manner, the spread between the MP2 and MBPT2 VDEs is only slightly larger than the magnitude of the ADC(2) basis-set effects.

The unbound Hartree–Fock case is an exception. Here, the range of VDEs established by MP2 and MBPT2 calculations is 0.3 eV even after scaling, although these results continue to bracket the ADC(2) results. Although the range of VDEs is only a bit larger than in the previous two cases, the SOMO is unbound at both the Hartree–Fock and BH&HLYP levels, and therefore application of perturbation theory is inappropriate for this particular isomer. It is also not surprising in this case that the SOMO obtained from a Hartree–Fock calculation differs qualitatively from the one that is obtained using BH&HLYP,[270] since both SOMOs are crude approximations to a plane wave.

The accuracy of the MP2 results rests on the fact that the *differential* correlation energy associated with the unpaired electron is reasonably small in the case that the unpaired electron is loosely-bound.[270,206,15] Let us denote this differential correlation energy for M^- as

$$\Delta E_{corr}(M^-) = E_{corr}(M) - E_{corr}(M^-) \qquad [38]$$

Unlike the total correlation energy (E_{corr}), which is extensive, the quantity ΔE_{corr} is an *intensive* property. How big should one expect ΔE_{corr} to be? An

oft-cited order-of-magnitude estimate of the correlation energy in a generic molecular system is 1 eV per electron pair. This estimate originates in accurate variational calculations for helium atom, for which $E_{corr} = 1.14$ eV.[277] An additional data point comes from an essentially exact calculation (in a triple-ζ basis set) for the equilibrium geometry of H_2O, which affords a correlation energy of 1.40 eV per electron pair.[278] Thus, one may expect at least 1 eV of correlation energy for electrons paired in valence MOs.

The differential correlation energy in Eq. [38] has been studied for $(H_2O)_N^-$ and $(HF)_N^-$ cluster anions,[270,206] where it is found that $\Delta E_{corr} \lesssim 0.3$ eV, independent of cluster size but increasing essentially linearly with the VDE. This behavior is demonstrated for $(H_2O)_N^-$ clusters in Figure 25. The increase in ΔE_{corr} with increasing VDE makes sense in light of the fact that the VDE is a measure of the mean electron–cluster distance, and the linear relationship that is observed in small clusters is preserved in surface-bound isomers of $(H_2O)_N^-$ that are at least as large as $N = 18$.[206,15] Only for cavity-bound isomers of $(H_2O)_N^-$ in larger clusters, where the SOMO has significant overlap with numerous H_2O molecules, does ΔE_{corr} begin to approach values of 0.5–0.6 eV.[206,15] Such values are closer to – but still smaller than – what one should anticipate for an electron in a doubly-occupied MO. This is consistent with the notion that spatial separation between the SOMO and the other occupied MOs reduces the magnitude of correlation contributions to the VDE, as compared to the correlation contribution to the IP of a closed-shell molecule.

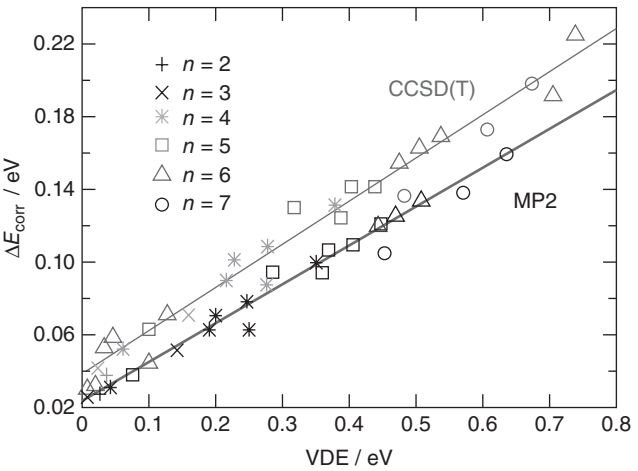

Figure 25 Correlation energy associated with the unpaired electron, ΔE_{corr} (Eq. [38]), computed at either the MP2/ or CCSD(T)/6-31(1+,3+)G* level for various isomers of $(H_2O)_N^-$. Reprinted with permission from Ref. 270; copyright 2006 the PCCP Owner Societies.

Large Systems and the Solution Phase

Our discussion of correlated wave function techniques demonstrates that accuracy sufficient to make quantitative comparisons with experiment is achievable using standard CC methods that work well in other contexts, albeit with some specialized basis-set requirements when weakly-bound anions are on the menu. Useful (if not quantitative) accuracy can be obtained at the MP2 level, provided that the VDE is $\gtrsim 0.05$ eV, the regime in which the Hartree–Fock determinant for the anion tends to be bound and thus normalizable. The reduced scaling of MP2 theory – $O(N^5)$ with respect to system size as compared to $O(N^6)$ for CCSD and $O(N^7)$ for CCSD(T) – offers the possibility of treating much larger systems. In 2008, this author[206] computed MP2/6-31(1+,3+)G*-level VDEs for cluster anions as large as $(H_2O)_{33}^-$ (≈ 1000 basis functions) using only modest computing resources (4 Gb of memory and 40 Gb of disk space per node, running in serial for systems with no symmetry). Today, MP2 calculations and even some higher-level methods are feasible in considerably larger systems,[264–266] by means of resolution-of-identity (RI) techniques and related methods,[279–281] which we shall briefly summarize.

At the heart of the RI-MP2 method is an expansion of the shell pairs $|\mu\nu)$ in an "auxiliary" basis of atom-centered Gaussians, $|K)$. This allows the four-index electron repulsion integrals required in MP2 theory to be expressed in terms of three-index integrals:[279]

$$(ia|jb) = \sum_{K,L}^{\text{auxiliary}} (ia|K)(K|L)^{-1}(L|jb) \qquad [39]$$

In this equation, which is exact if the auxiliary basis is complete, the quantity $(K|L)^{-1}$ is an element of the inverse overlap matrix (or some other metric matrix[279,282]) for the auxiliary basis, and the other quantities are electron repulsion integrals. While the formal scaling of the resulting RI-MP2 algorithm remains $O(N^5)$, the prefactor is reduced by up to a factor of ~ 20[282] such that the computational bottleneck is usually the iterative Hartree–Fock calculation rather than the post-SCF integral transformation. In practice, auxiliary basis sets $\{|K)\}$ are typically uncontracted and three to six times larger than the primary basis set, $\{|\mu)\}$, and extend to one unit higher in angular momentum. This ensures that the basis $\{|K)\}$ is sufficiently flexible to model the product functions $|\mu\nu)$. Using auxiliary basis sets that are specifically matched to – and optimized for – the primary basis set,[283,284] MP2 total energies are reproduced to within 30–60 μhartree per atom.[284,282] Relative energies and other energy differences are even more faithful to conventional MP2 results.

Timings for the Hartree–Fock part of the calculation can be dramatically reduced using either RI techniques (also known as *density fitting*[285,286]) to build the Coulomb and exchange matrices, or alternatively, dual-basis Hartree–Fock methods combined with RI-MP2.[287] The dual-basis RI-MP2 and density fitting RI-MP2 methods can routinely be extended to systems with ~ 50 atoms

using high-quality basis sets, and to systems with ∼100 atoms using smaller basis sets. As such, semiquantitative MP2-level VDE calculations should now be considered routine for systems of this size, although some care must be taken to modify and test the auxiliary basis sets for use with the highly diffuse primary basis sets that are required for weakly-bound anions. [Auxiliary basis sets designed for a floating-center treatment of $(H_2O)_6^-$ were developed in Ref. 288.] That said, and recognizing that efficient RI-MP2 gradient algorithms are also available,[289] for example, in Q-Chem,[194,195] geometry optimizations at the RI-MP2 level in systems with $\gtrsim 50$ atoms remain computationally demanding, and *ab initio* molecular dynamics simulations in this size regime are probably out of the question at present. For these tasks, one must rely on less expensive density-functional methods, which exhibit the same formal scaling as Hartree–Fock calculations and are amenable to the same density fitting and dual-basis acceleration techniques. The application of DFT to anions is considered later in this chapter.

The move toward larger systems allows one to consider solvation effects, by performing a quantum chemistry calculation involving the anion and one or more nearby solvent molecules. However, unless one is interested in relatively small gas-phase cluster anions (in which case the entire cluster might be described quantum mechanically), this sort of "microsolvation" approach is unlikely to describe solvation effects quantitatively or even semiquantitatively. For example, in an attempt to study e^-(aq), this author has computed VDEs for $(H_2O)_N^-$ clusters that were extracted from a bulk-phase simulation of e^-(aq), such that the cluster geometries are expected to be representative of electron binding motifs in bulk water. In these calculations, $N = 25–30$ water molecules were described using quantum chemistry while an additional 18,000 water molecules were described by classical point charges.[212,162] For the electronic absorption spectrum of e^-(aq), this rather elaborate QM/MM setup results in *quantitative* agreement with the spectrum measured experimentally in bulk water.[212,162] Nevertheless, the computed VDEs were no larger than 2.0–2.5 eV, whereas experimental measurements for the bulk-phase VDE of e^-(aq) range from 3.3 to 3.7 eV.[7–10] Evidently, the absorption spectrum is sensitive only to a correct treatment of the excess electron's wave function, which in turn depends on having a good description of the first two solvation shells into which this wave function penetrates. To predict the VDE, however, one must accurately describe the long-range Coulomb interactions in both charge states, which requires a much longer-range treatment of electronic reorganization.

Dielectric continuum solvation models can help to accelerate convergence toward the bulk limit. A simple, qualitative model for spherical solvent clusters was introduced in Eq. [6], in which the solvent's optical dielectric constant (ε_∞) provides a continuum correction for electronic reorganization. More general and more sophisticated dielectric continuum models exist, wherein the interface between the molecule and the continuum is allowed to be "molecule-shaped" rather than spherical (by means of a

union of atom-centered van der Waals spheres, for example), and where the polarization of the continuum is iterated to self-consistency alongside the solute's wave function. In quantum chemistry, such methods are typically known as *polarizable continuum models* (PCMs),[290−292] or alternatively, *self-consistent reaction-field models*.[172,293] A complete discussion of these models is beyond the scope of this review, and the reader is referred to several recent reviews of the subject.[290,294,295] For a discussion of the theoretical connections between various treatments of continuum electrostatics [e.g., the COSMO, GCOSMO, IEF-PCM, and SS(V)PE models], see Refs. 293 and 294, and for a discussion of how these models perform relative to empirical continuum models such as SM*x*,[291] see the work of Cramer, Truhlar, and others.[291,296−299]

Here, we note only that the properties computed from these models are *extremely* sensitive to how the "molecular cavity" (solute/continuum interface) is constructed, and that nonelectrostatic solvation effects are typically (though not always[297,300]) neglected in the PCMs such as COSMO, GCOSMO, IEF-PCM, and SS(V)PE that are derived from Poisson's equation for continuum electrostatics. In contrast, such effects are built into the empirical SM*x* models and are crucial to accurate prediction of solvation free energies.[291,297,298] It is unclear how the neglect of nonelectrostatic effects might impact the calculation of anion VDEs; cavitation effect should cancel, but dispersion effects may not, as the anion is intrinsically more polarizable. One may hope that these effects will disappear if a sufficiently large number of explicit solvent molecules is included as part of the QM solute.

One aspect of PCMs that does warrant mention in the context of VDE calculations is the issue of equilibrium versus nonequilibrium solvation.[301,172,290,294] Traditionally, this distinction has been considered in the context of electronic excitation energies,[302−307] where the solute wave function is excited in the presence of a continuum description of the solvent. In such a situation, "equilibrium solvation" – in which both ground- and excited-state wave functions are equilibrated separately and self-consistently to a continuum solvent whose dielectric constant is ε_s – is not the appropriate way to proceed. This is because the static dielectric constant (ε_s) includes the effects of orientational averaging over the solvent molecules, but these orientational degrees of freedom are too slow to readjust on the timescale of a vertical electronic excitation. Rather, for the excited state one should include a correction term in which the excited-state electron density is equilibrated self-consistently with the "fast" part of the continuum polarization, meaning that generated by ε_∞, but also subject to the electrostatic potential arising from the "slow" (orientational) polarization from the ground state, which is generated by $\varepsilon_s - \varepsilon_\infty$.[301,307] Other versions of this nonequilibrium correction have been derived and implemented in electronic structure codes,[306] but only the one described in Ref. 307 (which is based on much older work by Marcus[301]) is correct in the high-dielectric ($\varepsilon_s \to \infty$) limit.

Table 7 Aqueous-Phase Ionization Energies Measured via Liquid Microjet Photoelectron Spectroscopy and Calculated Using Continuum Solvation Models[a]

	Vertical ionization energy (eV)		
		MP2 + PCM	
Molecule	Experiment	Equil.[b]	Nonequil.[c]
Cytosine		6.6	7.9
Cytidine	8.3	6.6	7.8
CMP^{-}[d]		6.7	7.8
CMP^{2-}[d]		6.6	7.7
Thymine		6.6	7.9
Deoxythymidine	8.3	6.7	7.8
$dTMP^{-}$[d]		6.7	7.7
$dTMP^{2-}$[d]		6.6	7.7
$H_2PO_4^-$	9.5	7.6	8.9

[a]Reprinted with permission from Ref. 308 (copyright 2009 Chemical Society), except for the experimental $H_2PO_4^-$ ionization energy, which is from Ref. 136

[b]Using an "equilibrium" PCM that incorporates ε_s only.

[c]Using a nonequilibrium PCM that incorporates electronic reorganization using ε_∞.

[d]CMP, cytidine monophosphate; dTMP, deoxythymidine monophosphate.

We conclude this discussion with some data demonstrating the importance of equilibrium versus nonequilibrium solvation for aqueous-phase ionization. Table 7 shows VDEs for several aqueous-phase nucleobases, nucleosides, and nucleotides, computed at the MP2 level using both equilibrium and nonequilibrium PCMs. In the former case, the parent and the ionized species are separately equilibrated to a solvent whose dielectric constant is $\varepsilon_s = 78$, whereas in the latter case the nonequilibrium version of TD-DFT + PCM is used to estimate a correction on electron detachment such that only $\varepsilon_\infty = 1.78$ is used to relax the solvent polarization. (See Ref. 309 for details.)

For the examples in Table 7, VDEs computed with the equilibrium PCM are 1.0–1.3 eV smaller than the nonequilibrium values, the latter of which lie closer to experimental results obtained from liquid microjet photoelectron spectroscopy.[309,136] The ≈ 0.5 eV discrepancies that remain between the nonequilibrium theory and the experimental VDEs probably have myriad origins, not the least of which is likely the inherent limitations of a continuum description of the solvent. This comparison between theory and experiment serves as evidence of the complexity of solution-phase VDE calculations.

Density Functional Theory

A pedagogical introduction to KS DFT can be found in a previous chapter in this series.[40] While DFT methods are highly appealing in terms of their low cost, the description of anions by DFT, even strongly-bound ones like F^-, has

a controversial history that is summarized below. Until recently, the consensus view seemed to be that DFT methods were inappropriate for anions – especially in the context of VDE calculations – owing to problems associated with spurious self-interaction error (SIE).[46,310,308,311–313] A good historical overview of how the understanding of anion DFT calculations has evolved is given in a comprehensive review of anion DFT calculations by Schaefer and coworkers.[43] Summarizing briefly, there are two main objections to the application of DFT to anions.

1. DFT tends to yield *positive* HOMO eigenvalues, even for species with sizable EAs, suggesting that anions are unbound in DFT (in the KT sense).
2. SIE causes DFT to overstabilize half-filled orbitals, and in the context of electron attachment to a closed-shell molecule (forming a doublet radical anion) this means that the anion is overstabilized with respect to the neutral molecule, possibly drastically.

However, given the steady progress in functional development it is nowadays broadly recognized that DFT has an important role to play in anion electronic structure theory, even (with appropriate caveats, to be discussed) in the case of weakly-bound anions. At the same time, the literature is rife with egregious missteps and dubious conclusions because of ill-conceived DFT calculations for anions. In what follows, we attempt to sort this out and to address the two criticisms enumerated above.

Description of Anions in DFT

The effective one-electron potential in KS DFT is traditionally expressed as follows:

$$v_{\mathrm{KS}}(\mathbf{r}) = v_{\mathrm{ne}}(\mathbf{r}) + v_{\mathrm{H}}[\rho](\mathbf{r}) + v_{\mathrm{xc}}[\rho](\mathbf{r}) \qquad [40]$$

The three terms represent the sum of attractive nucleus–electron Coulomb potentials (v_{ne}), the Hartree potential

$$v_{\mathrm{H}}[\rho](\mathbf{r}) = \int d\mathbf{r}' \frac{\rho(\mathbf{r}')}{|\mathbf{r} - \mathbf{r}'|} \qquad [41]$$

that represents classical electron–electron repulsion, and the exchange-correlation potential (v_{xc}), which is the rug under which all complexity is swept. For an electron that is well separated from any nucleus, $v_{\mathrm{ne}}(r) \sim -Z/r$ in atomic units, where Z is the sum of all atomic numbers. Taking the lowest multipole moment of $\rho(\mathbf{r})$, we furthermore obtain $v_{\mathrm{H}}(r) \sim N/r$ in the same asymptotic limit, where N is the total number of electrons. Finally, the asymptotic form of the exchange-correlation potential can be shown to be $v_{\mathrm{xc}}(r) \sim -1/r$.[314] All together, the asymptotic KS potential is thus

$$v_{\mathrm{KS}}(r) \sim -\frac{Z - N + 1}{r} \qquad [42]$$

For electron attachment to a neutral molecule ($Z = N - 1$), one obtains $v_{KS}(r) \to 0$ asymptotically, consistent with previous remarks that there is no long-range $-1/r$ potential for electron attachment to a neutral molecule.

In Hartree–Fock theory, the nonlocal exchange operator $-\hat{K}$ replaces v_{xc} in Eq. [40], and the nonlocality recovers the correct form, $v_{xc}(r) \sim -1/r$, for an electron that is well separated from the other $N - 1$ electrons. The density-functionals in common use, however, are based on *local* exchange and correlation approximations, for which v_{xc} falls off with the density, which is to say, exponentially with distance. Note that this includes not just the local density (homogeneous electron gas) approximation, LDA, but also generalized gradient approximations (GGAs) that are still local potentials in the mathematical sense. (Sometimes GGAs are termed *semilocal* approximations, to distinguish them from LDA, but v_{KS}^{GGA} is still a local, scalar potential.)

The result is that, in practice, $v_{KS}(r) \sim -(Z - N)/r$ for a well-separated electron subject to a local KS potential. The basic problem is that $v_H(r)$ is the classical electrostatic potential for N electrons rather than $N - 1$, and approximate, local exchange potentials fail to fully cancel this spurious "self-interaction." As a result, an electron that is well separated from the molecule feels a repulsive potential generated by N electrons rather than $N - 1$. Setting $Z = N - 1$, the SIE leads to an anomalous $v_{KS}(r) \sim +1/r$ asymptotic potential for electron attachment to a neutral molecule. The electron–molecule potential is therefore repulsive at long range in approximate DFT!

As a result of SIE and the repulsive long-range potential that it engenders, anions that should be bound states in the real world are actually metastable resonances in the universe described by most approximate density-functionals. Figure 26(a) shows an example for the case of Li^-. On the basis of an accurate QMC density for Li^-, the Kohn–Sham equation can be inverted to determine the potential, $v_{KS}(r)$, whose ground-state orbitals reproduce the QMC density.[46] This may be considered the exact KS potential for this particular system, and indeed the asymptotic form of this potential is found to be $-1/r$, as it should be. This potential also binds an energy level corresponding to a stable Li^- ion with a $(1s)^2(2s)^2$ electron configuration. However, when the QMC density ρ is used to evaluate the KS potential

$$v_{KS}[\rho](r) = \frac{\delta E[\rho]}{\delta \rho} \qquad [43]$$

using an approximate density-functional $E[\rho]$, the potential rises above zero at intermediate distances and decays only very slowly back to zero [see Figure 26(b)].[46] Solution of the KS equations affords an energy level $\varepsilon = +0.80$ eV, which represents a metastable resonance since $v_{KS}(r) \to 0$ as $r \to \infty$. This point has been raised in various places, and used to suggest that DFT (with approximate functionals containing SIE) is not appropriate for the study of negative ions.[315,316,45] Notably, the density in KS DFT is represented in terms of a Slater determinant, so the considerations discussed

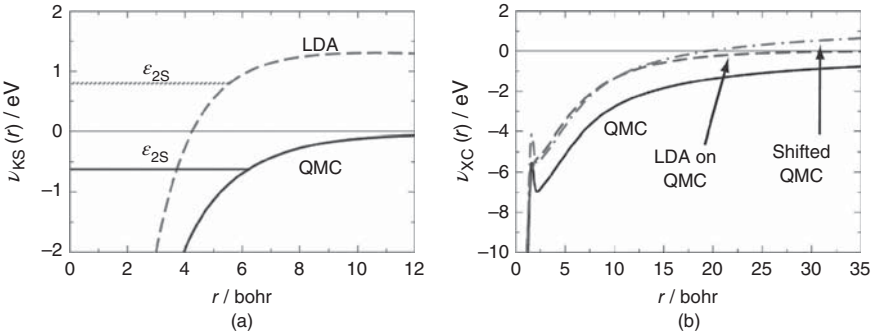

Figure 26 (a) The Kohn–Sham potential, $v_{KS}[\rho](r)$, for Li^-. The solid curve is the potential obtained from an accurate QMC density, for which the KS equations are inverted to obtain the corresponding KS potential. The broken curve is the potential obtained from the LDA functional, evaluated using the QMC density. (b) The exchange-correlation part of v_{KS} for Li^-, demonstrating that in the asymptotic region the LDA result (evaluated using the QMC density) differs from the QMC result by a roughly constant overall shift of the potential. Adapted with permission from Ref. 46; copyright 2010 American Chemical Society.

previously regarding positive orbital exponents in Hartree–Fock calculations are pertinent here as well: if $\varepsilon_{SOMO} > 0$ for a doublet radical anion, then in the limit of a complete basis set, the density for the "anion" M^- should converge to that of the neutral molecule M superimposed on a free electron.

The LDA version of $v_{KS}(r)$ that is plotted in Figure 26(a) has an outer classical turning point at $r = 17$ Å,[46] and one could therefore argue that in typical atom-centered basis sets, the lack of basis functions at such large values of r effectively forces the potential to go to infinity in those regions, and therefore the state that is metastable in the basis-set limit is transformed into a bound state in a finite-basis calculation. (In other words, the electron is trapped behind a very wide barrier, but the finite basis set does not allow one to notice this fact or to sample regions beyond the barrier.) *Extremely* diffuse basis sets may be required to detect this behavior. For example, DFT calculations on F^- show that ε_{HOMO} appears to converge to a positive value, even when the aug-cc-pV5Z basis is further augmented with an even-tempered progression of diffuse p functions out to $\zeta = 2 \times 10^{-5}\ a_0^{-2}$, corresponding to a FWHM of 197 Å.[44] However, with diffuse functions out to $\zeta = 10^{-10}\ a_0^{-2}$ (FWHM $> 9 \times 10^4$ Å), the HOMO eigenvalue converges to zero from above.[317] In the latter calculation, only a fraction (14%) of an electron is transferred in the asymptotic region, so that the converged DFT solution describes the system as $F^{0.86-} + 0.14\ e^-$.[317]

At the same time, these extra diffuse functions change the energy (and therefore the computed EA) only modestly, if at all, and DFT values for EAs are often not *disastrously* wrong,[43] even if the accuracy may be insufficient for the study of weakly-bound anions. (The accuracy of approximate DFT methods is discussed in more detail below.) This apparent paradox between predicted

"ΔSCF" EAs that are often quite reasonable, but HOMO energy levels that are unbound, can be explained by noting that the LDA potential $v_{KS}[\rho](r)$, evaluated using the QMC density, differs by a roughly constant shift from the QMC potential itself, at least outside of the core region [Figure 26(b)].[46] Note that the KS potential is arbitrary up to a constant. Moreover, orbital energies play different roles in Hartree–Fock theory (where the Slater determinant is intended as a genuine approximation to the wave function, and the HOMO–LUMO gap approximates the "fundamental gap", IP – EA) as compared to Kohn–Sham theory (where the Slater determinant represents a fictitious reference system, and the HOMO–LUMO gap approximates the "optical gap," or in other words the lowest electronic excitation energy).[318] Together, these observations suggests that a positive HOMO eigenvalue is not automatically fatal in KS DFT, nor is it a sign that the DFT result must be rejected out of hand.[46] That said, if the basis set extends beyond the turning point in the potential, then the density *will* begin to resemble an unbound electron. In the case of F^-, the potential barrier is high enough and/or wide enough that this does not occur except in ludicrously diffuse basis sets. For weakly-bound anions, however, one cannot be certain that the situation will be equally favorable.

Performance of Standard Functionals

The situation described above implies that one cannot trust the approach to the basis-set limit for most anion DFT calculations. (In fact, the complete-basis limit may not be completely well-defined for anion DFT,[313] as it may correspond to fractional electron transfer to the continuum.[317]) One solution to the lack of a well-defined basis-set limit in anion DFT calculations is to compute orbitals using Hartree–Fock theory, where the anion's HOMO tends to be bound (except in cases of very weak electron binding) and then use the Hartree–Fock density to evaluate energy by means of a density-functional containing both exchange *and* correlation.[46,313] The results of such a procedure, as applied to the G2-1 set[252] of EAs, are shown in Figure 27. (The G2-1 set includes EAs for atoms and small molecules that range from ∼0 up to 3.6 eV, with most of the EAs in the data set being > 1 eV.) The figure compares self-consistent B3LYP predictions for the EAs to predictions obtained by computing the B3LYP energy of the Hartree–Fock density. Unfortunately, one cannot say that, on the whole, the composite procedure affords any clear improvement over self-consistent B3LYP calculations; the advantage is that the HF-B3LYP procedure has a well-defined basis-set limit that should bind the electron.

In light of previous discussion, positive HOMO eigenvalues do not appear to be fatal for DFT anion calculations, and thus another approach is simply to charge ahead but benchmark thoroughly. To this end, Schaefer and coworkers[43] have benchmarked the performance of numerous density-functionals and basis sets against a data set consisting of 91 AEAs that have been determined, using photoelectron spectroscopy, to an accuracy of better than ±0.09 eV. (On the

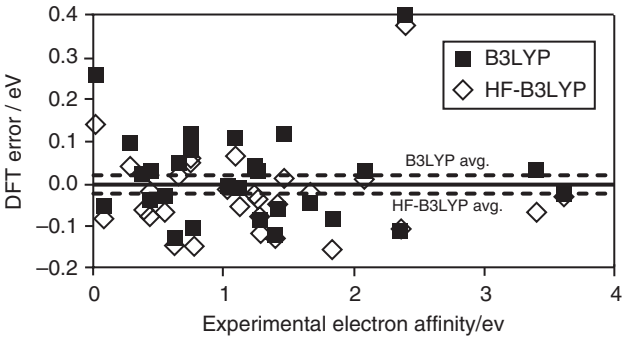

Figure 27 Errors in electron affinities (as compared to experiment) for self-consistent B3LYP/aug-cc-pVTZ calculations, and also for cases where the B3LYP energies for the neutral molecule and the anion were evaluated using Hartree–Fock densities (HF-B3LYP). The dashed horizontal lines are mean errors, which include considerable cancellation between over- and underestimation of the experimental EAs. The data set is G2-1,[252] except that the CN molecule is removed because of spin contamination in the Hartree–Fock determinant. Adapted with permission from Ref. 313; copyright 2011 American Institute of Physics.

Table 8 Error Statistics for DFT DZP++ Calculations of Adiabatic EAs[a]

	B3LYP	B3P86	BH&HLYP	BLYP	BP86	LSDA
Mean abs. error	0.14	0.59	0.24	0.14	0.18	0.68
	(0.16)	(0.60)	0.25	(0.15)	(0.19)	(0.67)
Max. abs. error	0.71	1.04	0.87	0.67	0.62	1.23
	(0.76)	(1.14)	(0.87)	(0.71)	(0.66)	(1.01)
Std. deviation	0.14	0.16	0.17	0.13	0.13	0.16
	(0.17)	(0.18)	(0.18)	(0.13)	(0.15)	(0.14)
% of AEAs that are overest'd	71	99	25	46	87	100
	(68)	(99)	(29)	(45)	(86)	(100)

Reprinted with permission from Ref. 43; copyright 2002 American Chemical Society.
[a]The data set is 91 atoms and molecules for which experimental uncertainties are no worse than ±0.09 eV, excluding SF_6. Values in parenthesis are vibrational zero-point energy contributions.

basis of the comprehensive review of 1,101 experimentally-determined AEAs in Ref. 43, this data set consists of essentially *all* of the accurately determined AEAs, as of 2002.) Error statistics for a subset of these functionals are reported in Table 8.

In general, the species in the data set are not weakly-bound anions, and the basis set used in these calculations (DZP++) reflects that. Although this basis does contain diffuse s and p functions on the heavy atoms, with different exponents, the ratio of those exponents is only, for example, 1.185 for carbon and 1.264 for oxygen,[43] rather than the scaling factors of ≈ 3.5 that

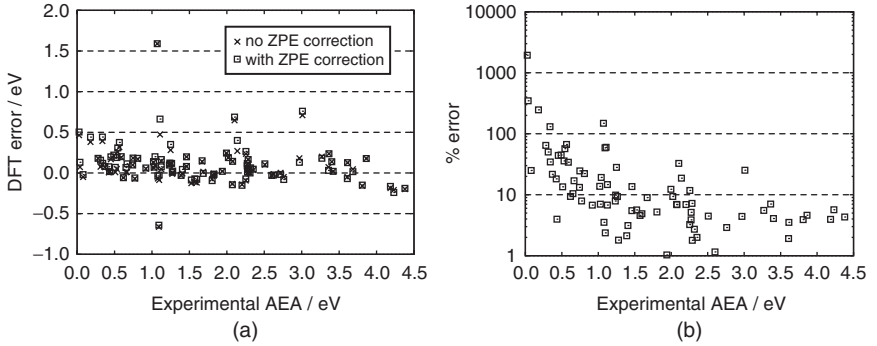

Figure 28 (a) Errors in B3LYP/DZP++ calculations of adiabatic EAs, either with or without a correction for the vibrational zero-point energy (ZPE), for 91 atoms and molecules whose experimental AEAs are known to be better than ±0.09 eV. (The outlier, with an error of 1.59 eV, is SF_6, which was excluded from the error statistics in Table 8.) (b) Percentage errors in the ZPE-corrected values, on a logarithmic scale. Both plots are based on data provided in Ref. 43.

were suggested in the discussion of basis sets presented earlier in this chapter. As such, the DZP++ basis set is effectively a singly-augmented one. (A variety of other singly-augmented basis sets were tested in Ref. 43 but did not afford results that were improved in any statistically meaningful way relative to DZP++ results.) The B3LYP/DZP++ and BH&HLYP/DZP++ results are fairly good, with mean absolute errors of 0.14 and 0.24 eV, respectively, although the maximum errors are 0.7–0.9 eV. The error for SF_6 is larger, and this molecule is therefore excluded from the statistics in Table 8. The authors of Ref. 43 attribute this larger error to the lack of f-type polarization functions in the DZP++ basis set.

The actual B3LYP/DZP++ errors are plotted in Figure 28(a) as a function of the magnitude of the experimental AEA. Somewhat surprisingly, the errors do not appear to be any larger for cases where the AEA is small (say, < 0.5 eV) as compared to cases where the AEA is several eV. Certainly, the *percentage* error is quite large for the more weakly-bound cases, and an error of ≈ 0.5 eV (toward overbinding) is fairly egregious for an anion that, experimentally, is almost unbound. Figure 28(b) shows that while B3LYP/DZP++ errors are *mostly* $< 10\%$ in cases where the AEA is larger than 1.5 eV, errors of 50–100% or more are not uncommon when the AEA is less than 1 eV. It is also worth noting that zero-point corrections have almost no effect on the error statistics, according to results in Table 8. Detailed examination of the B3LYP data from Ref. 43 shows that the difference between zero-point corrected and uncorrected AEAs is no larger than 0.05 eV for any molecule in the data set. Although one expects the zero-point corrections to be small (possibly vanishing) for dipole-bound anions, these are not well represented in the data set, hence the smallness of the zero-point corrections is perhaps something of a surprise. It may be attributable to the relatively small sizes of the molecules in

the data set (organic molecules no larger than tetracene, $C_{18}H_{12}$, and inorganic compounds no larger than SF_4).

The comprehensive benchmark study of Schaefer and coworkers,[43] which recommended B3LYP/DZP++ for EA calculations, is already more than a decade old at the time of this writing. Although B3LYP continues to enjoy widespread use in computational chemistry, considerable progress in functional development has transpired since the writing of Ref. 43 to the point that B3LYP is arguably no longer state-of-the-art. However, more modern functionals have not yet been tested exhaustively for EA and VDE calculations. Truhlar and coworkers[319−322] have compared a great many functionals, both new and old, against a small database, consisting of 13 AEAs for atoms and small molecules for which the data range from 1.3 to 3.6 eV.[97] (This is the data set that is listed in Table 1 of this chapter.) In compiling this data set, experimental AEAs were adjusted by subtracting out a harmonic DFT estimate of the zero-point energy, to obtain "zero-point exclusive" experimental AEAs.[97]

Mean unsigned errors (MUEs) for the AEAs in this data set, computed using a wide range of functionals, are shown in Figure 29. (Only functionals affording a smaller MUE than B3LYP are considered.) For context, the MUE for Hartree–Fock AEAs in this same data set is 1.2 eV,[320] an order-of-magnitude larger than the DFT errors, consistent with a value of $\Delta E_{\text{corr}} \sim 1$ eV for the differential correlation energy in Eq. [38]. This is larger than the values of ΔE_{corr} that were observed for $(H_2O)_N^-$ and $(HF)_N^-$ cluster anions, but many of the AEAs in the data set (Table 1) are quite sizable and correspond to placing an electron into a valence orbital, for which one should expect ΔE_{corr} to be closer to 1 eV.

In examining the error statistics in Figure 29, one should keep in mind that the MUE for B3LYP of Table 1 and Ref. 97 is 0.10 eV, as compared to the MUE of 0.16 eV that is obtained in the larger data set of Ref. 43. This comparison affords some estimate of how these MUEs might shift around if a different set of molecules was considered. With this in mind, the only functionals that really stand out in comparison to B3LYP are M11[325] and M08-HX,[326] which have MUEs of 0.04 and 0.06 eV, respectively, for the small data set. It is worth mentioning, however, that all 13 AEAs in this data set are included in the training set that is used to parameterize both of these functionals. (They are also included in the training set for the SOGGA11-X functional,[327] which according to Figure 29 also performs reasonably well for these AEAs.) Errors in AEAs for these functionals, using a data set on which the functionals have not been trained, do not appear to have been reported in the literature.

Let us now turn our attention back to weakly-bound anions. The average error in B3LYP/6-31(1+,3+)G* VDEs for $(H_2O)_N^-$ isomers was quoted as 0.24 eV in Ref. 202 on the basis of CCSD(T) benchmarks for $N \leq 6$. In truth, this value is not much larger than the average B3LYP error of 0.16 eV that is reported in Table 8, although absolute errors of this magnitude constitute a

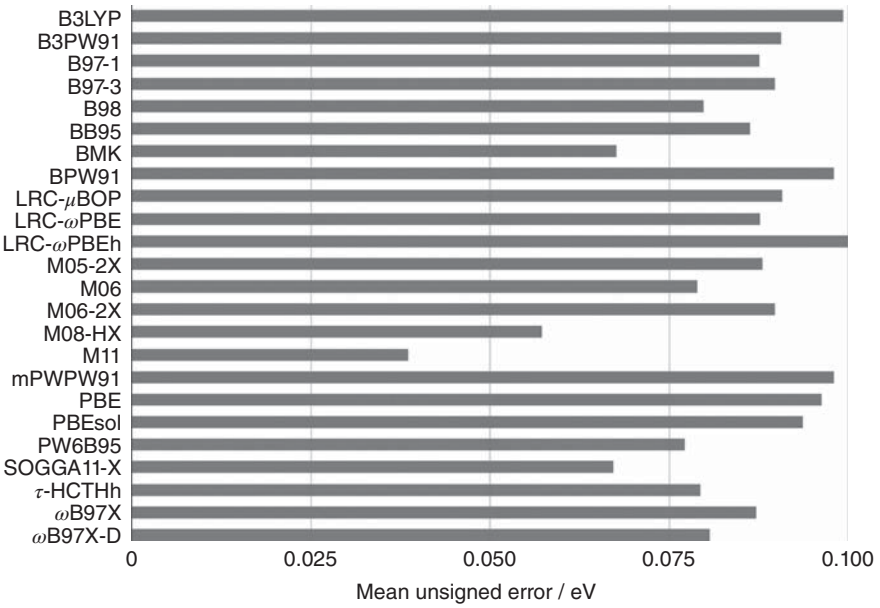

Figure 29 Mean unsigned errors for the database of 13 AEAs given in Table 1, with zero-point corrections removed from the experimental data,[97] and considering only functionals that perform at least as well as B3LYP. Note that the Minnesota (M) functionals and SOGGA11-X were parameterized based in part on this same set of AEAs. The basis set is G3(MP2)large,[244] but with diffuse functions removed from the hydrogen atoms, a basis that Truhlar and coworkers call MG3S. Data for the three long-range corrected (LRC) functionals are reported here for the first time; the parameters in these functionals are taken from Ref. 323 (LRC-ωPBE), Ref. 324 (LRC-ωPBEh), and Ref. 202 (LRC-μBOP). The remaining data are taken from Refs. 319–322.

much larger *fraction* of the VDE for a very weakly-bound anion, where even a 0.1–0.2 eV error might constitute 50–100% of the actual VDE. Moreover, the basis sets used to compile the error statistics in both Table 8 and Figure 29 are all singly-augmented, and thus inadequate for weakly-bound anions. Looking at the most diffuse exponent on the carbon and hydrogen nuclei in these basis sets and using Eq. [28] to convert the exponent into a minimum VDE suggests that these basis sets are appropriate only for VDEs $\gg$ 0.4–0.5 eV. For the more electronegative oxygen atom (which has a correspondingly smaller diffuse exponent), the same estimate suggests that these singly augmented basis sets are appropriate when the VDE is > 0.9 eV.

This is especially troubling in view of the fact that SIE, which leads to *overestimates* of VDEs for doublet radical anions in the complete-basis limit (because the SIE preferentially stabilizes the anion, with its half-filled orbital), can be substantially cancelled by the incompleteness of the basis set. (Diffuse functions preferentially stabilize the anion, so their omission *destabilizes* the anion.) The weakly-bound $(H_2O)_{12}^-$ isomer in Figure 18(a) is a good example. In

an overly compact basis set such as 6-31++G*, which is $n = 1$ in Figure 18(a), the B3LYP functional predicts VDE ≈ 0, which is in fact the right answer, based on MP2 calculations with very diffuse basis sets. However, the B3LYP VDE increases steadily as the quality (diffuseness) of the basis set is improved, such that when a more appropriate basis like 6-31(1+,3+)G* is used, the B3LYP prediction is a VDE of 0.2 eV. As such, it is possible (though certainly not advisable!) to use benchmark calculations or experimental data to "tune" the diffuseness of the basis set such that a given functional may afford an accurate VDE. However, there is no way to tell whether that particular combination of functional and basis set has any robustness or generality, and there is every reason to suspect that it does not.

Another hallmark of self-interaction problems, and another opportunity for ill-advised tweaking of DFT parameters, is the fact that DFT errors in VDEs are tunable, over a fairly wide range, as a function of the fraction of Hartree–Fock exchange that is included in the functional.[191] Of the commonly used functionals (as of 2005), BH&HLYP was the only choice found to yield useful results,[191] which is why this functional was selected for tests of the MBPT2(KS) approach that was discussed previously. VDEs predicted using BH&HLYP were typically ~0.03 eV larger than CCSD(T) predictions,[191] and this is borne out in the benchmark VDE comparison for $(H_2O)_N^-$ clusters that is shown in Figure 30(a). This comparison suggests a tractable way of putting error bars on computed VDEs, namely, by comparing the MP2 and BH&HLYP values,[191,270] although this approach would need to be tested against other methods on a wider variety of systems before it could convincingly be deployed to study weakly-bound anions other than the water and hydrogen fluoride cluster anions studied in Refs. 191 and 271.

Self-Interaction Corrections

Rather than tuning the combination of functional and basis set, and benchmarking against wave function methods for similar systems, another strategy is to try to eliminate the SIE that is a major source of error in VDE calculations. A simple self-interaction correction (SIC) was proposed in 1981 by Perdew and Zunger (PZ),[328] in which the self-interaction is subtracted orbital-by-orbital from the KS energy:

$$E_{\mathrm{PZ}}[\{\rho_{i\sigma}\}] = E_{\mathrm{KS}}[\rho_\alpha, \rho_\beta] - E_{\mathrm{SIC}}[\{\rho_{i\sigma}\}] \qquad [44]$$

Here, $\rho_{i\sigma} = |\phi_{i\sigma}|^2$ is the density associated with an occupied MO, and $\sigma = \alpha$ or β is a spin index (thus $\rho_\sigma = \sum_i \rho_{i\sigma}$). The SIC is

$$E_{\mathrm{SIC}}[\{\rho_{i\sigma}\}] = \sum_{\sigma=\alpha,\beta} \sum_{i}^{\mathrm{occ}} (E_{\mathrm{xc}}[\rho_{i\sigma}, 0] + J[\rho_{i\sigma}]) \qquad [45]$$

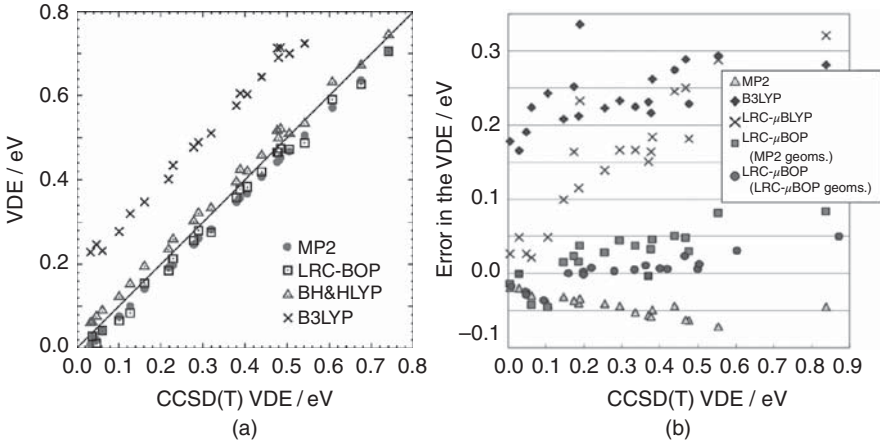

Figure 30 Comparison of VDEs for $(H_2O)_N^-$, $N = 2-7$, versus benchmark CCSD(T) results. In (a), cluster geometries were optimized at the B3LYP/6-31(1+,3+)G* level. MP2 and CCSD(T) calculations employ the 6-31(1+,3+)G* basis set while DFT calculations use the aDZ+diff basis from Ref. 202 which contains one more diffuse shell as compared to aug-cc-pVDZ, generated using a scaling factor $\kappa = 1/8$. In (b), all calculations use the aDZ+diff basis and MP2 geometries are used, except where indicated for the LRC-μBOP calculations. Panel (a) is adapted with permission from Ref. 15; copyright 2009 Taylor and Francis. Panel (b) is adapted with permission from Ref. 202; copyright 2008 American Chemical Society.

Using the notation of Hartree–Fock theory,[35]

$$J[\rho] = \int d\mathbf{r}\ v_{\mathrm{H}}(\mathbf{r})\,\rho(\mathbf{r}) \qquad [46]$$

is the so-called Hartree (or Coulomb) functional. The Perdew–Zunger SIC in Eq. [45] failed to find widespread use, however, because it spoils the invariance of the energy with respect to unitary transformations of the occupied MOs and is thus difficult to implement self-consistently within the standard KS formalism. Systematic tests of this SIC were not reported until 2004,[329] and it was then determined that this SIC does *not* improve the accuracy of DFT thermochemistry, except in the case of the LDA functional. (Enthalpies of formation were the only properties examined in Ref. 329.)

As a simpler alternative for doublet radical anions, one might try to eliminate the SIE from the SOMO only, since that is likely the main source of error in the VDE. Jungwirth and coworkers[330,331,218,217] have reported *ab initio* molecular dynamics simulations on $(H_2O)_{32}^-$, using the BLYP and PBE functionals plus an *ad hoc* SIC of this form, which had been proposed previously.[332,333] This SIC is based on the reasoning that, if the exact E_{xc} were known, then it would cancel the self-interaction in $J[\rho]$ exactly. In view of this consideration,

a sensible SIC for doublet radicals is[332]

$$\Delta E_{\mathrm{SIC}}[\rho_\alpha, \rho_\beta] = -J[m(\mathbf{r})] - E_{\mathrm{xc}}[m(\mathbf{r}), 0] \qquad [47]$$

where $m(\mathbf{r}) = \rho_\alpha(\mathbf{r}) - \rho_\beta(\mathbf{r})$ is the spin density. For self-consistency, one should implement ΔE_{SIC} by taking its functional derivatives with respect to density, and adding this as a correction to $v_{\mathrm{KS}}(\mathbf{r})$,[332] although this is not always done in practice. Equation [47] can be viewed as an *ad hoc* modification of the original Perdew–Zunger procedure and is appropriate only for systems with a single unpaired electron. Unlike the more general Perdew–Zunger scheme, however, the correction in Eq. [47] is inexpensive to evaluate and does not spoil orbital invariance among the doubly occupied MOs. Unfortunately, this simplified SIC *does* lead to unphysical distortions of these MOs, such that $\phi_{i\alpha}$ becomes very different from $\phi_{i\beta}$. To prevent this, the slightly more complicated[333] restricted open shell Kohn–Sham formalism[334–336] is required,[332] in which $\phi_{i\alpha} = \phi_{i\beta}$ (by construction) for each doubly-occupied MO.

In the context of simulating the aqueous hydroxyl radical using plane-wave DFT, VandeVondele and Sprik suggested a modified form of Eq. [47] that introduces two adjustable parameters, a and b:

$$\Delta E_{\mathrm{SIC}}[\rho_\alpha, \rho_\beta] = -aJ[m(\mathbf{r})] - bE_{\mathrm{xc}}[m(\mathbf{r}), 0] \qquad [48]$$

These authors then took $b = 0$ by fiat, citing studies of hemibonded cation radical systems in which the SIE, which arises primarily from an overly delocalized cation hole, was found to be roughly proportional to $J[m(\mathbf{r})]$.[337,338] The value $a = 0.2$ was then chosen by comparison to CCSD(T) calculations for some cation dimer radicals. Whether this rationale extends to anions is unclear, and in fact very different parameters ($a = 0.8$ and $b = 0.5$) have been suggested on the basis of studies of other, non-hemibonded cation radicals.[339] Nevertheless, the parameters $a = 0.2$ and $b = 0$ were adopted in the aforementioned $(H_2O)_{32}^-$ calculations,[217] whereas in *ab initio* molecular dynamics simulations of e^-(aq) in bulk water, the value $a = 0.3$ (with b again fixed at zero) was found to provide better agreement with the experimental absorption spectrum.[145] In Ref. 330, isosurface plots of $m(\mathbf{r})$ are presented for one particular isomer of $(H_2O)_{32}^-$, and the result obtained at the SIC-PBE level is seen to be qualitatively similar to the MP2 result. However, the SIC-PBE and RI-MP2 VDEs are rather different, and these differences do not appear to be systematic.[330] (On the other hand, the RI-MP2/6-311G* benchmarks in Ref. 330 could certainly be improved, in terms of the diffuseness of the basis set.) Moreover, the SIC is found to have *qualitative* effects on reactivity; the aqueous-phase reaction $H^+ + e^- \rightarrow H$, simulated inside of a water cluster, proceeds readily with the SIC but not without it.[340] In view of these issues, it seems that careful, systematic benchmark studies of SIC functionals for weakly-bound anions are probably warranted.

An alternative to explicit SICs is the use of long-range corrected (LRC) functionals,[341–344] also known as range-separated hybrid functionals,[345] which have garnered significant interest over the past decade. The LRC idea, as put forward by Hirao and coworkers[341] on the basis of earlier ideas by Savin and coworkers,[346,347] is to partition the electron–electron Coulomb operator, r_{12}^{-1}, into short- and long-range components, which are then described using different theoretical models. The most common partition uses the error function, erf(x):

$$\frac{1}{r_{12}} = \underbrace{\frac{1-\mathrm{erf}(-\mu r_{12})}{r_{12}}}_{SR} + \underbrace{\frac{\mathrm{erf}(-\mu r_{12})}{r_{12}}}_{LR} \qquad [49]$$

The first term on the right is the short-range component, and decays to zero on a length scale $\sim \mu^{-1}$, where μ is taken as an adjustable *range separation parameter*. Consider an exchange-correlation functional of the form $E_{xc} = E_x + E_c$, and furthermore separate the exchange functional into a nonlocal Hartree–Fock component and a local GGA component:

$$E_{xc} = E_c + C_{\mathrm{HF}} E_x^{\mathrm{HF}} + (1 - C_{\mathrm{HF}}) E_x^{\mathrm{GGA}} \qquad [50]$$

Here, C_{HF} represents the coefficient of Hartree–Fock exchange. For example, $C_{\mathrm{HF}} = 0.2$ for B3LYP, $C_{\mathrm{HF}} = 0.5$ for BH&HLYP, and $C_{\mathrm{HF}} = 0$ for BLYP. Then the corresponding LRC functional is

$$E_{xc}^{\mathrm{LRC}} = E_c + C_{\mathrm{HF}} E_x^{\mathrm{HF,SR}} + (1 - C_{\mathrm{HF}}) E_x^{\mathrm{GGA,SR}} + E_x^{\mathrm{HF,LR}} \qquad [51]$$

The labels "SR" and "LR" indicate whether each component is evaluated using the short-range or the long-range component of r_{12}^{-1}, as defined in Eq. [49].

The terms $E_x^{\mathrm{HF,SR}}$ and $E_x^{\mathrm{HF,LR}}$ in Eq. [51] can be handled using modified electron repulsion integrals,[348] but $E_x^{\mathrm{GGA,SR}}$ requires fundamental modifications to the GGA exchange functional. Two different ways to perform these modifications have been suggested: one on the basis of a modification to the GGA exchange enhancement factor,[341] and another on the basis of a modified exchange hole.[349] The papers developing the former *ansatz* have mostly been written by Hirao and coworkers,[341,342,350,351,343] who consistently use the symbol μ to represent the range separation parameter, as in Eq. [49], whereas Scuseria and coworkers[33,352,353,349,345] consistently use the symbol ω instead. As such, a notation for LRC functionals is the following:[354] LRC-μGGA is the LRC version of a particular GGA functional (e.g., GGA = PBE or BLYP) that is constructed according to the modified exchange enhancement factor introduced by Hirao's group.[341] LRC-ωPBE, on the other hand, denotes the LRC functional that uses the short-range ωPBE functional from the modified exchange hole introduced by Scuseria and coworkers.[349] (Whereas Hirao's construction can be applied to both the PBE and Becke88 exchange functionals, affording

short-range exchange functionals that we denote as μPBE and μB88, respectively, the exchange-hole formalism has been applied only to PBE, affording the ωPBE short-range exchange functional.) This notation, introduced in Ref. 354, is consistent with how these functionals are designated in the Q-Chem electronic structure program.[194,195] Note, however, that the LRC-ωPBE functional has also been called LC-ωPBE,[349] and the functional discussed below that is called LRC-μBOP in Q-Chem has also been called LC-BOP.[202] One must also take care that different electronic structure programs may have different default values for the μ or ω parameter, and computed properties can be very sensitive, in some cases, to the precise value that is used.[355,356,324]

For well-separated electrons, the exchange-correlation functional in Eq. [51] consists of 100% Hartree–Fock exchange, since E_c is local. Hartree–Fock theory is free of self-interaction, at least in the sense that this term has historically been defined, namely, $E_{xc} = 0$ for a one-electron system. (More recently, this traditional definition has been called the "one-electron" SIE.[357,311]) As such, one might expect LRC functionals to mitigate some of the problems associated with the DFT description of VDEs, especially in cases where the SOMO is largely separated from the valence MOs, and this is indeed the case with *certain* LRC functionals.[202,358] This is demonstrated in Figure 30, where VDEs for a variety of $(H_2O)_N^-$ clusters are computed using LRC-μBOP and LRC-μBLYP and compared to CCSD(T) benchmarks. The LRC-μBOP functional with $\mu = 0.33$ bohr^{-1} is found to perform just as well as MP2 theory and slightly better than MP2 if the geometries are optimized at the same level of theory that is used to compute the VDEs. In the latter case, the mean absolute deviations relative to CCSD(T) are 0.014 eV for LRC-μBOP versus 0.044 eV for MP2.[202]

On the other hand, LRC-μBLYP results are only moderately better than B3LYP results; see Figure 30(b). Both LRC-μBLYP and LRC-μBOP use a short-range version of Becke88 exchange[274] (μB88) for the $E_x^{\mathrm{GGA,SR}}$ term in Eq. [51], and the same value of the range separation parameter, μ. Thus, the only difference between the two is the correlation functional: the well-known LYP functional[273] in one case, versus the "one-parameter progressive" (OP) functional[359] in the other. Yagi et al.[202] suggest that the superior performance of LRC-μBOP originates in the fact that the OP correlation functional satisfies the exact constraint that the correlation energy density should vanish in the limit of a rapidly varying density,[359] whereas the LYP functional violates this constraint.

As mentioned above, predicted properties can be sensitive, in some cases, to the value of the range separation parameter.[356,355,324] In this context, it is worth noting that the original suggestion to use $\mu = 0.33\ a_0^{-1}$ comes not from fitting anion VDEs but rather was optimized to reproduce bond lengths for second-row diatomic molecules.[342] In other LRC functionals, the μ (or ω) parameter has been optimized to reproduce various experimental data.[353,343,349,324,323] A less empirical approach has been advocated[344] and

may have particular appeal for the calculation of anion VDEs and excitation spectra, but to understand this approach we must first digress to discuss a particular theorem in exact DFT, on which the method is based.

It is known that if the exact functional $E[\rho]$ were employed in a KS DFT calculation, then the value $-\varepsilon_{\mathrm{HOMO}}$ obtained from that calculation would be *exactly* equal to the system's smallest IP.[197,360,361] This result is in sharp contrast to the Hartree–Fock case, where $-\varepsilon_{\mathrm{HOMO}}$ is the KT *approximation* to the IP. On the other hand, for typical approximate density functionals, the value of $-\varepsilon_{\mathrm{HOMO}}$ is often a very crude approximation to the actual IP, much worse than the KT approximation obtained from a Hartree–Fock calculation. For example, a recent study[362] compared IPs for atoms and small molecules computed at the CCSD(T)/aQZ level to $-\varepsilon_{\mathrm{HOMO}}$/aQZ values for several functionals and found mean differences of 1.5 eV for M05-2X, 3.5 eV for B3LYP, and 5.3 eV for BOP, as compared to 0.8 eV for Hartree–Fock theory. As such, the recommended way to compute an IP using DFT is *not* to use $-\varepsilon_{\mathrm{HOMO}}$, but rather to use a ΔSCF approach. LRC functionals, however, do a much better job of achieving $-\varepsilon_{\mathrm{HOMO}} \approx$ IP, with a mean error of only 0.2 eV for LRC-μBOP (with $\mu = 0.47\ a_0^{-1}$) as compared to benchmark CCSD(T)/aQZ results.[362]

Motivated by the aforementioned theorem (IP $= -\varepsilon_{\mathrm{HOMO}}$), Baer et al.[344] have suggested tuning μ (or ω) in a system-specific way to satisfy this condition. Taking the IP to be defined by a ΔSCF calculation then provides some degree of self-consistency to this optimization procedure and provides an asymptotically correct exchange-correlation potential for the system of interest. Although Baer and coworkers have mostly been interested in ionization of neutral molecules,[363,344] in keeping with the spirit of this chapter we will state this condition in terms of the IP (= VDE) of the anion M^-:

$$E_{\mathrm{M}}(\mu) - E_{\mathrm{M}^-}(\mu) = -\varepsilon_{\mathrm{HOMO,M}^-}(\mu) \qquad [52]$$

The left-hand side of this equation is simply the ΔSCF value of the VDE for M^-, evaluated at a particular value of μ. The "tuning" procedure of Baer et al.[344] consists in locating a (system-specific) value of μ that satisfies Eq. [52]. While there is no theoretical guarantee that such a value must exist, some commonly used LRC functionals approximately satisfy this condition already, with values of μ that were obtained by minimizing the statistical errors with respect to some set of experimental data. This suggests that exceptional cases,[364] where no value of μ that satisfies Eq. [52] can be found, may be just that: exceptions.

Figure 31 shows an example of this tuning procedure for one particular isomer of $(H_2O)_6^-$.[162] This system was chosen because its VDE has been reported on the basis of a large-basis CCSD(T) calculation and a QMC calculation, and the two benchmark VDEs agree to within the statistical error of the QMC result.[259] For this system, the condition in Eq. [52] is satisfied when $\mu = 0.25\ a_0^{-1}$, and at this value of μ the error in the VDE (with respect to the benchmark) is 0.08 eV. In contrast, a ΔSCF calculation of the VDE agrees with

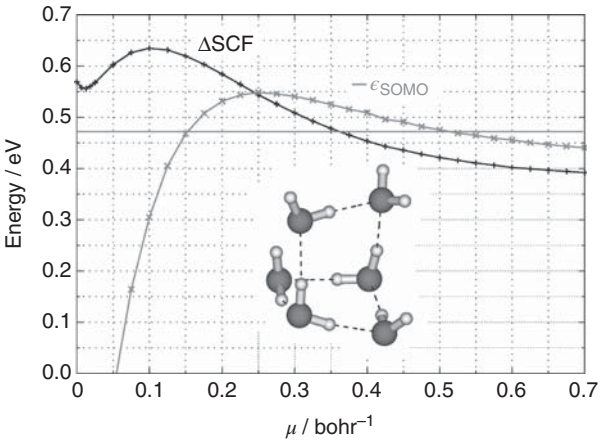

Figure 31 VDE for the "OP1-AA" isomer[128] of $(H_2O)_6^-$, computed at the LRC-μBOP/aDZ+diff level, as a function of the range separation parameter, μ. Results from a traditional ΔSCF calculation of the VDE are plotted along with the value $-\epsilon_{SOMO}$. The solid horizontal line represents the CCSD(T) VDE from Ref. 259, which is in good agreement with quantum Monte Carlo results. Reprinted with permission from Ref. 162; copyright 2011 American Chemical Society.

the benchmark for $\mu = 0.35\ a_0^{-1}$. At this larger value of μ, the condition in Eq. [52] is violated only by about 0.05 eV, which suggests that LRC-μBOP with $0.25\ a_0^{-1} \lesssim \mu \lesssim 0.35\ a_0^{-1}$ is a good method for this system. Note, however, that the tuned value of μ often varies strongly with system size, such that a rather different value may be optimal for larger $(H_2O)_N^-$ clusters.[163]

These considerations lend some credence to the use of LRC functionals for moderate accuracy ($\sim$0.1 eV) VDE calculations in weakly-bound anions, which is especially promising for studies of cluster anions and other condensed-phase species, where large system sizes are required to obtain a realistic model. It has also been found that LRC functionals avoid the spurious transfer of fractional electrons from negatively to positively charged moieties on molecules that contain both.[317,365] At the same time, even for LRC functionals one is not free of the dependence of the result on the choice of functional, hence benchmarking against wave function methods remains advisable. The "tuning" criterion for μ in Eq. [52] suggests how this parameter can be validated, or perhaps modified, if some other LRC density-functional were to be used in place of LRC-μBOP.

QUANTUM CHEMISTRY FOR METASTABLE ANIONS

The traditional quantum chemistry methods discussed up to this point are designed to find the lowest Born–Oppenheimer energy and wave function (or density) for a given arrangement of the nuclei. For the AB^- system described

in Figure 1, the lowest-energy state for $R > R_c$ does indeed correspond to an anion: either the molecular anion AB^- (around the minimum-energy geometry), or else the radical $A^\bullet$ plus the anion B^- (in the exit channel as $R \rightarrow \infty$). For $R < R_c$, however, the lowest-energy form of AB^- corresponds (in the basis-set limit) to a neutral AB molecule and a free electron. As such, bound-state quantum chemistry methods are not appropriate for $R < R_c$. In that regime, bound-state quantum chemistry applied to AB^- will afford an *orthogonalized discretized continuum* (ODC) solution,[366,233,367–369] consisting of ψ_{AB} for the neutral molecule superimposed on a poor quality, finite-basis approximation of a free electron. In such a case, the VDE should converge to zero in the limit of an infinitely-diffuse basis set.

Stated differently, while it is possible to use standard quantum chemistry methods to compute *an* energy for the unbound ($R < R_c$) state of AB^-, in general the computed wave function will not match the correct boundary conditions to qualify as a proper resonance state. In terms of the one-dimensional example in Figure 13, not every particle that is incident from the left yields a resonant enhancement of the probability density inside of the potential well. Only for a narrow range of incident particle energies is the phase matching "just right" to afford a resonance. As Simons puts it,[2] "An arbitrarily chosen basis, even with diffuse functions included, will yield but an arbitrary energy for the metastable anion rather than the correct resonance." This has not prevented the appearance of numerous studies of purportedly stable molecular anions in which what was really being examined is the structure of a neutral molecule in the field of a $-e$ charge that is smeared out over the most diffuse functions that are included in the basis set.

An example is depicted in Figure 32, which shows the results of two different calculations aimed at understanding whether electrons with near-zero kinetic energy can initiate DEA reactions within the DNA backbone.[370–372] The hypothesis was put forward that e^- attachment to P–O π^* orbitals of a phosphate moiety could subsequently lead to a rupture of a sugar–phosphate C—O bond.[371] Using a charge stabilization method that is discussed later (as an appropriate technique for computing potential curves for metastable anions), Simons and coworkers[370] obtained the C—O potential energy scans shown in Figure 32(a). These potentials do suggest the existence of a $(\pi^*_{CO})^-$ anion resonance and also a dissociative $(\sigma^*_{CO})^-$ resonance. Electron attachment to form the $(\pi^*_{CO})^-$ state is therefore capable of causing C—O bond dissociation, according to the calculation. However, the calculations also suggest that the $(\pi^*_{CO})^-$ resonance lies > 2.5 eV above the energy of the neutral species in its equilibrium geometry. Bond rupture by ~0 eV electrons is therefore excluded, according to this calculation.[370,372]

A wholly different picture emerges when traditional bound-state quantum chemistry methods are applied, as shown in Figure 32(b).[371] A B3LYP/6-31+G* calculation of the C—O moiety affords "anion" potential energy curves that

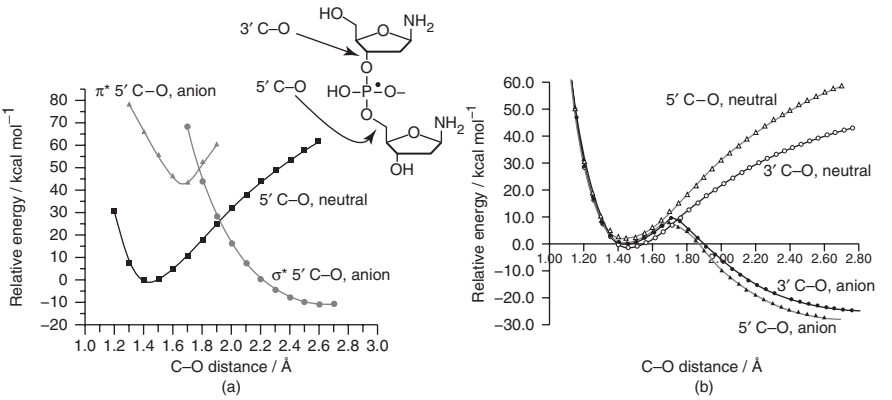

Figure 32 One-dimensional potential energy scans for a section of DNA backbone, addressing the question of whether attachment of zero-energy electrons to P–O π^* orbitals can subsequently cause rupture of a sugar—phosphate C—O bond. (a) Potential energy curves for the neutral 5′ C—O bond and two-electron-attached states thereof, the latter obtained using stabilization methods that can correctly describe metastable anion resonances. Qualitatively similar curves are obtained for the 3′ C—O bond but are not shown, for clarity. An electron whose energy matches the neutral-to-$(\pi^*)^-$ energy gap could potentially attach to form a temporary negative ion, which might subsequently undergo internal conversion to the $(\sigma^*)^-$ state, resulting in C—O bond dissociation. (b) Potential energy curves along both the 3′ and the 5′ C—O bond, obtained from a conventional B3LYP/6-31+G* calculation of the sugar—phosphate—sugar moiety and its anion. In both panels, the equilibrium value of the neutral C—O bond is used to define the zero of energy. Panel (a) is reprinted with permission from Ref. 370; copyright 2004 American Chemical Society. Panel (b) and the chemical structure drawing are reprinted with permission from Ref. 371; copyright 2003 American Chemical Society.

are essentially isoenergetic with the neutral curves, in the vicinity of the equilibrium geometry that both the neutral and anionic species reportedly share. After passing over a small barrier, the anion's potential energy curves become dissociative at larger C—O bond lengths, which was taken as evidence in favor of the hypothesis that very low-energy electrons could induce single-strand breaks.[371] However, the isoenergetic minima and similarly-shaped potential curves are also features that one would expect for a neutral molecule that is subject to the weak field arising from a smeared-out one-electron density trapped a few Angstroms away by a set of diffuse (but atom-centered) Gaussian functions. Larger bond lengths lead to a larger C—O bond dipole, such that the extra electron is probably stabilized into a σ^*_{CO} orbital as the bond is stretched. In a sense, this calculation captures the correct physics at large C–O bond lengths, yet the description of the anion states in the vicinity of the neutral molecule's equilibrium geometry is almost certainly wrong.[370]

The remainder of this section is devoted to methods that can get such systems *right*. As mentioned in the introductory remarks to this chapter, the discussion here is limited to methods that are based on relatively

straightforward modifications to traditional (bound-state) quantum chemistry methods, since these are the only theoretical approaches that are widely accessible to the chemistry community. Such methods have also been reviewed in Ref. 20.

Maximum Overlap Method

Let us consider a slightly different case first, namely, the protonated model peptide system that was discussed in the context of electron transfer dissociation spectroscopy (see Figure 2). The goal of the calculations reported in Figure 2 is to obtain electron-attached Rydberg states, two of which are shown in the figure, and then to determine whether internal conversion to a dissociative $(\sigma^*)^-$ state is feasible.[77,74] At the equilibrium geometry of the parent species (the peptide cation), the lowest of the electron-attached Rydberg states is also the lowest Born–Oppenheimer electronic energy for a system composed of the parent molecule and an extra electron. As such, this state can be determined using traditional quantum chemistry, but the higher-lying Rydberg-attached state cannot be, nor can the $(\sigma^*)^-$ state.

Instead, the higher lying states were found using the following procedure.

1. First, compute MOs for the parent molecule (which happens to be a cation, in the calculations of Refs. 74 and 77 but might be a neutral molecule in other applications).
2. Second, compute the electron-attached Hartree–Fock determinant for the state of interest, using the neutral molecule's MOs as an initial guess but altering the initial occupancies such that an electron is added not to the LUMO but to some higher-lying virtual MO.

Following this procedure, the SCF calculation *may* converge (in the sense of finding a stationary point in the space of MO coefficients) to a legitimate solution of the SCF equations, but one that is *not* the lowest-energy solution. If so, then this state represents a Hartree–Fock approximation to an excited state (a higher-lying Rydberg-attached state, or the $(\sigma^*)^-$ state in the present example) including full orbital relaxation upon electron attachment. Electron correlation can be included subsequently, simply by using this excited Hartree–Fock determinant as the reference state for a correlated wave function. (The curves in Figure 2 were computed in this way at the MP2 level.[74])

On the other hand, this procedure is by no means guaranteed to work. In many cases, the "non-*aufbau*" guess for the initial MO occupancies may suffer variational collapse as the SCF iterations proceed, such that despite the elaborate initial guess, the final, converged SCF solution is simply the lowest energy anion state. In the calculations reported in Figure 2,[74] it proved possible to locate the excited Rydberg-attached state in this way, but attempts to determine the σ^*-attached state suffered variational collapse, and the potential

curve for that state was ultimately computed in an entirely different way, using stabilization methods that are described later in this chapter.

To avoid variational collapse, it is probably advisable to use an SCF convergence algorithm that is based on direct minimization[373] rather than extrapolation methods such as direct inversion in the iterative subspace (DIIS)[374] and related methods,[375] which are the default convergence algorithms in most quantum chemistry programs. Direct minimization, while often very slow to reach convergence, is more likely to converge to the desired *local* minimum in the space of MO coefficients.

Nevertheless, even direct minimization remains vulnerable to variational collapse, since the newly-occupied MO of the anion is subject to a different potential as compared to virtual MOs that might be nearby in energy. Subsequent SCF iterations can therefore modify the energetic ordering of the MOs, and in such cases, it is unclear which MOs should be the occupied ones at the next SCF iteration. The *maximum overlap method* (MOM)[376,377] offers a possible solution to this problem, and a more refined version of the orbital relaxation technique.

Originally implemented in Q-Chem[194,195] as a way to assist SCF convergence in cases of near degeneracies, MOM has more recently been used as a means to compute electronically excited states using ground-state SCF technology,[376,377] and extension to electron-attached states is straightforward. The basic idea is that once the initial MO occupancies have been specified (with one or more holes below the Fermi level), the Fock matrix is constructed and diagonalized to obtain new MOs, but then the occupancies of these MOs are chosen, not according to the *aufbau* principle but rather by determining which orbitals exhibit maximum overlap with the orbitals from the previous SCF iteration.[376] Although not immune to variational collapse (especially, in our experience, when large, diffuse basis sets are employed, which may be a problem), this method has been applied successfully to the challenging problem of computing core-level excitation spectra.[377] In other words, SCF solutions that correspond to the promotion of an electron from a core orbital into a low-lying virtual orbital have been converged successfully, without collapse of the core hole. In the future, MOM may provide a more robust way to perform orbital relaxation for electron-attached states, although the algorithm has not yet been tested extensively in this capacity.

Note that the states that are generated by MOM are *diabatic* states, in the sense that the character of the wave function changes smoothly as each state passes through the interaction region with another state (see Figure 2). In a one-dimensional, two-state diabatic model, we can write the Hamiltonian in the form

$$\mathbf{H} = \begin{pmatrix} E_1(R) & V(R) \\ V(R) & E_2(R) \end{pmatrix} \qquad [53]$$

Here, $E_1(R)$ and $E_2(R)$ are the diabatic potential energy curves obtained, for example, using the MOM procedure. The adiabatic (Born–Oppenheimer) potential energy curves are the eigenvalues of this matrix:

$$E_{\pm} = \frac{1}{2}(E_1 + E_2) \pm \frac{1}{2}\sqrt{(E_1 - E_2) + 4V^2} \qquad [54]$$

The quantities E_1, E_2, and V each depend on molecular geometry, R, but this is suppressed in Eq. [54], for brevity. At the point $R_\times$ where the two diabatic curves cross ($E_1 = E_2$), the adiabatic states are split by $\Delta E = E_+(R_\times) - E_-(R_\times) = 2V(R_\times)$. Having obtained the point $R_\times$ from plotting the diabatic potential curves, if one can compute *adiabatic* energies at $R_\times$ for the two states in question, then one can evaluate the coupling, $V(R_\times)$. (In fact, this procedure could be followed at any value of R, using Eq. [54] to map out the coupling $V(R)$, but we assume for simplicity that this coupling changes little in the vicinity of the crossing point.) Calculating the Born–Oppenheimer adiabatic energies $E_\pm(R)$ requires performing some type of electronic structure calculation that is capable of computing excited states, and this procedure has been used by Simons and coworkers[74–78] to evaluate $V(R_\times)$ for systems such as the protonated peptide electron capture problem that is depicted in Figure 2.

With the coupling matrix element $V = \langle \psi_1^{\text{diabatic}} | \hat{H} | \psi_2^{\text{diabatic}} \rangle$ in hand, the semiclassical Landau–Zener formula[378,379] can be used to estimate the rate of nonadiabatic transitions. According to Landau–Zener theory, the probability (call it p_{LZ}) of making a transition from state 1 to state 2 is

$$p_{\text{LZ}} = 1 - \exp\left(-\frac{2\pi V^2}{\hbar \dot{R} |\Delta F|}\right) \qquad [55]$$

where $\dot{R}$ is the speed at which the nuclei are passing through the interaction region and ΔF is the difference in the forces (slopes) on the two diabatic potential energy curves. (Both of these ideas are semiclassical in that they take a classical view of the nuclear motion.)

To use Eq. [55], one must estimate the nuclear speed $\dot{R}$ along the reaction coordinate in question. A harmonic approximation for the reaction coordinate (e.g., the S–S stretching coordinate for the example in Figure 2) affords a simple means to do this,[74] and one that is consistent with the semiclassical nature of Landau–Zener theory. Having computed the (linear) harmonic frequency ν for the mode in question, using some flavor of quantum chemistry, one may compute the classical turning points of the harmonic potential:

$$x_{\pm} = \pm\sqrt{\frac{\left(n + \frac{1}{2}\right)h}{4\pi^2 m\nu}} \qquad [56]$$

where m is the reduced mass for the mode in question, and $n = 0, 1, \ldots$ is the vibrational quantum number. Taking twice the distance between the two turning points as a measure of the distance traversed during a single vibrational period, one obtains the estimate $\dot{R} \approx 4x_+\nu$ (speed = distance × frequency), which works out to be

$$\dot{R} \approx \frac{2}{\pi}\left[\frac{\left(n+\frac{1}{2}\right)h\nu}{m}\right]^{1/2} \qquad [57]$$

Finally, one may estimate the nonadiabatic transition rate according to[74]

$$\text{rate} = (\text{frequency}) \times (\text{transition probability}) = \nu p_{\text{LZ}} \qquad [58]$$

Simons and coworkers[74–78] have used this procedure to estimate electron capture and DEA rates for problems such as the one in Figure 2.

Landau–Zener theory is applicable in the regime where the nuclear kinetic energy is large compared to the spacing between the adiabatic potential energy surfaces in the crossing region.[380] The latter may be estimated as $\Delta E \approx 2V$ (from Eq. [54] with $E_1 = E_2$), whereas the nuclear kinetic energy is $m\dot{R}^2/2$. These considerations suggest that Landau–Zener theory is appropriate in the limit

$$|V| \ll \frac{\left(n+\frac{1}{2}\right)h\nu}{\pi^2} \qquad [59]$$

Assuming a typical disulfide harmonic frequency $h\nu \approx 515$ cm^{-1},[381] the couplings $V \approx 350$ cm^{-1} for the system considered in Figure 2 lie outside of this limit. However, they are at least small compared to $h\nu$, so that Landau–Zener theory can be used to estimate the nonadiabatic transition rate, even if the theory is not completely rigorous in this particular system.

Complex Coordinate Rotation

As compared to the MOM approach discussed earlier, other methods for treating metastable states are somewhat more involved, and understanding them requires a few concepts that go beyond bound-state quantum mechanics. One idea that is needed is the notion of analytic continuation of the bound-state energy levels into the complex plane. A heuristic explanation of why this is necessary goes as follows.[382] In some ways, a temporary anion resonance resembles a stationary state of the molecular potential, at least in the sense that the probability distribution is relatively localized around the molecule (see Figure 13). At the same time, however, the resonance has a finite lifetime and will ultimately tunnel out of the potential that is responsible for it. In view of these facts, it

seems reasonable that the simplest possible mathematical description of a resonance that is localized in space at time $t = 0$ might be the usual stationary-state time evolution formula,

$$\psi(\mathbf{r}, t) = e^{-iEt/\hbar} \ \psi(\mathbf{r}, 0) \qquad [60]$$

but with a complex energy

$$E = E_R - \frac{1}{2} i\Gamma \qquad [61]$$

(The quantities E_R and Γ are real.) Putting these two equations together, we have

$$\psi(\mathbf{r}, t) = e^{-t\Gamma/2\hbar} \ [e^{-iE_R t/\hbar} \ \psi(\mathbf{r}, 0)] \qquad [62]$$

The quantity in square brackets looks like an ordinary stationary state, suggesting that the real part of the energy (E_R) is the resonance energy. The imaginary part of the energy ($-\Gamma/2$) contributes an envelope function that decays exponentially on a timescale $\tau \sim \hbar/\Gamma$. This is consistent, up to factors of order unity, with the time-energy uncertainty principle in Eq. [19], if we take $\Delta E \sim \Gamma$. It is therefore not surprising that the quantity Γ is known as the *resonance width*. The lifetime of the metastable resonance is $\tau \sim \hbar/\Gamma$.

Scattering states are non-normalizable (and thus not in L^2, the Hilbert space of square-integrable functions), since they remain nonzero as $r \to \infty$. Moreover, one cannot obtain a complex energy as the eigenvalue of any self-adjoint operator. As such, the resonances cannot be computed directly using the machinery of bound-state quantum chemistry, but *can* be computed as eigenfunctions and eigenvalues of a modified, non-Hermitian Hamiltonian. The mathematical basis of this statement is a theorem by Balslev and Combes,[383] which we shall motivate below using a simple example and then summarize in a pedagogical way.

The underlying idea behind the *complex coordinate rotation* (CCR) method[382,384] that is suggested by the Balslev–Combes theorem is a complex scaling of the Cartesian coordinates in the Hamiltonian operator, each by the same complex phase factor: $x \to xe^{i\theta}$. This transformation defines a new, complex-scaled Hamiltonian, $\hat{H} \to \hat{H}(\theta)$. In one dimension (for simplicity), the complex-scaled Hamiltonian is

$$\hat{H}(\theta) = -\frac{\hbar^2 e^{-2i\theta}}{2m} \frac{\partial^2}{\partial x^2} + U(xe^{i\theta}) \qquad [63]$$

This idea is readily extended to the Born–Oppenheimer electronic Hamiltonian by noting that $x \to xe^{i\theta}$ implies that interparticle coordinates should be scaled as $r \to re^{i\theta}$. For $\theta \neq 0$, the operator $\hat{H}(\theta)$ is non-Hermitian and therefore admits complex eigenvalues. In its simplest form, the CCR method consists of determining these eigenvalues.

Before stating the general Balslev–Combes theorem, let us first consider two simple examples.[382] Up to constants and in atomic units ($\hbar = m_e = 1$), the 1s wave function for the hydrogen atom is $\psi(r) = e^{-r}$, which becomes $\psi(re^{i\theta}) = \exp(-re^{i\theta})$ upon complex scaling. The latter is still in L^2, provided that $|\theta| \leq \frac{1}{2}\pi$, else the function is not single-valued. (We will see that the CCR method uses only quadrant IV of the complex plane, corresponding to rotation angles $0 \geq \theta \geq -\frac{1}{2}\pi$.) To determine the energy of the state $\psi(re^{i\theta})$, we compute the expectation value

$$\langle E \rangle = \frac{\langle \psi(re^{i\theta}) | \hat{H}(\theta) | \psi(re^{i\theta}) \rangle}{\langle \psi(re^{i\theta}) | \psi(re^{i\theta}) \rangle} \quad . \qquad [64]$$

In more detail, this expectation value is

$$\langle E \rangle = \frac{\displaystyle\int_0^\infty e^{-re^{i\theta}} \left[\left(-\frac{e^{-2i\theta}}{2} \frac{1}{r^2} \frac{\partial}{\partial r} r^2 \frac{\partial}{\partial r} - \frac{1}{re^{i\theta}} \right) e^{-re^{i\theta}} \right] e^{3i\theta} r^2 dr}{\displaystyle\int_0^\infty (e^{-re^{i\theta}})^2 e^{3i\theta} r^2 dr} \qquad [65]$$

Two points warrant explanation here. First, $e^{3i\theta} r^2 dr$ is simply the radial volume element following complex scaling. Second, and more subtle, is the fact that the CCR factor of $e^{i\theta}$ does *not* get complex-conjugated, that is, $[\psi(re^{i\theta})]^* = \exp(-re^{i\theta})$. The reason is that this factor ultimately results from an integration contour in the complex plane, taking advantage of Cauchy's residue theorem; see Ref. 382 for a more detailed explanation of this point. The factor in square brackets in Eq. [65] represents the action of $\hat{H}(\theta)$ on $\psi(re^{i\theta})$ and can be evaluated directly; the result is $-\frac{1}{2}\psi(re^{i\theta})$. Evaluating the integrals in Eq. [65] then affords $\langle E \rangle = -\frac{1}{2}$ in atomic units, meaning that the energy of this bound-state solution is unchanged on complex scaling.

The scattering wave functions, on the other hand, will behave something like e^{ikr} at long range. On scaling $r \to re^{i\theta}$, these continuum functions will not remain finite as $r \to \infty$ unless $k \to ke^{-i\theta}$,[382] which also makes sense in terms of the inverse relationship between r (position) and $\hbar k$ (momentum). A continuum state is characterized by its kinetic energy, and therefore the energy $E = (\hbar k)^2/2m$ is transformed upon complex scaling into $E = e^{-2i\theta}(\hbar k)^2/2m$. It has been rotated into the complex plane by an angle of -2θ.

With these examples in hand, a pedagogical version of the Balslev–Combes theorem[383] can be stated as follows.[382]

1. Bound-state eigenvalues of the original Hamiltonian are equal to bound-state eigenvalues of $\hat{H}(\theta)$ and are independent of θ, provided that $|\theta| \leq \frac{1}{2}\pi$.
2. Segments of the continuum beginning at a given scattering threshold are rotated by -2θ into quadrant IV of the complex plane.

3. Resonance states appear as *discrete* (albeit complex) eigenvalues of $\hat{H}(\theta)$, having L^2 eigenfunctions. The quantities E_R and Γ are obtained from the real and imaginary parts of the complex energy, respectively, according to Eq. [61].
4. The discrete resonances are independent of θ so long as they are isolated from the continuum states, appearing or disappearing as the continuum states rotate past.

A pictorial illustration is provided in Figure 33. It is important to emphasize that the theorem is rigorously valid for *exact* eigenfunctions of $\hat{H}(\theta)$ in L^2. For approximate solutions, including finite-basis solutions, these results are not exact, and in particular the complex resonance energies acquire a θ-dependence in finite basis sets.[187] It is suggested in practice to compute $E(\theta)$ and to use the value where $|dE/d\theta|$ is minimized as a best estimate of the resonance energy.[385,187]

The CCR idea has been around for a long time, as reviewed in Refs. 389 and 391, and many applications to temporary anion resonances have been reported. Nevertheless, this technique has remained somewhat specialized. Within the context of electronic structure theory, what is required for a CCR calculation is to combine the complex-scaled Hamiltonian in Eq. [63] with the usual wave function *ansätze*, and this involves extending quantum chemistry codes to handle complex-valued wave functions and energies and non-Hermitian matrices. CCR implementations of the Hartree–Fock,[386,387] configuration interaction,[386] and multiconfigurational SCF (MCSCF) models[387] have been reported but are not available in standard

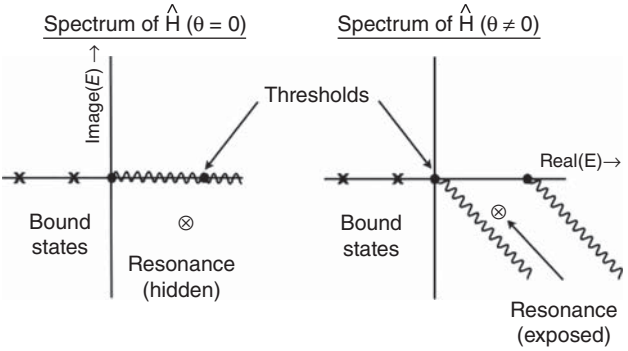

Figure 33 Pictorial illustration of the Balslev–Combes theorem and the complex coordinate rotation method. Horizontal and vertical axes represent the real and imaginary parts of the complex energy, respectively. Application of the complex-scaling transformation $x \rightarrow xe^{i\theta}$ rotates the continuum by an angle of -2θ in the complex plane, leaving the resonances "exposed" as discrete states with square-integrable wave functions and complex energies. Bound states remain on the real axis. Adapted with permission from Ref. 187; copyright 2013 American Institute of Physics.

quantum chemistry codes. In any case, the Hartree–Fock version of CCR is incapable of describing auto-ionizing Feshbach resonances, since these are two-electron processes (see the right side of Figure 16, for example). Hartree–Fock theory is obviously not suitable to describe such states, and a time-dependent DFT (TD-DFT) description of a true two-electron excitation requires the use of a frequency-dependent exchange-correlation kernel.[388] Such kernels so far exist only at the proof-of-concept level.[388,389]

Very recently, however, a CCR implementation of the EOM-CCSD method has been reported[187] in the Q-Chem program,[194,195] which promises to make such methods more routinely available to a wider variety of researchers. As it is based on a correlated wave function, this approach is capable of describing auto-ionizing, core-excited Feshbach resonances. So far, only atomic anion resonances have been considered, and the generation of molecular potential energy surfaces is complicated by the fact that the mathematical proof of the Balslev–Combes theorem requires the nuclear coordinates to be complex-scaled as well. Special techniques are therefore required to extract potential energy surfaces from CCR calculations.[390–394] Alternatively, the EOM-CCSD method has also been implemented in conjunction with a complex absorbing potential,[31,395] $\hat{H}_\xi = \hat{H} - i\xi W$, where the potential W turns on at large electron–molecule separation. Historically, the resonance energies thus obtained have been sensitive to the details of this potential, including most notably the coupling strength ξ, but recent progress has been made toward analyzing the ξ-dependent results in a way that minimizes this dependence.[31]

It is emphasized in Ref. 187 that very flexible basis sets are required to deal with the finite-basis θ-dependence of the complex eigenvalues in CCR methods, and in particular to converge the resonance widths. However, the term "very flexible" is used in comparison to standard basis sets for valence anions, and in fact good results are obtained for auto-ionizing resonances of He, H^-, and Be using the aug-cc-pVTZ+[3s3p] basis,[187] which includes three even-tempered diffuse s and p shells. This is not much different from the basis sets recommended here for proper description of loosely-bound electrons in general gas-phase calculations.

Since this methodology is fairly new to mainstream quantum chemistry, it is impossible to provide a broad overview of its performance at this time, so let us close this section instead with a provocative example,[187] illustrating the fundamental importance of such methods. Earlier in this chapter, we introduced *p*-coumaric acid as a molecule with an auto-ionizing resonance, in the sense that its $S_1(\pi\pi^*)$ bright state lies above its adiabatic electron detachment energy. (The molecule in question was introduced previously in Figure 16, but its structure is reproduced here in Figure 34.) This particular molecule carries significant chemical interest insofar as it is a simplified model of the chromophore in photoactive yellow protein.[188] In Figure 34, we show a large number of excitation energies computed for this molecule,[187] in a sequence

of increasingly diffuse basis sets, at the level of singles configuration interaction (CIS). By the time one has put a single set of diffuse functions on all atoms (6-31++G**), the $^1\pi\pi^*$ excited state – which can be identified either by inspecting the orbitals involved in the transition, or more easily by examining oscillator strengths – is *not* the lowest energy excitation! That honor goes instead to an excitation that transfers an electron from the π system into the diffuse orbitals, with very little oscillator strength. Adding more and more diffuse shells results in an increasingly large density of states corresponding to excitations of the latter type, to the point where these π-to-diffuse excitations start to mix strongly with the $\pi \rightarrow \pi^*$ excitations, gradually bleeding the oscillator strength out of the latter. (This is reminiscent of the manner in which spurious, low-energy charge-transfer states predicted by TD-DFT with asymptotically incorrect exchange-correlation functionals can form a dense manifold that steals intensity from the true bright states.[397])

The explanation of the behavior in Figure 34 is the following. The auto-ionizing nature of the $S_1(\pi\pi^*)$ state means that it is *not* the lowest energy excited state at the S_0 geometry; an electron-detached state is lower. As the finite basis set extends farther into space, more and more ODC states appear

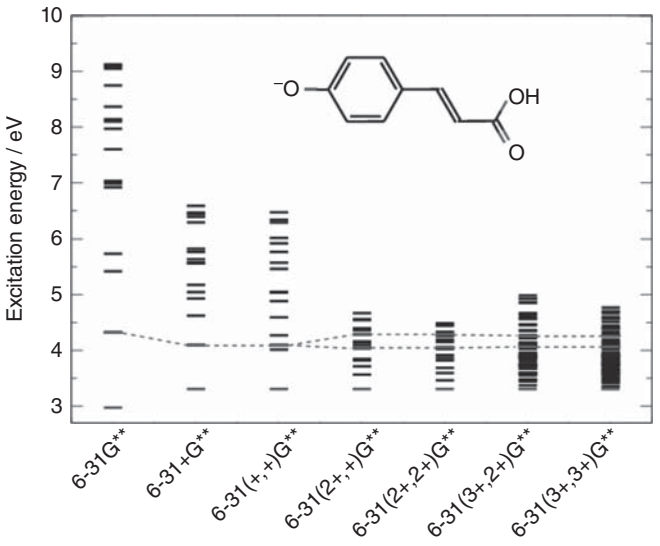

Figure 34 CIS calculations, in a sequence of increasingly diffuse basis sets, for the phenolate isomer of *p*-coumaric acid, a chemical model of the chromophore in photoactive yellow protein. (The energy level structure of this molecule is depicted in Figure 16.) Dashed lines connect the $\pi \rightarrow \pi^*$ transition(s) obtained in each basis, which mix with the continuum states in the more diffuse basis sets. The lowest-energy level in each basis set represents $-\epsilon_{\mathrm{HOMO}}$, which is the threshold energy for the onset of the continuum in the basis-set limit.[396] The other levels denote CIS excitation energies, most of which correspond to discretized continuum states. Adapted with permission from Ref. 187; copyright 2013 American Institute of Physics.

at energies below the $^1\pi\pi^*$ state. This type of behavior is expected whenever the lowest electronic excitation energy lies above $-\epsilon_{\mathrm{HOMO}}$, which represents the threshold energy for the onset of the continuum states in a complete-basis CIS (or complete-basis TD-DFT) calculation.[396,187] This type of behavior may well be endemic for electronically excited states of anions (it is well known, for example, in the case of the aqueous halide anions[398]), suggesting that methods appropriate for *metastable* states may be necessary in many such cases. To date, these considerations have not been widely recognized.

Moreover, in aqueous solution there is always a solvated-electron energy level sitting $\sim$3.5 eV below vacuum level, and the $S_0 \rightarrow S_1$ excitation of an aqueous chromophore may be enough energy to access such a state. Common aromatic chromophores have photoionization thresholds corresponding to ultraviolet wavelengths (e.g., 4.35 eV for indole[399]), so that these solvated-electron states may be very much in play in solution-phase photochemistry and photophysics.[92] The molecular-level details of the electron ejection process, and the structure of the initially formed solvated electron, remain poorly understood.

Stabilization Methods

As compared to the complex-scaling method described earlier, the methods discussed in this section have been used more widely in quantum chemistry, although the *proper* computation of temporary anion resonances (as opposed to dubious calculation of random ODC states) continues to be a niche market. Historically, stabilization methods were introduced as an alternative to quantum scattering methods,[400] by means of which resonances could be located by solving a Schrödinger equation for bound-state energy levels only. In the present context, this means that the well-developed machinery of bound-state quantum chemistry can be deployed to compute temporary anion resonances. The basic idea (stated here using the language of a temporary anion resonance, although the technique is more general[400]) is to first stabilize an otherwise metastable anion M^- by placing it in confining potential and thereby converting it into a bound state, whose energy can be computed using standard methods. Then, by examining how that bound-state energy level varies as a function of the spatial extent of the confining potential, the resonance energy can be extracted as described below. (With some additional effort, resonance widths can be extracted as well.) In effect, we aim to place the molecule into a box that is large enough so that its presence does not perturb the energy levels of the neutral molecule. Assuming this is so, then the effect of the box (confining potential) is to modulate the kinetic energy of the extra electron, whereas the molecular energy levels should not be significantly perturbed.

Exponent Stabilization and Analytic Continuation

In the context of quantum chemistry, a finite Gaussian basis set provides a natural confining potential, because any region of space that is not supported by basis functions is in effect subject to a potential of $+\infty$. In what is sometimes known as the *exponent stabilization method*,[369,401] one first selects a Gaussian basis set that is appropriate to describe the molecule, M, then constructs an adjustable confining potential simply by adding additional diffuse basis functions and scaling their orbital exponents, $\zeta \rightarrow \eta\zeta$. This is tantamount to varying the size of the box in which M^- is confined. The additional diffuse functions should include s, p, d, … angular momentum functions as appropriate to describe any centrifugal barrier that might exist in the electron–molecule potential (see Figure 14).

The exponent stabilization method consists of a sequence of bound-state calculations in which various energy levels of M^- are computed as a function of the scaling parameter, η. Properly speaking, one should compute actual electronic states of M^-. At a simple level, however, this might consist of attaching the electron to different orbitals of the neutral molecule, using KT estimates of the VAE, or perhaps by performing a proper SCF calculation to include orbital relaxation. The MOM can be used in the case that the electron is attached to an orbital of M other than the HOMO. (To date, most applications of the exponent stabilization method have been to small molecules where orbital symmetry may prevent collapse to the HOMO.) Figure 35(a) provides a schematic depiction of the results,[2] which are η-dependent energy levels for M^-, while Figure 35(b) and (c) provide examples from actual calculations.[402,368] A fixed value of η in these plots corresponds to a particular set of orbital exponents, and a vertical slice through the stabilization graph therefore represents the energies computed for various states of M^- (measured, for convenience, relative to the energy of neutral M). It is important to bear in mind that these states are generally ODC states, none of which need represent a true temporary anion resonance, but rather an electron that is artificially confined by a finite basis set. Techniques to extract the resonance energies and widths from these plots are discussed below.

The true resonance energy can be extracted by examining the η-dependence of these pseudo-bound-state energies. To understand how, let us first understand the behavior of the curves sketched in Figure 35(a). Note that the action of the radial kinetic energy operator, $\hat{T}_r$, on a Gaussian basis function $\exp(-\eta\zeta r^2)$, is

$$\hat{T}_r \; e^{-\eta\zeta r^2} = \left[-\frac{\hbar^2}{2mr^2} \frac{\partial}{\partial r} \left(r^2 \frac{\partial}{\partial r} \right) \right] e^{-\eta\zeta r^2} = -\frac{\hbar^2 \eta\zeta}{m} (2\eta\zeta r^2 - 3) e^{-\eta\zeta r^2} \qquad [66]$$

For an anion that is bound only by the confining potential, one expects the largest contribution to the wave function to come from the Gaussian(s) with the smallest exponent, and Eq. [66] suggests that the energy of such a state

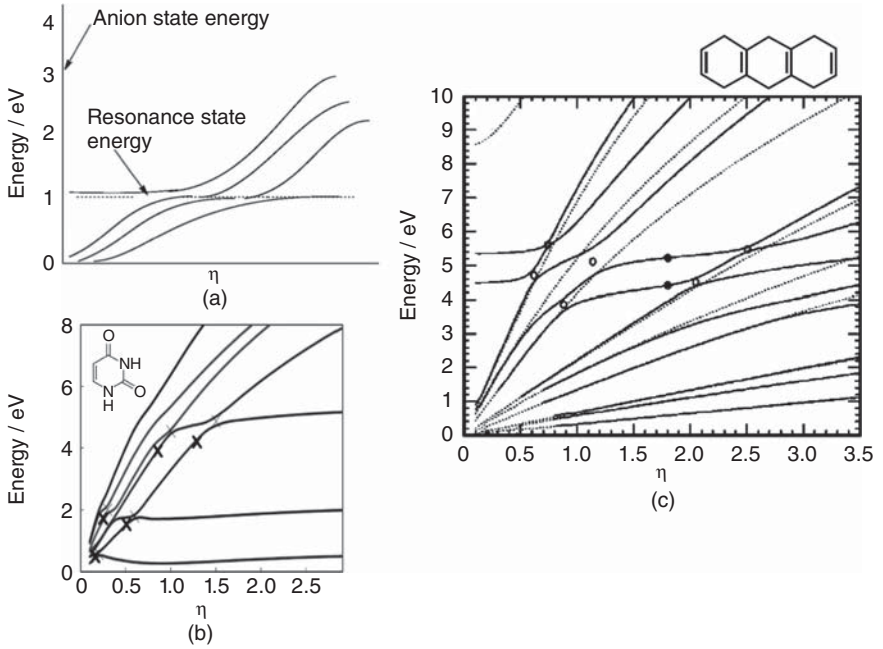

Figure 35 (a) Schematic illustration of the stabilization method, wherein anion energies are computed as a function of a dimensionless parameter, η, that is used to scale the diffuse basis function exponents. (b) Data for the a″ orbitals [$(\pi^*)^-$ electron-attached states] of $(\text{uracil})^-$, in which crosses mark the locations of avoided crossings. ODC states that are unaffected by exponent scaling have been removed from this plot. (c) Data for electron attachment to a_u orbitals of 1,4,5,8,9,10-hexahydroanthracene (whose structure is shown at the top of the figure), where the open circles indicate avoided crossings and the two filled circles are located on relatively stable plateaus at $\eta = 1.8$. The dashed curves are states that are not affected by interactions with any resonance state(s). Panel (a) is reprinted with permission from Ref. 2; copyright 2008 American Chemical Society. Panel (b) is adapted with permission from Ref. 368; copyright 2011 American Chemical Society. Panel (c) is reprinted with permission from Ref. 402; copyright 2000 American Institute of Physics.

should vary as η^2 for large r. At certain energies, however, the extra electron's wave function is precisely matched – in magnitude, slope, and phase – for resonant enhancement by the molecular potential, and the result is that the $\sim \eta^2$ dependence of the energy levels vanishes as the electron's wave function becomes localized on the molecule. The result is a plateau in $E(\eta)$, as depicted in Figure 35(a), and avoided crossings that can be understood in terms of the interaction between a bound state of the molecule and a continuum (ODC) state. [Some of these avoided crossings are indicated in Figure 35(b).] The location of the avoided crossing(s) identifies the true resonance energy or energies. A free electron with these special kinetic energies can be captured by the molecular

potential, so that the energy of the resulting anion is only weakly dependent on η in the vicinity of the resonance.

As suggested in the schematic example of Figure 35(a), one sometimes observes a "plateau" in the $E(\eta)$ curves, or in other words a range of η over which the energy is approximately independent of η. The origin of this behavior is that the electron's wave function has localized on the molecule, and thus its size is controlled by the spatial extent of the *molecular* potential rather than the artificial confining potential introduced by the finite basis set. In such cases, one may safely identify the resonance energy as the energy of the plateau in $E(\eta)$. Alternatively, one may estimate the resonance energy by finding the point of the closest approach (call it η_0) of two $E(\eta)$ curves and simply taking the average of the two $E(\eta)$ values:

$$E_R \approx \frac{1}{2}[E_1(\eta_0) + E_2(\eta_0)] \qquad [67]$$

This is the procedure suggested by the dashed lines in Figure 35(a). It has been called the *midpoint method*,[233] and is basically equivalent to setting E_R to be the energy of the "plateau," in the case where the plateau exists and the avoided crossings are well separated.

Unfortunately, the complexity of the real stabilization graphs is often significantly greater than that of the idealized example in Figure 35(a). In Figure 35(c), for example, two plateau-like regions can be identified, and the point $\eta = 1.8$ is singled out in this figure because it was found to lie in the middle of the plateau for other, similar molecules.[402] For this particular molecule, however, the "plateaus" in Figure 35(c) are constant to no better than $\sim$0.5 eV. Moreover, there are numerous avoided crossings and some states (the dashed curves) that lack any avoided crossings at all. The latter are ODC states that, for one reason or another, do not interact strongly with the resonances. Data for $(\text{uracil})^-$ [Figure 35(b)] show hardly any plateaus at all, and the value of $E(\eta)$ also changes significantly as one moves through the region of the avoided crossing.

For these more complicated cases, more sophisticated methods for extracting the resonance energy are required. Such methods are based on fitting $E_1(\eta)$ and $E_2(\eta)$ in the region near η_0 and then analytically continuing the energy into the complex plane, taking advantage of the fact that the complex energy in Eq. [61] should correspond to a stationary point, $\partial E/\partial\overline{\eta} = 0$, for complex $\overline{\eta}$.[403–406] (The notation $\overline{\eta}$ will be used whenever the real scaling parameter η has been analytically continued into the complex plane.) While these approaches are more complicated, they are also more rigorous, and provide the resonance width Γ in addition to its energy. Two variants of the analytic continuation method are described later.

To understand these methods, first consider the underlying physics of the avoided crossings in the stabilization graphs. These arise due to the interaction

between a bound state and a continuum state, with a noncrossing rule in one dimension as the parameter η is varied. This suggests a two-state model,[403,405]

$$\mathbf{H} = \begin{pmatrix} H_1(\eta) & V(\eta) \\ V(\eta) & H_2(\eta) \end{pmatrix} \qquad [68]$$

in which H_1 represents a slowly-varying resonance root and H_2 is a continuum root that couples to the resonance, with a coupling V. This two-state Hamiltonian has eigenvalues

$$E_{\pm}(\eta) = \frac{1}{2}H_{+}(\eta) \pm \frac{1}{2}\left\{[H_{-}(\eta)]^2 + 4[V(\eta)]^2\right\}^{1/2} \qquad [69]$$

where $H_{\pm} = H_1 \pm H_2$. The two branches of the avoided crossing are to be understood as data sets representing the functions $E_{+}(\eta)$ and $E_{-}(\eta)$.

One possible analytic continuation procedure is as follows.[405] Since the data plotted in the stabilization graphs are $E_{\pm}(\eta)$, one can express the three unknown functions $H_1(\eta)$, $H_2(\eta)$, and $V(\eta)$ as polynomials whose coefficients are determined by fitting to one or both branches of the $E_{\pm}(\eta)$ data, using the two-state model of Eq. [69]. Once these polynomial coefficients are fixed, one then analytically continues the functions H_1, H_2, and V into the complex plane by solving for the *complex* value $\overline{\eta}_0$ such that $E_{+}(\overline{\eta}_0) = E_{-}(\overline{\eta}_0)$. Thus, $\overline{\eta}_0$ is the solution to the equation

$$[H_{-}(\overline{\eta}_0)]^2 + 4[V(\overline{\eta}_0)]^2 = 0 \qquad [70]$$

Having found $\overline{\eta}_0$, one then expands the two eigenvalues $E_{\pm}(\overline{\eta})$ in the vicinity of $\overline{\eta}_0$ and searches for a stationary point where $\partial E/\partial\overline{\eta} = 0$. This stationary point is the complex energy in Eq. [61], from which one obtains E_R and Γ.

An alternative way to perform the analytic continuation is based on generalized Padé approximations.[403,406,368] In this approach, the energy E is taken to be a solution to the polynomial equation

$$E^3P_3 + E^2P_2 + EP_1 + P_0 = 0 \ , \qquad [71]$$

in which each P_k is itself a polynomial in η:

$$P_0(\eta) = c_{0,0} + c_{0,1}\eta + \cdots + c_{0,m_0}\eta^{m_0} \qquad [72]$$

$$P_1(\eta) = c_{1,0} + c_{1,1}\eta + \cdots + c_{1,m_1}\eta^{m_1} \qquad [73]$$

$$P_2(\eta) = c_{2,0} + c_{2,1}\eta + \cdots + c_{2,m_2}\eta^{m_2} \qquad [74]$$

$$P_3(\eta) = 1 + c_{3,1}\eta + \cdots + c_{3,m_3}\eta^{m_3} \ . \qquad [75]$$

The cubic polynomial for the energy in Eq. [71] allows for the possibility that three states might be strongly interacting in the vicinity of the avoided crossing.[406] If only two states are strongly interacting, as assumed in the analytic continuation procedure based on the two-state model in Eqs. [68] and [69], then one may set $P_3 \equiv 0$ in Eq. [71] and set $c_{2,0} = 1$ in Eq. [74]. As earlier, the data points for determining the polynomial coefficients are points (η, E) along the stabilization graphs. Given $m_0 + m_1 + m_2 + m_3 + 3$ such data points, all coefficients in Eq. [35] can be determined exactly, since there are exactly as many (η, E) data points as there are parameters to define the polynomials P_k. (In the two-state case, only $m_0 + m_1 + m_2 + 2$ data points are required.)

Once the polynomial coefficients in Eq. [35] are determined, they are taken to be fixed parameters, but η is allowed to become complex, and Eq. [71] for the energy is extended into the complex plane. One searches for complex roots E that are also stationary, $\partial E/\partial\overline{\eta} = 0$. The quality of the results is sensitive to the quality of the (η, E) data and also to the order of the polynomials in Eq. [35]; in recent applications, the quadratic (two-state) version of the procedure with $m_0 = m_1 = m_2 = 3$, 4, or 5 has been used.[368] It should be noted that this procedure can produce spurious roots[368] (which tend to appear far from the real line), just as it is not clear *a priori* which root in Eq. [69] is the physically correct one.[405] If the (η, E) data are accurate, the $E(\eta)$ fits are good, and the nonlinear search for stationary points is thorough, then it is claimed that these spurious solutions should be easy to identify,[404,405,368] as they are sensitive to the number and choice of the points (η, E) used in the analytic continuation procedure.[368]

In principle one may construct a stabilization graph by computing the energies of various electronic states (including excited states) of M^- at various values of η, each corresponding to a different set of orbital exponents. In practice, the calculation of proper electronic excited states is usually unnecessary, and sufficient accuracy to assign experimental VAEs (obtained from electron transmission spectroscopy[184,185,2]) can be achieved using simple modifications of the KT VAEs, which are equal to $-\varepsilon_{\text{virtual}}$. Often, electron transmission spectra are assigned on the basis of empirical shifting and scaling of the virtual MO eigenvalues to match known data in similar molecules,[233,407,125] as in Eq. [32] for example. In doing so, it is important to use relatively compact basis sets, as the low-lying virtual orbitals will mix with ODC states as one approaches the basis-set limit, and any correspondence between virtual MOs and actual electronic states of M^- will be lost.

From an *ab initio* perspective, a more satisfying procedure, yet one that is still enormously simpler than computing proper anion electronic states, is to use a stabilized version of KT.[406,366,408,401,367,409,368] This approach amounts to the approximation $E(\eta) \approx -\varepsilon_{\text{virtual}}(\eta)$, that is, the virtual MO eigenvalues are used to construct the stabilization graphs, from which resonance energies can be extracted either using the midpoint method (Eq. [67]) or else by proper analytic

continuation. Recently, Chen and coworkers have explored this technique using virtual MOs from KS DFT, with good results obtained when LRC functionals with correct asymptotic behavior are used.[401,409,368] There is a formal objection along the lines that incorporating Hartree–Fock exchange into these functionals serves to push the Kohn–Sham eigenvalue spectrum (which is fundamentally an approximate electronic excitation spectrum) toward the Hartree–Fock spectrum (where the HOMO–LUMO gap approximates IP – EA, but the occupied → virtual transitions are poor approximations to electronic excitations),[318] thereby defiling the meaning of the KS DFT orbital energies. For VDE calculations, however, this choice may be justified.

Table 9 shows an example, for the case of $(\pi^*)^-$ and $(\sigma^*)^-$ resonances of $(\text{uracil})^-$. Stabilized KT (S-KT) results are shown for the LRC functional ωB97X-D;[410] the "double hybrid" functional B2PLYP-D,[411] which mixes MP2 and DFT correlation as well as Hartree–Fock and DFT exchange; and the meta-GGA functional M06-HF.[320] Experimentally, only the $(\pi^*)^-$ resonances have been measured by electron transmission spectroscopy,[407] as the $(\sigma^*)^-$ resonances are shorter-lived. The S-KT results for all three functionals, which are based on stabilization graphs resembling the one in Figure 35(b), are in reasonable agreement with the lowest two $(\pi^*)^-$ VAEs measured experimentally, with differences of 0.2–0.3 eV that are comparable to the differences between the resonance energies (E_R) obtained with the three different functionals. In contrast, when Hartree–Fock virtual orbital energies are used [S-KT(HF)], the accuracy is unacceptable. Even for the DFT results, the agreement is less good for the third $(\pi^*)^-$ resonance, but at least good enough to assign the experimental spectrum. Note also that the resonance energies obtained using the midpoint method are nearly identical to those obtained using analytic continuation based on Padé approximations, although only the latter method affords resonance widths. Both the resonance energies and widths are in good agreement with the results of several quantum scattering calculations,[23,89,26] although there are other scattering calculations in the literature that place these resonances 1–2 eV higher in energy.[368] Overall, this $(\text{uracil})^-$ example demonstrates the limits of how accurately one can expect to obtain resonance energies via the exponent stabilization method.

Extrapolation into the Metastable Domain

The advantage of the exponent stabilization method is that all necessary calculations can be performed using standard quantum chemistry codes, without modification. This makes such calculations readily accessible to the average chemist, and in addition various levels of theory can be brought to bear to compute the $E(\eta)$ stabilization curves. That said, the procedure is somewhat more complicated as compared to ordinary bound-state quantum chemistry calculations, because multiple states of M^- must be calculated, the stabilization graphs must be fit to analytic functions in the avoided crossing region(s), and finally these functions must be analytically continued and stationary points located

Table 9 Resonance Energies and Widths (Both in eV) for the Lowest Temporary Anion Resonances of Uracil

		$\pi^*(a'')$ Resonances						$\sigma^*(a')$ Resonances					
Method	Ref.	E_R	Γ	E_R	Γ	E_R	Γ	E_R	Γ	E_R	Γ	E_R	Γ
Shifted and scaled $\varepsilon_{virtual}$[a]	125, 407	0.22		1.61		5.01		2.26		3.67		3.87	
S-KT(HF), midpt. method[b]	368	2.07		4.21		7.59		6.03		6.29		7.60	
S-KT(ωB97X-D), midpt. method[c]	368	0.40		1.74		4.53		2.45		4.32		4.79	
S-KT(ωB97X-D), 3rd-order Padé[c,d]	368	0.36	0.04	1.69	0.17	4.58	0.27	2.35	1.94	4.35	0.77	4.82	0.68
S-KT(ωB97X-D), 5th-order Padé[c,e]	368	0.36	0.05	1.75	0.10	4.52	0.23	2.20	1.62	4.28	0.86	4.68	0.67
S-KT(B2PLYP-D), midpt. method[c]	368	0.11		1.51		4.30		1.57		3.75		4.11	
S-KT(B2PLYP-D), 3rd-order Padé[c,d]	368	0.06	0.08	1.52	0.15	4.33	0.33	1.52	1.53	3.86	0.81	4.11	0.53
S-KT(M06-HF), midpt. method[c]	368	0.44		2.01		5.26		1.81		4.29		4.45	
S-KT(M06-HF), 3rd-order Padé[c,d]	368	0.46	0.08	2.06	0.24	5.29	0.27	1.84	1.90	4.15	0.89	4.50	0.64
Quantum scattering	23	0.32	0.02	1.91	0.16	5.08		1.45		4.5		4.5	
Quantum scattering	26	0.13	0.00	1.94	0.17	4.95	0.38						
Quantum scattering	89	0.33		1.70		3.50							
Experiment	407	0.22		1.58		3.83							

[a]Scaled Hartree–Fock/6-31G* virtual orbital shifted and scaled to match the lowest experimental resonance.[407]
[b]Basis set is 6-31G* augmented with a set of sp diffuse functions.
[c]Basis set is aug-cc-pVDZ with the most diffuse exponent on each atom scaled by η.
[d]Padé approximation with $m_0 = m_1 = m_2 = 3$ (Eq. [35]).
[e]Padé approximation with $m_0 = m_1 = m_2 = 5$ (Eq. [35]).

in the complex plane. In the end, however, one obtains not just the resonance energy but also the resonance width.

An alternative *charge stabilization method* has been suggested for computing resonance energies (only),[412,413] which is simpler insofar as computing multiple states of M^- is not required. (This method has also been called *Z*-extrapolation, for reasons that will become clear.) The idea is to identify the likely binding site for the extra electron and then artificially increase the atomic numbers (Z) of one or more nearby nuclei. For sufficiently large values of Z, the anion M^- should be converted to a bound state treatable with standard quantum chemistry methods. Calculations are performed at a variety of nuclear charges, and the actual resonance energy is approximated as

$$E_R = \lim_{Z \to Z_0} E(\eta) \qquad [76]$$

where Z_0 denotes the actual atomic number. The success of this method depends critically on using values of Z that do indeed transform M^- into a bound state.

An example is shown in Figure 36 for the case of SO_4^{2-}.[414] This species is an example of a metastable dianion of the sort suggested in Figure 4(b), where the dianion can exist only when trapped behind the RCB to e^- detachment. As such, the lowest-energy state of gas-phase SO_4^{2-} in a finite basis set corresponds

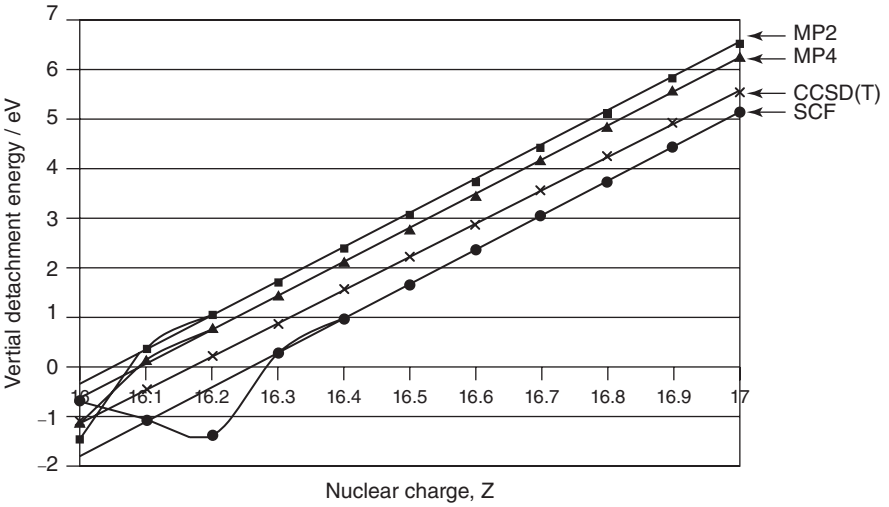

Figure 36 Variation of the VDE for the sulfate dianion, VDE = $E(SO_4^{2-}) - E(SO_4^-)$, as a function of the atomic number, Z, that is assigned to the sulfur atom. In cases where VDE < 0, the scaling of Z is insufficient to convert SO_4^{2-} into a bound state; these data points should be discarded. Reprinted with permission from Ref. 414; copyright 2002 American Institute of Physics.

to an ODC state as discussed above, and the energetics from bound-state quantum chemistry calculations should not be trusted for this species. However, an increase of the sulfur atom's atomic number by 0.1–0.3 (depending on the level of theory) is sufficient to obtain a bound state whose energetics *can* be trusted and can be extrapolated back to $Z_0 = 16$. Plots of the VDE as a function of Z (Figure 36) are remarkably linear except close to $Z = 16$, where the dianion is unbound. These unbound data points should not be used in the extrapolation.

Figure 37 shows an example of the charge stabilization method as applied to several different electronic states of O_2^- computed at a high level of theory, CCSD(T)/aug-cc-pVTZ. (Each state has a different symmetry and thus can be computed from a reference determinant of appropriate symmetry, as if it were the ground state.) Excellent agreement with spectroscopic potentials is obtained, demonstrating the feasibility of this method. Other studies have shown that this Z-extrapolation method affords resonance energies in good

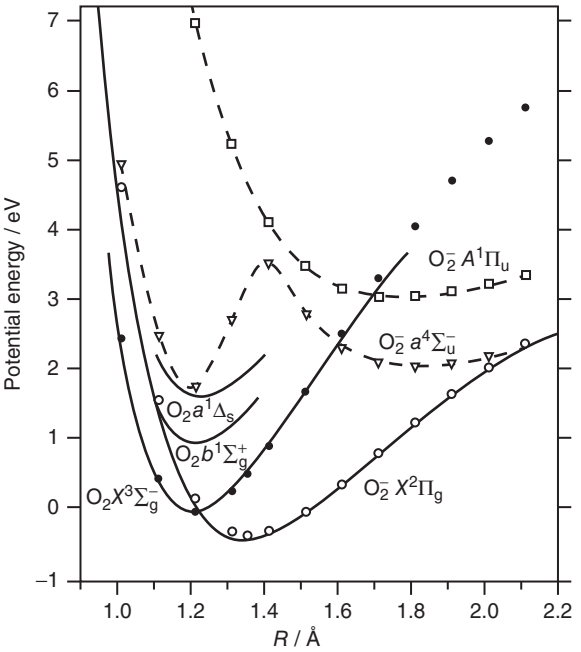

Figure 37 Potential energy curves for the ground state ($X^3\Sigma_g^-$) of O_2 (solid circles) along with three different states of O_2^-: the $X\ ^2\Pi_g$ state (open circles), the $a^4\Sigma_u^-$ state (inverted triangles), and the $A^2\ \Pi_u$ state (squares). The solid curves are derived from experimental spectroscopic parameters, whereas the data points come from theory. All points where O_2^- is not the lowest-energy species were obtained using the charge stabilization method at the CCSD(T)/aug-cc-pVTZ level. Reprinted with permission from Ref. 415; copyright 2003 American Chemical Society.

agreement with those obtained from methods based on complex absorbing potentials, provided that one extrapolates the VAE rather than the total energy.[416] (This is implicit in the stabilization graphs shown in Figure 36.) It was also recommended in Ref. 416 to scale the Gaussian exponents by a factor of $(Z/Z_0)^2$, so as to provide a balanced basis set for each value of Z. (Recall that the radial wave functions for a one-electron atom decay as e^{-Zr/a_0}, so the corresponding Gaussian basis function looks like $e^{-Z^2\zeta r^2}$.)

A clever alternative to Z-extrapolation has been introduced by Cederbaum and coworkers,[416] for cases where one-dimensional potentials are desired along some relatively simple distance coordinate. The proposed "R-extrapolation" technique is based upon the observation that the attachment energy VAE(R) is often nearly linear in R, or at least the curvature is such that VAE(R) can easily be fit to a low-order polynomial, unlike potential energy curves. This is shown in Figure 38(a) for N_2^- and CO_2^-. The solid VAE(R) curves have been computed in the region where the anion is lower in energy than the neutral molecule, then extrapolated into the region $R \gtrsim 1.4$ Å where the anion is metastable. Alternative methods based on complex absorbing potentials (open symbols in the figure) can be performed on both sides of the metastability threshold $R_c \approx 1.4$ Å, and agree quite well with the R-extrapolated results.[416] Adding the VAE(R) curve (in both the stable and metastable domains) to potential energy curves for the neutral molecule then affords a reasonable potential energy curve for the anion, on both sides of the metastability threshold. This is shown in Figure 38(b).

In both the Z- and R-extrapolation examples, only resonance energies were computed, not resonance widths. To date, that seems to be the state of things: resonance widths have been extracted only on the basis of the exponent stabilization technique, not by Z- or R-extrapolation. However, we note that the analytic continuation procedure discussed above in the context of exponent stabilization has also been used in conjunction with an alternative stabilization technique in which the anion is stabilized by placing it inside of a large spherical array of positive point charges,[417,418,406,366,408] which will convert the anion into a bound state if the charges are sufficiently large. Stabilization graphs, complete with avoided crossings, are then generated by varying either the magnitude of the charges or the radius of the spherical array, and analytic continuation that is based on Padé approximations is applied. The fact that this is a form of *charge* (rather than *exponent*) stabilization suggests that it might be possible to perform similar techniques on the basis of Z-extrapolation, if sufficiently diffuse basis functions were included, so that ODC states that might interact with the resonance states would appear in the calculations. In Ref. 416, it was demonstrated in the case of CO_2^- that avoided crossings could be generated as Z was varied, although no attempt was made to locate these quantitatively or to apply analytic continuation.

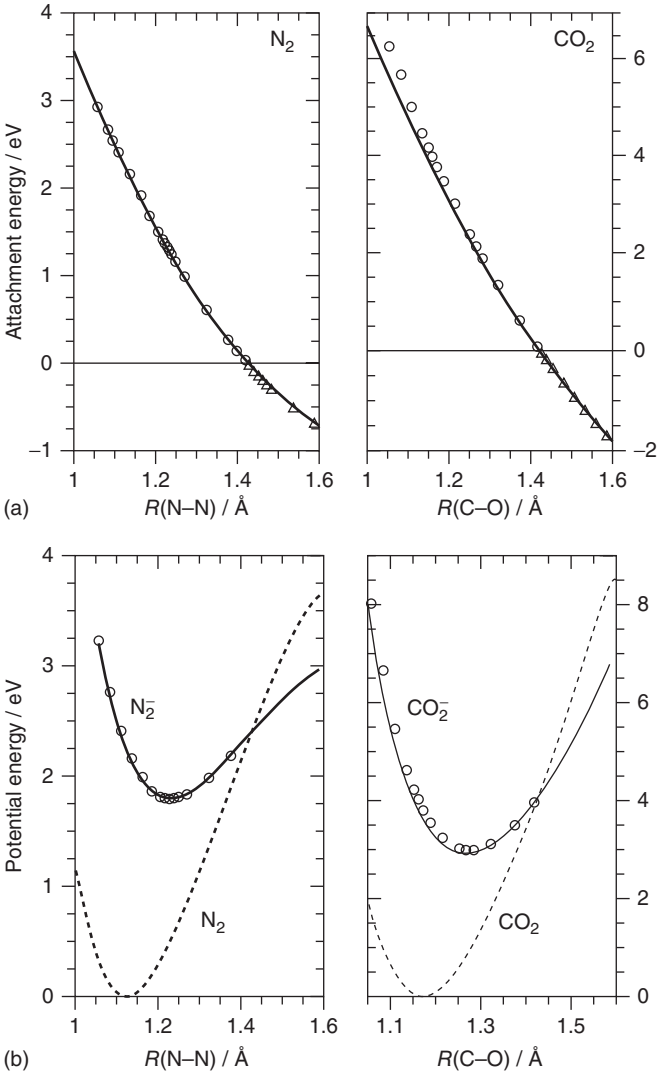

Figure 38 Demonstration of the *R*-extrapolation technique for N_2^- and CO_2^-. (a) Solid curves show the VAE for the anion, computed where the anion is stable and then extrapolated to larger bond lengths where the anion is metastable (VAE < 0). The open symbols represent calculations performed using a method that can be applied on both sides of the metastability threshold, which occurs around $R \approx 1.4$ Å. (A complex absorbing potential is used in the metastable region; see Ref. 416 for details.) (b) Potential energy curves, where the anion's potential was obtained by adding the VAE to the neutral molecule's potential energy curve. Reprinted with permission from Ref. 416; copyright 2004 American Institute of Physics.

CONCLUDING REMARKS

The loosely-bound electron, orphaned from any molecular unit and ranging far outside of the valence region as it is bound only by weak charge–multipole interactions, nevertheless manages to play a role in a variety of important chemical phenomena. These range from DEA reactions in the gas phase – where a weakly-bound anion may serve as a "doorway" to molecular dissociation – to putative DEA reactions in condensed phases. Solvated electrons *may* play a role in condensed-phase DEA, but in any case the solvated electron is undisputedly present as a reactive intermediates following solvent radiolysis. This species can actually be quite strongly bound, in the sense of its VDE, despite the fact that it is not strongly associated with any particular molecular unit and is bound only collectively by solvent molecules.

Quantum chemistry calculations for loosely-bound electrons come with some specialized demands in terms of the one-particle basis set, which must be "ultra-diffuse" in weakly-bound cases. (On the other hand, highly diffuse but double-ζ basis sets often suffice for the calculation of vertical detachment energies.) With that caveat about basis-set requirements, however, standard high-accuracy *ab initio* methods such as CCSD(T) continue to perform well, even for weakly-bound anions. Perturbative methods such as MP2 also work reasonably well, except in cases where the electron binding energy is exceedingly small ($\lesssim 0.05$ eV), such that the Hartree–Fock reference determinant is unbound or nearly so. DFT methods can also achieve semiquantitative accuracy (~ 0.1–0.3 eV), especially when SICs are employed. A promising route to correcting the SIE for weakly-bound anions is the use of LRC functionals. These appear to eliminate most of the SIE associated with the unpaired electron in doublet radical anions, especially when they are "tuned" to achieve a system-specific asymptotic correction, according to the criterion $\varepsilon_{\mathrm{HOMO}} = -\mathrm{IP}$.

While CCSD(T), MP2, DFT, and so on are appropriate for *bound* anions, theoretical description of *metastable* anions requires specialized techniques. Many of these techniques are well-established but have seen far less use as compared to bound-state quantum chemistry. In this chapter, we have discussed a variety of techniques (the maximum overlap method, CCR, and stabilization methods) that are all based, at some level, on modifications to bound-state quantum chemistry that can be implemented as reasonably straightforward modifications of standard bound-state quantum chemistry codes. It is this author's hope that this review of such methods for temporary anion resonances will prompt renewed and increased interest in these techniques.

ACKNOWLEDGMENTS

The author's own work on negative ions (primarily solvated electrons) has been supported over the years by the National Science Foundation (grant nos. CHE-0748448 and CHE-1300603, and a Mathematical Sciences Postdoctoral Fellowship), the Alfred P. Sloan Foundation, the Henry and

Camille Dreyfus Foundation, and through generous allocations of computing time from the Ohio Supercomputer Center (project nos. PAS-0291 and PAA-0003).

APPENDIX A: LIST OF ACRONYMS

ADC(2)	second-order algebraic diagrammatic construction
aDZ	aug-cc-pVDZ basis set
AEA	adiabatic electron affinity
aQZ	aug-cc-pVQZ basis set
aTZ	aug-cc-pVTZ basis set
CBS	complete basis set
CCSD	coupled-cluster theory with single and double excitations
CCSDT	coupled-cluster theory with single, double, and triple excitations
CCSD(T)	CCSD plus perturbative (noniterative) triple excitations
CIS	configuration interaction with single excitations
DEA	dissociative electron attachment
DFT	density-functional theory
EA	electron affinity
EOM-CCSD	equation-of-motion coupled-cluster theory
EOM-EA-CCSD	equation of motion coupled-cluster theory with electron attachment
EOM-IP-CCSD	equation of motion coupled-cluster theory with electron detachment
FWHM	full width at half maximum
GGA	generalized gradient approximation
HF	Hartree–Fock
HOMO	highest occupied molecular orbital
IP	ionization potential
KS	Kohn–Sham
KT	Koopmans' theorem
LDA	local density approximation
LRC-DFT	long-range-corrected density-functional theory
LUMO	lowest unoccupied molecular orbital
MBPT2	second-order many-body perturbation theory
MO	molecular orbital
MOM	maximum overlap method
MP2	second-order Møller–Plesset perturbation theory
MUE	mean unsigned error
ODC	orthogonalized discretized continuum
PCM	polarizable continuum model
QM/MM	quantum mechanics molecular mechanics
QMC	quantum Monte Carlo

RCB	repulsive Coulomb barrier
RI	resolution of identity
SCF	self-consistent field
SIC	self-interaction correction
SIE	self-interaction error
S-KT	stabilized Koopmans' theorem
SOMO	singly occupied molecular orbital
TD-DFT	time-dependent density-functional theory
VAE	vertical attachment energy
VDE	vertical detachment energy

REFERENCES

1. H. Hotop and W. C. Lineberger, *J. Phys. Chem. Ref. Data*, **14**, 731–750 (1985). Binding Energies in Atomic Negative Ions: II.
2. J. Simons, *J. Phys. Chem. A*, **112**, 6401–6511 (2008). Molecular Anions.
3. J. Simons, *Annu. Rev. Phys. Chem.*, **62**, 107–128 (2011). Theoretical Study of Negative Molecular Ions.
4. J. R. R. Verlet, A. E. Bragg, A. Kammrath, O. Cheshnovsky, and D. M. Neumark, *Science*, **307**, 93–96 (2005). Observation of Large Water-Cluster Anions with Surface-Bound Excess Electrons.
5. L. Ma, K. Majer, F. Chirot, and B. von Issendorff, *J. Chem. Phys.*, **131**, 144303:1–6 (2009). Low Temperature Photoelectron Spectra of Water Cluster Anions.
6. J. V. Coe, S. T. Arnold, J. G. Eaton, G. H. Lee, and K. H. Bowen, *J. Chem. Phys.*, **125** 014315: 1–11 (2006). Photoelectron Spectra of Hydrated Electron Clusters: Fitting Line Shapes and Grouping Isomers.
7. K. R. Siefermann, Y. Liu, E. Lugovoy, O. Link, M. Faubel, U. Buck, B. Winter, and B. Abel, *Nat. Chem.*, **2**, 274–279 (2010). Binding Energies, Lifetimes and Implications of Bulk and Interface Solvated Electrons in Water.
8. Y. Tang, H. Shen, K. Sekiguchi, N. Kurahashi, T. Mizuno, Y. I. Suzuki, and T. Suzuki, *Phys. Chem. Chem. Phys.*, **12**, 3653–3655 (2010). Direct Measurement of Vertical Binding Energy of a Hydrated Electron.
9. A. T. Shreve, T. A. Yen, and D. M. Neumark, *Chem. Phys. Lett.*, **493**, 216–219 (2010). Photoelectron Spectroscopy of Hydrated Electrons.
10. A. Lübcke, F. Buchner, N. Heine, I. V. Hertel, and T. Schultz, *Phys. Chem. Chem. Phys.*, **12**, 14629–14634 (2010). Time-Resolved Photoelectron Spectroscopy of Solvated Electrons in Aqueous NaI Solution.
11. K. D. Jordan and F. Wang, *Annu. Rev. Phys. Chem.*, **54**, 367–396 (2003). Theory of Dipole-Bound Anions.
12. C. R. Arumainayagam, H.-L. Lee, R. B. Nelson, D. R. Haines, and R. P. Gunawardane, *Surf. Sci. Rep.*, **65**, 1–44 (2010). Low-Energy Electron-Induced Reactions in Condensed Matter.
13. E. Alizadeh and L. Sanche, *Chem. Rev.*, **112**, 5578–5602 (2012). Precursors of Solvated Electrons in Radiobiological Physics and Chemistry.
14. J. Gu, J. Leszczynski, and H. F.Schaefer, III, *Chem. Rev.*, **112**, 5603–5640 (2012). Interaction of Electrons with Bare and Hydrated Biomolecules: From Nucleic Acid Bases to DNA Segments.

15. J. M. Herbert and L. D. Jacobson, *Int. Rev. Phys. Chem.*, **30**, 1–48 (2011). Nature's Most Squishy Ion: The Important Role of Solvent Polarization in the Description of the Hydrated Electron.
16. L. Turi and P. J. Rossky, *Chem. Rev.*, **112**, 5641–5674 (2012). Theoretical Studies of Spectroscopy and Dynamics of Hydrated Electrons.
17. B. C. Garrett, D. A. Dixon, D. M. Camaioni, D. M. Chipman, M. A. Johnson, C. D. Jonah, G. A. Kimmel, J. H. Miller, T. N. Rescigno, P. J. Rossky, S. S. Xantheas, S. D. Colson, A. H. Laufer, D. Ray, P. F. Barbara, D. M. Bartels, K. H. Becker, K. H.Bowen, Jr., S. E. Bradforth, I. Carmichael, J. V. Coe, L. R. Corrales, J. P. Cowin, M. Dupuis, K. B. Eisenthal, J. A. Franz, M. S. Gutowski, K. D. Jordan, B. D. Kay, J. A. LaVerne, S. V. Lymar, T. E. Madey, C. W. McCurdy, D. Meisel, S. Mukamel, A. R. Nilsson, T. M. Orlando, N. G. Petrik, S. M. Pimblott, J. R. Rustad, G. K. Schenter, S. J. Singer, A. Tokmakoff, L.-S. Wang, C. Wittig, and T. S. Zwier, *Chem. Rev.*, **105**, 355–389 (2005). Role of Water in Electron-Initiated Processes and Radical Chemistry: Issues and Scientific Advances.
18. M. Mostafavi and I. Lampre, in *Radiation Chemistry: From Basics to Applications in Material and Life Sciences*, M. Spotheim-Maurizot, M. Mostafavi, J. Belloni, and T. Douki (Eds.), EDP Sciences, 2008; chapter 3, pp. 33–52, The Solvated Electron: A Singular Chemical Species.
19. R. M. Young and D. M. Neumark, *Chem. Rev.*, **112**, 5553–5577 (2012). Dynamics of Solvated Electrons in Clusters.
20. K. D. Jordan, V. K. Voora, and J. Simons, *Theor. Chem. Acc.*, **133**, 1445:1–15 (2014). Negative Electron Affinities from Conventional Electronic Structure Methods.
21. F. A. Gianturco and R. R. Lucchese, *J. Chem. Phys.*, **120**, 7446–7455 (2004). Radiation Damage of Biosystems Mediated by Secondary Electrons: Resonant Precursors for Uracil Molecules.
22. S. Tonzani and C. H. Greene, *J. Chem. Phys.*, **122**, 014111:1–8 (2005). Electron–Molecule Scattering Calculations in a 3D Finite Element *R*-Matrix Approach.
23. C. Winstead and V. McKoy, *J. Chem. Phys.*, **125**, 174304:1–8 (2006). Low-Energy Electron Collisions with Gas-Phase Uracil.
24. C. Winstead and V. McKoy, *J. Chem. Phys.*, **125**, 244302:1–7 (2006). Interaction of Low-Energy Electrons with the Purine Bases, Nucleosides, and Nucleotides of DNA.
25. C. Winstead, V. McKoy, and S. d'Almeida Sanchez, *J. Chem. Phys.*, **127**, 085105:1–6 (2007). Interaction of Low-Energy Electrons with the Pyrimidine Bases and Nucleosides of DNA.
26. A. Dora, J. Tennyson, L. Bryjko, and T. van Mourik, *J. Chem. Phys.*, **130**, 164307:1–8 (2009). *R*-Matrix Calculation of Low-Energy Electron Collisions with Uracil.
27. U. Fano, *Phys. Rev.*, **124**, 1866–1878 (1961). Effects of Configuration Interaction on Intensities and Phase Shifts.
28. D. Chen and G. A. Gallup, *J. Chem. Phys.*, **93**, 8893–8901 (1990). The Relationship of the Virtual Orbitals of Self-Consistent-Field Theory to Temporary Negative Ions in Electron Scattering from Molecules.
29. R. Santra and L. S. Cederbaum, *J. Chem. Phys.*, **117**, 5511–5521 (2002). Complex Absorbing Potentials in the Framework of Electron Propagator Theory. I. General Formalism.
30. S. Feuerbacher, T. Sommerfeld, R. Santra, and L. S. Cederbaum, *J. Chem. Phys.*, **118**, 6188–6199 (2003). Complex Absorbing Potentials in the Framework of Electron Propagator Theory. II. Application to Temporary Anions.
31. T.-C. Jagau, D. Zuev, K. B. Bravaya, E. Epifanovsky, and A. I. Krylov, *J. Phys. Chem. Lett.*, **5**, 310–315 (2014). A Fresh Look at Resonances and Complex Absorbing Potentials: Density Matrix-Based Approach.
32. W. A. Al-Saidi, E. J. Walter, and A. M. Rappe, *Phys. Rev. B*, **77**(075112), 1–10 (2008). Optimized Norm-Conserving Hartree-Fock Pseudopotentials for Plane-Wave Calculations.
33. J. Heyd, G. E. Scuseria, and M. Ernzerhof, *J. Chem. Phys.*, **118**, 8207–8215 (2003). Hybrid Functionals Based on a Screened Coulomb Potential.

34. J. Paier, M. Marsman, K. Hummer, G. Kresse, I. C. Gerber, and J. G. Ángyán, *J. Chem. Phys.*, **124**, 154709:1–13 (2006). Screened Hybrid Density Functionals Applied to Solids.
35. A. Szabo and N. S. Ostlund, *Modern Quantum Chemistry*, Macmillan, New York, 1982.
36. R. J. Bartlett and J. F. Stanton, in *Reviews in Computational Chemistry*, K. B. Lipkowitz and D. B. Boyd (Eds.), Vol. 5, VCH Publishers, Inc., New York, 1993, pp. 65–169, Applications of Post-Hartree–Fock Methods: A Tutorial.
37. T. D. Crawford and H. F. Schaefer, III, in *Reviews in Computational Chemistry*, K. B. Lipkowitz and D. B. Boyd (Eds.), Vol. 14, VCH Publishers, Inc., New York, 2000, pp. 33–136, An Introduction to Coupled Cluster Theory for Computational Chemists.
38. F. Jensen, *Introduction to Computational Chemistry*, Wiley, 2006.
39. I. N. Levine, *Quantum Chemistry, Prentice Hall*, 6th edition, 2008.
40. F. M. Bickelhaupt and E. J. Baerends, in *Reviews in Computational Chemistry*, K. B. Lipkowitz and D. B. Boyd (Eds.), Vol. 15, VCH Publishers, Inc., New York, 2000, pp. 1–86, Kohn-Sham Density Functional Theory: Predicting and Understanding Chemistry.
41. P. Elliott, F. Furche, and K. Burke, in *Reviews in Computational Chemistry*, K. B. Lipkowitz and D. B. Boyd (Eds.), Vol. 26, VCH Publishers, Inc., New York, 2009, pp. 91–165, Excited States from Time-Dependent Density Functional Theory.
42. J. Simons, *J. Phys. Chem. A*, **114**, 8631–8643 (2010). One-Electron Electron–Molecule Potentials Consistent with ab Initio Møller–Plesset Theory.
43. J. C. Rienstra-Kiracofe, G. S. Tschumper, H. F. Schaefer III, S. Nandi, and G. B. Ellison, *Chem. Rev.*, **102**, 231–282 (2002). Atomic and Molecular Electron Affinities: Photoelectron Experiments and Theoretical Computations.
44. J. M. Galbraith and H. F. Schaefer III, *J. Chem. Phys.*, **105**, 862–864 (1996). Concerning the Applicability of Density Functional Methods to Atomic and Molecular Ions.
45. N. Rösch and S. B. Trickey, *J. Chem. Phys.*, **106**, 8940–8941 (1997). Comment on "Concerning the Applicability of Density Functional Methods to Atomic and Molecular Negative Ions" [J. Chem. Phys. 105, 862 (1996)].
46. D. Lee, F. Furche, and K. Burke, *J. Phys. Chem. Lett.*, **1**, 2124–2129 (2010). Accuracy of Electron Affinities of Atoms in Approximate Density Functional Theory.
47. J. Simons, *J. Am. Chem. Soc.*, **103**, 3971–3976 (1981). Propensity Rules for Vibration-Induced Electron Detachment of Anions.
48. P. K. Acharya, R. A. Kendall, and J. Simons, *J. Am. Chem. Soc.*, **106**, 3402–3407 (1984). Vibration-Induced Electron Detachment in Molecular Anions.
49. G. Chalasinski, R. A. Kendall, H. Taylor, and J. Simons, *J. Phys. Chem.*, **92**, 3086–3091 (1988). Propensity Rules for Vibration–Rotation-Induced Electron Detachment of Diatomic Anions: Application to $NH^- \rightarrow NH + e^-$.
50. G. V. Buxton, in *Radiation Chemistry: From Basics to Applications in Material and Life Sciences*, M. Spotheim-Maurizot, M. Mostafavi, J. Belloni, and T. Douki (Eds.). EDP Sciences, 2008; chapter 1, pp. 3–16, An Overview of the Radiation Chemistry of Liquids.
51. R. Balog and E. Illenberger, *Phys. Rev. Lett.*, **91**, 213201:1–4 (2003). Complete Chemical Transformation of a Molecular Film by Subexcitation Electrons (< 3 eV).
52. G. Dujardin, R. E. Walkup, and P. Avouris, *Science*, **255**, 1232–1235 (1992). Dissociation of Individual Molecules with Electrons from the Tip of a Scanning Tunneling Microscope.
53. S.-W. Hla, L. Bartels, G. Meyer, and K.-H. Rieder, *Phys. Rev. Lett.*, **85**, 2777–2780 (2000). Inducing All Steps of a Chemical Reaction with the Scanning Tunneling Microscope Tip: Towards Single Molecule Engineering.
54. Q.-B. Lu and L. Sanche, *Phys. Rev. Lett.*, **87**, 078501:1–4 (2001). Effects of Cosmic Rays on Atmospheric Chloroflurocarbon Dissociation and Ozone Depletion.
55. S. Ryu, J. Chang, H. Kwon, and S. K. Kim, *J. Am. Chem. Soc.*, **128**, 3500–3501 (2006). Dynamics of Solvated Electron Transfer in Thin Ice Film Leading to Large Enhancement in Photodissociation of $CFCl_3$.

56. Q.-B. Lu, *Phys. Rep.*, **487**, 141–167 (2010). Cosmic-Ray-Driven Electron-Induced Reactions of Halogenated Molecules Adsorbed on Ice Surfaces: Implications for Atmospheric Ozone Depletion and Global Climate Change.
57. J. Stähler, C. Gahl, and M. Wolf, *Acc. Chem. Res.*, **45**, 131–138 (2012). Dynamics and Reactivity of Trapped Electrons on Supported Ice Crystals.
58. J. Stähler, U. Bovensiepen, M. Meyer, and M. Wolf, *Chem. Soc. Rev.*, **37**, 2180–2190 (2008). A Surface Science Approach to Ultrafast Electron Transfer and Solvation Dynamics at Interfaces.
59. M. Bertin, M. Meyer, J. Stähler, C. Gahl, M. Wolf, and U. Bovensiepen, *Faraday Discuss.*, **141**, 293–307 (2009). Reactivity of Water–Electron Complexes on Crystalline Ice Surfaces.
60. U. Bovensiepen, C. Gahl, J. Stähler, M. Bockstedte, M. Meyer, F. Baletto, S. Scandolo, X.-Y. Zhu, A. Rubio, and M. Wolf, *J. Phys. Chem. C*, **113**, 979–988 (2009). A Dynamic Landscape from Femtoseconds to Minutes for Excess Electrons at Ice–Metal Interfaces.
61. F. P. Sargent and E. M. Gardy, *Chem. Phys. Lett.*, **39**, 188–190 (1976). Direct ESR Detection of the Solvated Electron in Pulse Irradiated Liquid Water.
62. G. V. Buxton, C. L. Greenstock, W. P. Helman, and A. B. Ross, *J. Phys. Chem. Ref. Data*, **17**, 513–886 (1988). Critical Review of Rate Constants for Reactions of Hydrated Electrons, Hydrogen Atoms and Hydroxyl Radicals ($^{\bullet}$OH/$^{\bullet}$O) in Aqueous Solution.
63. N. R. P. Harris, J. C. Farman, and D. W. Fahey, *Phys. Rev. Lett.*, **89**, 219801 (2002). Comment on "Effects of Cosmic Rays on Atmospheric Chlorofluorocarbon Dissociation and Ozone Depletion".
64. Q.-B. Lu and L. Sanche, *Phys. Rev. Lett.*, **89**, 219802 (2002). Reply to "Comment on Effects of Cosmic Rays on Atmospheric Chlorofluorocarbon Dissociation and Ozone Depletion".
65. P. K. Patra and M. S. Santhanam, *Phys. Rev. Lett.*, **89**, 219803 (2002). Comment on "Effects of Cosmic Rays on Atmospheric Chlorofluorocarbon Dissociation and Ozone Depletion".
66. Q.-B. Lu and L. Sanche, *Phys. Rev. Lett.*, **89**, 219804 (2002). Reply to "Comment on Effects of Cosmic Rays on Atmospheric Chlorofluorocarbon Dissociation and Ozone Depletion".
67. R. Müller, *Phys. Rev. Lett.*, **91**, 058502:1–4 (2003). Impact of Cosmic Rays on Stratospheric Chlorine Chemistry and Ozone Depletion.
68. R. Müller, *J. Chem. Phys.*, **129**, 027101:1–2 (2008). Comment on "Resonant Dissociative Electron Transfer of the Presolvated Electron to CCl_4 in Liquid: Direct Observation and Lifetime of the CCl_4^{*-} Transition State" [J. Chem. Phys. 128, 041102 (2008)].
69. C.-R. Wang, K. Drew, T. Luo, M.-J. Lu, and Q.-B. Lu, *J. Chem. Phys.*, **129**, 027102:1–2 (2008). Response to "Comment on 'Resonant Dissociative Electron Transfer of the Presolvated Electron to CCl_4 in Liquid: Direct Observation and Lifetime of the CCl_4^{*-} Transition State" [J. Chem. Phys. 129, 027101 (2008)]".
70. R. Müller and J.-U. Grooß, *Phys. Rev. Lett.*, **103**, 228501:1–4 (2009). Does Cosmic-Ray-Induced Heterogeneous Chemistry Influence Stratospheric Polar Ozone Loss?
71. J.-U. Grooß and R. Müller, *Atmos. Environ.*, **45**, 3508–3514 (2011). Do Cosmic Ray-Driven Electron-Induced Reactions Impact Stratospheric Ozone Depletion and Global Climate Change?
72. R. A. Zubarev, N. L. Kelleher, and F. W. McLafferty, *J. Am. Chem. Soc.*, **120**, 3265–3266 (1998). Electron Capture Dissociation of Multiply Charged Protein Cations. A Nonergodic Process.
73. J. E. P. Syka, J. J. Coon, M. J. Schroeder, J. Shabanowitz, and D. F. Hunt, *Proc. Natl. Acad. Sci. U.S.A.*, **101**, 9528–9533 (2004). Peptide and Protein Sequence Analysis by Electron Transfer Dissociation Mass Spectrometry.
74. M. Sobczyk and J. Simons, *Int. J. Mass. Spectrom.*, **253**, 274–280 (2006). Distance Dependence of Through-Bond Electron Transfer Rates in Electron-Capture and Electron-Transfer Dissociation.
75. I. Anusiewicz, J. Berdys-Kochanska, and J. Simons, *J. Phys. Chem. A*, **109**, 5801–5813 (2005). Electron Attachment Step in Electron Capture Dissociation (ECD) and Electron Transfer Dissociation (ETD).

76. I. Anusiewicz, J. Berdys-Kochanska, P. Skurski, and J. Simons, *J. Phys. Chem. A*, **110**, 1261–1266 (2006). Simulating Electron Transfer Attachment to a Positively Charged Model Peptide.
77. M. Sobczyk and J. Simons, *J. Phys. Chem. B*, **110**, 7519–7527 (2006). The Role of Excited Rydberg States in Electron Transfer Dissociation.
78. D. Neff and J. Simons, *J. Phys. Chem. A*, **114**, 1309–1323 (2010). Analytical and Computational Studies of Intramolecular Electron Transfer Pertinent to Electron Transfer and Electron Capture Dissociation Mass Spectrometry.
79. B. Boudaffa, P. Cloutier, D. Hunting, M. A. Huels, and L. Sanche, *Science*, **287**, 1658–1661 (2000). Resonance Formation of DNA Strand Breaks by Low-Energy (3 to 20 eV) Electrons.
80. Y. Zheng, P. Cloutier, D. J. Hunting, L. Sanche, and J. R. Wagner, *J. Am. Chem. Soc.*, **127**, 16592–16598 (2005). Chemical Basis of DNA Sugar–Phosphate Cleavage by Low-Energy Electrons.
81. L. Sanche, in *Radical and Radical Ion Reactivity in Nucleic Acid Chemistry*, M. M. Greenberg (Ed.), Wiley, 2010, pp. 239–293, Low Energy Electron Interaction with DNA: Bond Dissociation and Formation of Transient Anions, Radicals, and Radical Anions.
82. J. Simons, *Acc. Chem. Res.*, **39**, 772–779 (2006). How Do Low-Energy (0.1–2 eV) Electrons Cause DNA Strand Breaks?
83. I. Bald, J. Langer, P. Tegeder, and O. Ingólfsson, *Int. J. Mass Spectrom.*, **277**, 4–25 (2008). From Isolated Molecules through Clusters and Condensates to the Building Blocks of Life.
84. G. V. Buxton, in *Charged Particles and Phonon Interactions with Matter*, A. Mozumder and Y. Hatano (Eds.), Marcel Dekker, New York, 2004; chapter 12, pp. 331–364, The Radiation Chemistry of Liquid Water.
85. S. Ptasinkska, S. Denifl, P. Scheier, E. Illenberger, and T. D. Märk, *Angew. Chem. Int. Ed. Engl.*, **44**, 6941–6943 (2005). Bond- and Site-Selective Loss of H Atoms from Nucleobases by Very-Low-Energy Electrons (<3 eV).
86. A. M. Scheer, C. Silvernail, J. A. Belot, K. Aflatooni, G. A. Gallup, and P. D. Burrow, *Chem. Phys. Lett.*, **411**, 46–50 (2005). Dissociative Electron Attachment to Uracil Deuterated at the N_1 and N_3 Positions.
87. S. Ptasinkska, S. Denifl, P. Scheier, and T. D. Märk, *J. Chem. Phys.*, **120**, 8505–8511 (2004). Inelastic Electron Interaction (Attachment Ionization) with Deoxyribose.
88. P. D. Burrow, *J. Chem. Phys.*, **122**, 087105:1–2 (2005). Comment on "Radiation Damage of Biosystems Mediated by Secondary Electrons: Resonant Precursors for Uracil Molecules" [J. Chem. Phys. 120, 7446 (2004)].
89. F. A. Gianturco, F. Sebastianelli, R. R. Lucchese, I. Baccarelli, and N. Sanna, *J. Chem. Phys.*, **128**, 174302:1–8 (2008). Ring-Breaking Electron Attachment to Uracil: Following Bond Dissociations via Evolving Resonances.
90. J. Gu, J. Wang, and J. Leszczynski, *Nucleic Acids Res.*, **38**, 5280–5290 (2010). Electron Attachment-Induced DNA Single-Strand Breaks at the Pyrimidine Sites.
91. E. J. Hart and M. Anbar, *The Hydrated Electron*, Wiley, New York, 1970.
92. J. Peon, G. C. Hess, J.-M. L. Pecourt, T. Yuzawa, and B. Kohler, *J. Phys. Chem. A*, **103**, 2460–2466 (1999). Ultrafast Photoionization Dynamics of Indole in Water.
93. N. I. Hammer, J. W. Shin, J. M. Headrick, E. G. Diken, J. R. Roscioli, G. H. Weddle, and M. A. Johnson, *Science*, **306**, 675–679 (2004). How Do Small Water Clusters Bind an Excess Electron?
94. O. T. Ehrler and D. M. Neumark, *Acc. Chem. Res.*, **42**, 769–777 (2009). Dynamics of Electron Solvation in Molecular Clusters.
95. L. D. Jacobson and J. M. Herbert, *J. Am. Chem. Soc.*, **133**, 19889–19899 (2011). Theoretical Characterization of Four Distinct Isomer Types in Hydrated-Electron Clusters, and Proposed Assignments for Photoelectron Spectra of Water Cluster Anions.

96. W. C. Martin, A. Musgrove, S. Kotochigova, and J. E. Sansonetti. Technical report, National Institute of Standards and Technology, Gaithersburg, MD, 2013. Ground Levels and Ionization Energies for the Neutral Atoms.
97. B. J. Lynch, Y. Zhao, and D. G. Truhlar, *J. Phys. Chem. A*, **107**, 1384–1388 (2003). Effectiveness of Diffuse Basis Functions for Calculating Relative Energies by Density Functional Theory.
98. J. Simons, *Collect. Czech. Chem. C.*, **70**, 579–604 (2005). Equations of Motion Theory for Electron Affinities.
99. J. Simons, *Adv. Quantum Chem.*, **50**, 213–233 (2005). Response of a Molecule to Adding or Removing an Electron.
100. D. Danovich, *WIREs Comput. Mol. Sci.*, **1**, 377–387 (2011). Green's Function Methods for Calculating Ionization Potentials, Electron Affinities, and Excitation Energies.
101. J. V. Ortiz, in *Computational Chemistry: Reviews of Current Trends*, J. Leszczynski (Ed.) Vol. 2, World Scientific, Singapore, 1997, pp. 1–61, The Electron Propagator Picture of Molecular Electronic Structure.
102. R. Flores-Moreno and J. V. Ortiz, in *Practical Aspects of Computational Chemistry*, J. Leszczynski and M. K. Shukla (Eds.), Springer, 2009, chapter 1, pp. 1–17, Efficient and Accurate Electron Propagator Methods and Algorithms.
103. R. Flores-Moreno, J. Melin, O. Dolgounitcheva, V. G. Zakrezewski, and J. V. Ortiz, *Int. J. Quantum Chem.*, **110**, 706–715 (2010). Three Approximations to the Nonlocal and Energy-Dependent Correlation Potential in Electron Propagator Theory.
104. J. V. Ortiz, *WIREs Comput. Mol. Sci.*, **3**, 123–142 (2013). Electron Propagator Theory: An Approach to Prediction and Interpretation in Quantum Chemistry.
105. J. M. Herbert and M. Head-Gordon, *Proc. Natl. Acad. Sci. U.S.A.*, **103**, 14282–14287 (2006). First-Principles, Quantum-Mechanical Simulations of Electron Solvation by a Water Cluster.
106. J. Simons, P. Skurski, and R. Barrios, *J. Am. Chem. Soc.*, **122**, 11893–11899 (2000). Repulsive Coulomb Barriers in Compact Stable and Metastable Multiply Charged Anions.
107. T. P. Hezel, C. E. Burkhardt, M. Ciocca, L.-W. He, and J. J. Leventhal, *Am. J. Phys.*, **60**, 329–335 (1992). Classical View of the Properties of Rydberg Atoms: Application of the Correspondence Principle.
108. R. F. Wallis, R. Herman, and H. W. Milnes, *J. Mol. Spectrosc.*, **4**, 51–74 (1960). Energy Levels of an Electron in the Field of a Finite Dipole.
109. O. H. Crawford, *Proc. Phys. Soc. London*, **91**, 279–284 (1967). Bound States of a Charged Particle in a Dipole Field.
110. W. R. Garrett, *Chem. Phys. Lett.*, **5**, 393–397 (1970). Critical Binding of an Electron to a Non-Stationary Electric Dipole.
111. W. R. Garrett, *Phys. Rev. A*, **3**, 961–972 (1971). Critical Binding of an Electron to a Rotationally Excited Dipolar System.
112. O. H. Crawford and W. R. Garrett, *J. Chem. Phys.*, **66**, 4968–4970 (1977). Electron Affinities of Polar Molecules.
113. M. Gutowski, P. Skurski, A. I. Boldyrev, J. Simons, and K. D. Jordan, *Phys. Rev. A*, **54**, 1906–1909 (1996). Contribution of Electron Correlation to the Stability of Dipole-Bound Anionic States.
114. C. Desfrançois, H. Abdoul-Carime, N. Khelifa, and J. P. Schermann, *Phys. Rev. Lett.*, **73**, 2436–2439 (1994). From $1/r$ to $1/r^2$ Potentials: Electron Exchange between Rydberg Atoms and Polar Molecules.
115. M. Gutowski and P. Skurski, *Chem. Phys. Lett.*, **303**, 65–75 (1999). Theoretical Study of the Quadrupole-Bound Anion $(BeO)_2^-$.
116. H.-Y. Chen and W.-S. Sheu, *J. Chem. Phys.*, **110**, 9032–9038 (1999). Dipole-Bound Anion of Water Dimer: Theoretical *ab-Initio* Study.

117. J. V. Coe, G. H. Lee, J. G. Eaton, S. T. Arnold, H. W. Sarkas, K. H. Bowen, C. Ludewigt, H. Haberland, and D. R. Worsnop, *J. Chem. Phys.*, **92**, 3960–3962 (1990). Photoelectron Spectroscopy of Hydrated Electron Cluster Anions, $(H_2O)^-_{n=2-69}$.

118. G. H. Lee, S. T. Arnold, J. G. Eaton, H. W. Sarkas, K. H. Bowen, C. Ludewigt, and H. Haberland, *Z. Phys. D*, **20**, 9–12 (1991). Negative Ion Photoelectron Spectroscopy of Solvated Electron Cluster Anions, Water $(H_2O)^-_n$ and Ammonia $(NH_3)^-_n$.

119. J. Kim, S. B. Suh, and K. S. Kim, *J. Chem. Phys.*, **111**, 10077–10087 (1999). Water Dimer to Pentamer with an Excess Electron: *Ab Initio* Study.

120. C. Desfrançois, V. Periquet, Y. Bouteiller, and J. P. Schermann, *J. Phys. Chem. A*, **102**, 1274–1278 (1998). Valence and Dipole Binding of Electrons to Uracil.

121. O. Dolgounitcheva, V. G. Zakrzewski, and J. V. Ortiz, *Chem. Phys. Lett.*, **307**, 220–226 (1999). Structures and Electron Detachment Energies of Uracil Anions.

122. J. H. Hendricks, S. A. Lyapustina, H. L. de Clercq, and K. H. Bowen, *J. Chem. Phys.*, **108**, 8–11 (1998). The Dipole Bound-to-Covalent Anion Transformation in Uracil.

123. R. A. Bachorz, J. Rak, and M. Gutowski, *Phys. Chem. Chem. Phys.*, **7**, 2116–2125 (2005). Stabilization of Very Rare Tautomers of Uracil by an Excess Electron.

124. A. M. Scheer, K. Aflatooni, G. A. Gallup, and P. D. Burrow, *Phys. Rev. Lett.*, **92**, 068102:1–4 (2004). Bond Breaking and Temporary Anion States in Uracil and Halouracils: Implications for the DNA Bases.

125. P. D. Burrow, G. A. Gallup, A. M. Scheer, S. Denifl, S. Ptasinkska, T. Märk, and P. Scheier, *J. Chem. Phys.*, **124**, 124310:1–7 (2006). Vibrational Feshbach Resonances in Uracil and Thymine.

126. F. Wang and K. D. Jordan, *J. Chem. Phys.*, **119**, 11645–11653 (2003). Parallel-Tempering Monte Carlo Simulations of the Finite-Temperature Behavior of $(H_2O)^-_6$.

127. T. Sommerfeld and K. D. Jordan, *J. Phys. Chem. A*, **109**, 11531–11538 (2005). Quantum Drude Oscillator Model for Describing the Interaction of Excess Electrons with Water Clusters: An Application to $(H_2O)^-_{13}$.

128. T. Sommerfeld, S. D. Gardner, A. DeFusco, and K. D. Jordan, *J. Chem. Phys.*, **125**, 174301:1–7 (2006). Low-Lying Isomers and Finite Temperature Behavior of $(H_2O)^-_6$.

129. A. DeFusco, T. Sommerfeld, and K. D. Jordan, *Chem. Phys. Lett.*, **455**, 135–138 (2008). Parallel Tempering Monte Carlo Simulations of the Water Heptamer Anion.

130. R. A. Bachorz, W. Klopper, M. Gutowski, X. Li, and K. H. Bowen, *J. Chem. Phys.*, **129**, 054309:1–10 (2008). Photoelectron Spectrum of Valence Anions of Uracil and First-Principles Calculations of Excess Electron Binding Energies.

131. T. Waters, X.-B. Wang, and L.-S. Wang, *Coordin. Chem. Rev.*, **251**, 474–491 (2007). Electrospray Ionization Photoelectron Spectroscopy: Probing the Electronic Structure of Inorganic Metal Complexes in the Gas-Phase.

132. X.-B. Wang and L.-S. Wang, *Annu. Rev. Phys. Chem.*, **60**, 105–126 (2009). Photoelectron Spectroscopy of Multiply Charged Anions.

133. X.-B. Wang, C.-F. Ding, and L.-S. Wang, *Phys. Rev. Lett.*, **81**, 3351–3354 (1998). Photodetachment Spectroscopy of a Doubly Charged Anion: Direct Observation of the Repulsive Coulomb Barrier.

134. L.-S. Wang, C.-F. Ding, X.-B. Wang, and J. B. Nicholas, *Phys. Rev. Lett.*, **81**, 2667–2670 (1998). Probing the Potential Barriers and Intramolecular Electrostatic Interactions in Free Doubly Charged Anions.

135. C.-F. Ding, X.-B. Wang, and L.-S. Wang, *J. Phys. Chem. A*, **102**, 8633–8636 (1998). Photoelectron Spectroscopy of Doubly Charged Anions: Intramolecular Coulomb Repulsion and Solvent Stabilization.

136. E. Pluharřová, M. Ončák, R. Seidel, C. Schroeder, W. Schroeder, B. Winter, S. E. Bradforth, P. Jungwirth, and P. Slavček, *J. Phys. Chem. B*, **116**, 13254–13264 (2012). Transforming Anion Instability into Stability: Contrasting Photoionization of Three Protonation Forms of the Phosphate Ion upon Moving into Water.

137. J. V. Coe, A. D. Earhart, M. H. Cohen, G. J. Hoffman, H. W. Sarkas, and K. H. Bowen, *J. Chem. Phys.*, **107**, 6023–6031 (1997). Using Cluster Studies to Approach the Electronic Structure of Bulk Water: Reassessing the Vacuum Level, Conduction Band Edge, and Band Gap of Water.

138. J. V. Coe, *Int. Rev. Phys. Chem.*, **20**, 33–58 (2001). Fundamental Properties of Bulk Water from Cluster Ion Data.

139. J. V. Coe, S. M. Williams, and K. H. Bowen, *Int. Rev. Phys. Chem.*, **27**, 27–51 (2008). Photoelectron Spectra of Hydrated Electron Clusters Vs. Cluster Size.

140. B. Winter and M. Faubel, *Chem. Rev.*, **106**, 1176–1211 (2006). Photoemission from Liquid Aqueous Solutions.

141. L. D. Jacobson and J. M. Herbert, *J. Chem. Phys.*, **133**, 154106:1–19 (2010). A One-Electron Model for the Aqueous Electron that Includes Many-Body Electron-Water Polarization: Bulk Equilibrium Structure, Vertical Electron Binding Energy, and Optical Absorption Spectrum.

142. L. Kevan, *Acc. Chem. Res.*, **14**, 138–145 (1981). Solvated Electron Structure in Glassy Matrices.

143. P. J. Rossky and J. Schnitker, *J. Phys. Chem.*, **92**, 4277–4285 (1988). The Hydrated Electron: Quantum Simulation of Structure, Spectroscopy, and Dynamics.

144. M. Boero, M. Parrinello, K. Terakura, T. Ikeshoji, and C. C. Liew, *Phys. Rev. Lett.*, **90**, 226403:1–4 (2003). First-Principles Molecular-Dynamics Simulations of a Hydrated Electron in Normal and Supercritical Water.

145. M. Boero, *J. Phys. Chem. A*, **111**, 12248–12256 (2007). Excess Electron in Water at Different Thermodynamic Conditions.

146. F. Uhlig, O. Marsalek, and P. Jungwirth, *J. Phys. Chem. Lett.*, **3**, 3071–3075 (2012). Unraveling the Complex Nature of the Hydrated Electron.

147. G. W. Robinson, P. J. Thistlewaite, and J. Lee, *J. Phys. Chem.*, **90**, 4224–4233 (1986). Molecular Aspects of Ionic Hydration Reactions.

148. H. F. Hameka, G. W. Robinson, and C. J. Marsden, *J. Phys. Chem.*, **91**, 3150–3157 (1987). Structure of the Hydrated Electron.

149. T. R.Tuttle, Jr. and S. Golden, *J. Phys. Chem.*, **95**, 5725–5736 (1991). Solvated Electrons: What is Solvated?

150. A. L. Sobolewski and W. Domcke, *Phys. Chem. Chem. Phys.*, **4**, 4–10 (2002). Hydrated Hydronium: A Cluster Model of the Solvated Electron?

151. A. L. Sobolewski and W. Domcke, *J. Phys. Chem. A*, **106**, 4158–4167 (2002). Ab Initio Investigation of the Structure and Spectroscopy of Hydronium–Water Clusters.

152. A. L. Sobolewski and W. Domcke, *Phys. Chem. Chem. Phys.*, **9**, 3818–3829 (2007). Computational Studies of Aqueous-Phase Photochemistry and the Hydrated Electron in Finite-Size Clusters.

153. S. Neumann, W. Eisfeld, A. Sobolewski, and W. Domcke, *Phys. Chem. Chem. Phys.*, **6**, 5297–5303 (2004). Simulation of the Resonance Raman Spectrum of the Hydrated Electron in the Hydrated-Hydronium Cluster Model.

154. R. E. Larsen, W. J. Glover, and B. J. Schwartz, *Science*, **329**, 65–69 (2010). Does the Hydrated Electron Occupy a Cavity?

155. B. Abel, U. Buck, A. L. Sobolewski, and W. Domcke, *Phys. Chem. Chem. Phys.*, **14**, 22–34 (2012). On the Nature and Signatures of the Solvated Electron in Water.

156. J. R. Casey, R. E. Larsen, and B. J. Schwartz, *Proc. Natl. Acad. Sci. U.S.A.*, **110**, 2712–2717 (2013). Resonance Raman and Temperature-Dependent Electronic Absorption Spectra of Cavity and Noncavity Models of the Hydrated Electron.

157. F. Muguet, M.-P. Bassez, and G. W. Robinson, *J. Phys. Chem.*, **92**, 7262–7263 (1988). Reply to the Comment "Aquated Electrons, H_2O^- Anions, and OH^- H_3O Units".

158. M. J. Tauber and R. A. Mathies, *J. Am. Chem. Soc.*, **125**, 1394–1402 (2003). Structure of the Aqueous Solvated Electron from Resonance Raman Spectroscopy: Lessons from Isotopic Mixtures.

159. L. Turi and A. Madarász, *Science*, **331**, 1387 (2011). Comment on "Does the Hydrated Electron Occupy a Cavity?".

160. L. D. Jacobson and J. M. Herbert, *Science*, **331**, 1387 (2011). Comment on "Does the Hydrated Electron Occupy a Cavity?".

161. R. E. Larsen, W. J. Glover, and B. J. Schwartz, *Science*, **331**, 1387 (2011). Response to Comment on "Does the Hydrated Electron Occupy a Cavity?".

162. J. M. Herbert and L. D. Jacobson, *J. Phys. Chem. A*, **115**, 14470–14483 (2011). Structure of the Aqueous Electron: Assessment of One-Electron Pseudopotential Models in Comparison to Experimental Data and Time-Dependent Density Functional Theory.

163. F. Uhlig, J. M. Herbert, M. P. Coons, and P. Jungwirth, *J. Phys. Chem. A*, **118**, 7507–7515 (2014). Optical Spectroscopy of the Bulk and Interfacial Hydrated Electron from ab Initio Calculations.

164. D. M. Neumark, *Mol. Phys.*, **106**, 2183–2197 (2008). Spectroscopy and Dynamics of Excess Electrons in Clusters.

165. A. Kammrath, J. R. R. Verlet, G. B. Griffin, and D. M. Neumark, *J. Chem. Phys.*, **125**, 076101:1–2 (2006). Photoelectron Spectroscopy of Large $(\text{Water})_n^-$ ($n = 50$–200) Clusters at 4.7 eV.

166. M. Mitsui, N. Ando, S. Kokubo, A. Nakajima, and K. Kaya, *Phys. Rev. Lett.*, **91**, 153002:1–4 (2003). Coexistence of Solvated Electrons and Solvent Valence Anions in Negatively Charged Acetonitrile Clusters, $(CH_3CN)_n^-$ ($n = 10$–100).

167. R. N. Barnett, U. Landman, C. L. Cleveland, and J. Jortner, *J. Chem. Phys.*, **88**, 4429–4447 (1988). Electron Localization in Water Clusters. II. Surface and Internal States.

168. J. Jortner, U. Landman, and R. N. Barnett, *Chem. Phys. Lett.*, **152**, 353–357 (1988). Optical Absorption Spectra of $(H_2O)_n^-$.

169. R. N. Barnett, U. Landman, G. Makov, and A. Nitzan, *J. Chem. Phys.*, **93**, 6226–6238 (1990). Theoretical Studies of the Spectroscopy of Excess Electrons in Water Clusters.

170. G. Makov and A. Nitzan, *J. Phys. Chem.*, **98**, 3459–3466 (1994). Solvation and Ionization near a Dielectric Surface.

171. S. E. Braslavsky, *Pure Appl. Chem.*, **79**, 292–465 (2007). Glossary of Terms Used in Photochemistry, 3rd Edition (IUPAC Recommendations 2006).

172. C. J. Cramer and D. G. Truhlar, *Chem. Rev.*, **99**, 2161–2200 (1999). Implicit Solvation Models: Equilibria, Structure, Spectra, and Dynamics.

173. L. Turi, W.-S. Sheu, and P. J. Rossky, *Science*, **309**, 914–917 (2005). Characterization of Excess Electrons in Water-Cluster Anions by Quantum Simulations.

174. J. R. R. Verlet, A. E. Bragg, A. Kammrath, O. Cheshnovsky, and D. M. Neumark, *Science*, **310**, 1769–1769 (2005). Comment on "Characterization of Excess Electrons in Water-Cluster Anions by Quantum Simulations".

175. L. Turi, W.-S. Sheu, and P. J. Rossky, *Science*, **310**, 1769–1769 (2005). Response to Comment on "Characterization of Excess Electrons in Water-Cluster Anions by Quantum Simulations".

176. J. R. Roscioli, N. I. Hammer, and M. A. Johnson, *J. Phys. Chem. A*, **110**, 7517–7520 (2006). Infrared Spectroscopy of Water Cluster Anions $(H_2O)_{n=3-24}^-$ in the HOH Bending Region: Persistence of the Double H-Bond Acceptor (AA) Water Molecule in the Excess Electron Binding Site of the Class I Isomers.

177. K. R. Asmis, G. Santabrogio, J. Zhou, E. Garand, J. Headrick, D. Goebbert, M. A. Johnson, and D. M. Neumark, *J. Chem. Phys.*, **126**, 191105, 1–5 (2007). Vibrational Spectroscopy of Hydrated Electron Clusters $(H_2O)_{15-50}^-$ via Infrared Multiple Photon Dissociation.

178. T. Maeyama, K. Yoshida, and A. Fujii, *J. Phys. Chem. A*, **116**, 3771–3780 (2012). Size-Dependent Metamorphosis of Electron Binding Motif in Cluster Anions of Primary Amide Molecules.

179. C. Cohen-Tannoudji, B. Diu, and F. Laloë, *Quantum Mechanics*, Vols. I and II, Wiley, New York, 1977.

180. H. Yamamoto, *Appl. Phys. A*, **42**, 245–248 (1987). Resonant Tunneling Condition and Transmission Coefficient in a Symmetrical One-Dimensional Rectangular Double-Barrier System.

181. H. Xu, Y. Wang, and G. Chen, *Phys. Stat. Sol. B*, **171**, K9–K12 (1992). Shape of the Transmission Spectrum in Rectangular Double-Barrier Structures.

182. S. Klaiman and I. Gilary, *Adv. Quantum Chem.*, **63**, 1–31 (2012). Chapter 1 – On Resonance: A First Glance in the Behavior of Unstable States.

183. J. Simons, in *Resonances in Electron-Molecule Scattering, van der Waals Complexes, and Reactive Chemical Dynamics*, D. Truhlar (Ed.), Vol. 263 of, *ACS Symposium Series*, American Chemical Society, 1984; chapter 1, pp. 3–16, Roles Played by Metastable States in Chemistry.

184. K. D. Jordan and P. D. Burrow, in *Photon, Electron, and Ion Probes of Polymer Structure and Properties*, *ACS Symposium Series* Vol. 162, American Chemical Society, 1981; chapter 1, pp. 1–10, Resonant Electron Scattering and Anion States in Polyatomic Molecules.

185. K. D. Jordan and P. D. Burrow, *Chem. Rev.*, **87**, 557–588 (1987). Temporary Anion States of Polyatomic Hydrocarbons.

186. R. Balog, J. Langer, S. Gohlke, M. Stano, H. Abdoul-Carime, and E. Illenberger, *Int. J. Mass Spectrom.*, **233**, 267–291 (2004). Low Energy Electron Driven Reactions in Free and Bound Molecules: From Unimolecular Processes in the Gas Phase to Complex Reactions in a Condensed Environment.

187. K. B. Bravaya, D. Zuev, E. Epifanovsky, and A. I. Krylov, *J. Chem. Phys.*, **138**, 124106:1–15 (2013). Complex-Scaled Equation-of-Motion Coupled-Cluster Method with Single and Double Substitutions for Autoionizing Excited States: Theory, Implementation, and Examples.

188. D. Zuev, K. B. Bravaya, T. D. Crawford, R. Lindh, and A. I. Krylov, *J. Chem. Phys.*, **134**, 034310:1–13 (2011). Electronic Structure of the Two Isomers of the Anionic Form of *p*-Coumaric Acid Chromophore.

189. T. Clark, J. Chandrasekhar, G. W. Spitznagel, and P. v. R. Schleyer, *J. Comput. Chem.*, **4**, 294–301 (1983). Efficient Diffuse Function-Augmented Basis Sets for Anion Calculations. III. The 3-21+G Basis Set for First-Row Elements, Li–F.

190. R. A. Kendall, T. H. Dunning, Jr. and R. J. Harrison, *J. Chem. Phys.*, **96**, 6796–6806 (1992). Electron Affinities of the First-Row Atoms Revisited. Systematic Basis Sets and Wave Functions.

191. J. M. Herbert and M. Head-Gordon, *J. Phys. Chem. A*, **109**, 5217–5229 (2005). Calculation of Electron Detachment Energies for Water Cluster Anions: An Appraisal of Electronic Structure Methods, with Application to $(H_2O)_{20}^-$ and $(H_2O)_{24}^-$.

192. P. Skurski, M. Gutowski, and J. Simons, *Int. J. Quantum Chem.*, **80**, 1024 (2000). How to Choose a One-Electron Basis Set to Reliably Describe a Dipole-Bound Anion.

193. T. J. Lee and H. F. Schaefer, III, *J. Chem. Phys.*, **83**, 1784–1794 (1985). Systematic Study of Molecular Anions within the Self-Consistent-Field Approximation: OH^-, CN^-, C_2H^-, NH_2^-, and CH_3^-.

194. A. I. Krylov and P. M. W. Gill, *WIREs Comput. Mol. Sci.*, **3**, 317–326 (2013). Q-Chem: An Engine for Innovation.

195. http://www.q-chem.com

196. J. Katriel and E. R. Davidson, *Proc. Natl. Acad. Sci. U.S.A.*, **77**, 4403–4406 (1980). Asymptotic Behavior of Atomic and Molecular Wave Functions.

197. J. P. Perdew, R. G. Parr, M. Levy, and J. L.Balduz, Jr., *Phys. Rev. Lett.*, **49**, 1691–1694 (1982). Density-Functional Theory for Fractional Particle Number: Derivative Discontinuities of the Energy.

198. N. C. Handy, M. T. Marron, and H. J. Silverstone, *Phys. Rev.*, **180**, 45–48 (1969). Long-Range Behavior of Hartree-Fock Orbitals.

199. K. H. Bowen and J. G. Eaton, in *The Structure of Small Molecules and Ions*, R. Naaman and Z. Vager (Eds.), Plenum, New York, 1989, pp. 147–169, Photodetachment Spectroscopy of Negative Cluster Ions.

200. S. T. Arnold, J. G. Eaton, D. Patel-Misra, H. W. Sarkas, and K. H. Bowen, in *Ion and Cluster Ion Spectroscopy and Structure*, J. P. Maier (Ed.), Elsevier, Amsterdam, 1989, pp. 417–472, Continuous Beam Photoelectron Spectroscopy of Cluster Anions.

201. Y. Bouteiller, C. Desfrançois, H. Abdoul-Carime, and J. P. Schermann, *J. Chem. Phys.*, **105**, 6420–6425 (1996). Structure and Intermolecular Motions of the Water Dimer Anions.

202. K. Yagi, Y. Okano, T. Sato, Y. Kawashima, T. Tsuneda, and K. Hirao, *J. Phys. Chem. A*, **112**, 9845–9853 (2008). Water Cluster Anions Studied by Long-Range Corrected Density Functional Theory.

203. M. Gutowski and P. Skurski, *J. Chem. Phys.*, **107**, 2968–2973 (1997). Theoretical Study of the Dipole-Bound Anion $(HF)_2^-$.

204. M. Gutowski and P. Skurski, *J. Phys. Chem. B*, **101**, 9143–9146 (1997). Dispersion Stabilization of Solvated Electrons and Dipole-Bound Anions.

205. M. Gutowski, K. D. Jordan, and P. Skurski, *J. Phys. Chem. A*, **102**, 2624–2633 (1998). Electronic Structure of Dipole-Bound Anions.

206. C. F. Williams and J. M. Herbert, *J. Phys. Chem. A*, **112**, 6171–6178 (2008). Influence of Structure on Electron Correlation Effects and Electron–Water Dispersion Interactions in Anionic Water Clusters.

207. T. Clark and G. Illing, *J. Am. Chem. Soc.*, **109**, 1013–1020 (1987). Ab Initio Localized Electron Calculations on Solvated Electron Structures.

208. H. Tachikawa and M. Ogasawura, *J. Phys. Chem.*, **94**, 1746–1750 (1990). Ab Initio Molecular Orbital Study on Water Dimer Anions.

209. H. Tachikawa, *Chem. Phys. Lett.*, **370**, 188–196 (2003). Electron Capture Dynamics of the Water Dimer: A Direct ab Initio Dynamics Study.

210. H. Tachikawa, *J. Chem. Phys.*, **125**, 144307, 1–8 (2006). Electron Hydration Dynamics in Water Clusters: A Direct *ab Initio* Molecular Dynamics Approach.

211. J. Kim, J. Y. Lee, K. S. Oh, J. M. Park, S. Lee, and K. S. Kim, *Phys. Rev. A*, **59**, R930–R933 (1999). Quantum-Mechanical Probabilistic Structure of the Water Dimer with an Excess Electron.

212. L. D. Jacobson and J. M. Herbert, *J. Am. Chem. Soc.*, **132**, 10000–10002 (2010). Polarization-Bound Quasi-Continuum States are Responsible for the "Blue Tail" in the Optical Absorption Spectrum of the Aqueous Electron.

213. R. L. Martin, *J. Chem. Phys.*, **118**, 4775–4777 (2003). Natural Transition Orbitals.

214. J. S. Townsend, *Modern Approach to Quantum Mechanics*, University Science Books, Sausalito, CA, 2000.

215. A. Dreuw and M. Head-Gordon, *Chem. Rev.*, **105**, 4009–4037 (2005). Single-Reference ab Initio Methods for the Calculation of Excited States of Large Molecules.

216. J. VandeVondele and J. Hutter, *J. Chem. Phys.*, **127**, 114105:1–9 (2007). Gaussian Basis Sets for Accurate Calculations on Molecular Systems in Gas and Condensed Phases.

217. O. Marsalek, F. Uhlig, J. VandeVondele, and P. Jungwirth, *Acc. Chem. Res.*, **45**, 23–32 (2012). Structure, Dynamics, and Reactivity of Hydrated Electrons by ab Initio Molecular Dynamics.

218. O. Marsalek, F. Uhlig, and P. Jungwirth, *J. Phys. Chem. C*, **114**, 20489–20495 (2010). Electrons in Cold Water Clusters: An ab Initio Molecular Dynamics Study of Localization and Metastable States.

219. S. Ronen, *Phys. Rev. A*, **68**, 012106:1–7 (2003). Electron Structure of a Dipole-Bound Anion Confined in a Spherical Box.

220. J. M. Herbert and M. Head-Gordon, *J. Am. Chem. Soc.*, **128**, 13932–13939 (2006). Charge Penetration and the Origin of Large O–H Vibrational Red-Shifts in Hydrated-Electron Clusters, $(H_2O)_n^-$.

221. http://www.iqmol.org, xxxx.

222. G. Schaftenaar and J. H. Noordik, *J. Comput.-Aided Mol. Design*, **14**, 123–134 (2000). Molden: A Pre- and Post-Processing Program for Molecular and Electronic Structures.

223. B. M. Bode and M. S. Gordon, *J. Mol. Graphics Mod.*, **16**, 133–138 (1998). MacMolPlt: A Graphical User Interface for GAMESS.

224. W. Humphrey, A. Dalke, and K. Schulten, *J. Molec. Graphics*, **14**, 33–38 (1996). VMD – Visual Molecular dynamics.

225. C. B. Hübschle and P. Luger, *J. Appl. Crystallogr.*, **39**, 901–904 (2006). MolIso – A Program for Colour-Mapped Iso-Surfaces.

226. C. B. Hübschle and B. Dittrich, *J. Appl. Crystallogr.*, **44**, 238–240 (2011). MoleCoolQt – A Molecule Viewer for Charge-Density Research.

227. S. N. Eustis, D. Radisic, K. H. Bowen, R. A. Bachorz, M. Haranczyk, G. K. Schenter, and M. Gutowski, *Science*, **319**, 936–939 (2008). Electron-Driven Acid–Base Chemistry: Proton Transfer from Hydrogen Chloride to Ammonia.

228. M. Haranczyk and M. Gutowski, *J. Chem. Theory Comput.*, **4**, 689–693 (2008). Visualization of Molecular Orbitals and the Related Electron Densities.

229. A. Rauk and D. A. Armstrong, *Int. J. Quantum Chem.*, **95**, 683–696 (2003). Potential Energy Barriers for Dissociative Attachment to HF.HF and HCl.HCl: Ab Initio Study.

230. http://www.gaussian.com/g_tech/g_ur/u_cubegen.htm

231. K. Momma and F. Izumi, *J. Appl. Crystallogr.*, **41**, 653–658 (2008). VESTA: A Three-Dimensional Visualization System for Electronic and Structural Analysis.

232. M. D. Sevilla, B. Besler, and A.-O. Colson, *J. Phys. Chem.*, **99**, 1060–1063 (1995). Ab Initio Molecular Orbital Calculations of DNA Radical Ions. 5. Scaling of Calculated Electron Affinities and Ionization Potentials to Experimental Values.

233. P. D. Burrow, A. E. Howard, A. R. Johnston, and K. D. Jordan, *J. Phys. Chem.*, **96**, 7570–7578 (1992). Temporary Anion States of Hydrogen Cyanide, Methyl Cyanide, and Methylene Dicyanide, Selected Cyanoethylenes, Benzonitrile, and Tetracyanoquinodimethane.

234. M. Gutowski and P. Skurski, *Recent Res. Dev. Phys. Chem.*, **3**, 245–260 (1999). Electronic Structure of Dipole-Bound Anions.

235. K. A. Peterson and T. H.Dunning, Jr., *J. Mol. Struct. (THEOCHEM)*, **400**, 93–117 (1997). The CO Molecule: The Role of Basis Set and Correlation Treatment in the Calculation of Molecular Properties.

236. R. K. Nesbet, *J. Chem. Phys.*, **40**, 3619–3633 (1964). Electronic Structure of N_2, CO, and BF.

237. K. Raghavachari, G. W. Trucks, J. A. Pople, and M. Head-Gordon, *Chem. Phys. Lett.*, **157**, 479–483 (1989). A Fifth-Order Perturbation Comparison of Electron Correlation Theories.

238. T. Helgaker, P. Jørgensen, and J. Olsen, *Molecular Electronic-Structure Theory*, Wiley, New York, 2000.

239. G. de Oliveira, J. M. L. Martin, F. de Proft, and P. Geerlings, *Phys. Rev. A*, **60**, 1034–1045 (1999). Electron Affinities of the First- and Second-Row Atoms: Benchmark *Ab Initio* and Density-Functional Calculations.

240. N. B. Balabanov and K. A. Peterson, *J. Chem. Phys.*, **125**, 074110:1–10 (2006). Basis Set Limit Electronic Excitation Energies, Ionization Potentials, and Electron Affinities for the 3*d* Transition Metal Atoms: Coupled Cluster and Multireference Methods.

241. J. M. L. Martin and G. de Oliveira, *J. Chem. Phys.*, **111**, 1843–1866 (1999). Towards Standard Methods for Benchmark Quality *ab Initio* Thermochemistry – W1 and W2 Theory.

242. S. Parthiban and J. M. L. Martin, *J. Chem. Phys.*, **114**, 6014–6029 (2001). Assessment of W1 and W2 Theories for the Computation of Electron Affinities, Ionization Potentials, Heats of Formation, and Proton Affinities.

243. L. A. Curtiss, K. Raghavachari, P. C. Redfern, V. Rassolov, and J. A. Pople, *J. Chem. Phys.*, **109**, 7764–7776 (1998). Gaussian-3 (G3) Theory for Molecules Containing First and Second-Row Atoms.

244. L. A. Curtiss, P. C. Redfern, K. Raghavachari, V. Rassolov, and J. A. Pople, *J. Chem. Phys.*, **110**, 4703–4709 (1999). Gaussian-3 Theory Using Reduced Møller-Plesset Order.

245. L. A. Curtiss and K. Raghavachari, *Theor. Chem. Acc.*, **108**, 61–70 (2002). Gaussian-3 and Related Methods for Accurate Thermochemistry.

246. J. A. Montgomery, M. J. Frisch, J. W. Ochterski, and G. A. Petersson, *J. Chem. Phys.*, **112**, 6532–6542 (2000). A Complete Basis Set Model Chemistry. VII. Use of the Minimum Population Localization Method.

247. J. A. Montgomery, J. W. Ochterski, and G. A. Petersson, *J. Chem. Phys.*, **101**, 5900–5909 (1994). A Complete Basis Set Model Chemistry. IV. An Improved Atomic Pair Natural Orbital Method.

248. J. W. Ochterski, G. A. Petersson, and J. A. Montgomery, *J. Chem. Phys.*, **104**, 2598–2619 (1996). A Complete Basis Set Model Chemistry. V. Extensions to Six or More Heavy Atoms.

249. J. A. Montgomery, M. J. Frisch, J. W. Ochterski, and G. A. Petersson, *J. Chem. Phys.*, **110**, 2822–2827 (1999). A Complete Basis Set Model Chemistry. VI. Use of Density Functional Geometries and Frequencies.

250. J. M. L. Martin and S. Parthiban, in *Quantum-Mechanical Prediction of Thermochemical Data*, J. Cioslowski (Ed.) Vol. 22 of, *Understanding Chemical Reactivity*, Kluwer Academic Publishers, 2001; chapter 2, pp. 31–66, W1 and W2 Theories, and Their Variants: Thermochemistry in the kJ/mol Accuracy Range.

251. K. Raghavachari and L. A. Curtiss, in *Quantum-Mechanical Prediction of Thermochemical Data*, J. Cioslowski (Ed.) Vol. 22 of, *Understanding Chemical Reactivity*, Kluwer Academic Publishers, 2001; chapter 3, pp. 67–98, Complete Basis Set Models for Chemical Reactivity: From the Helium Atom to Enzyme Kinetics.

252. L. A. Curtiss, K. Raghavachari, G. W. Trucks, and J. A. Pople, *J. Chem. Phys.*, **94**, 7221–7230 (1991). Gaussian-2 Theory for Molecular Energies of First- and Second-Row Compounds.

253. H. Haberland, C. Ludewigt, H. Schindler, and D. R. Worsnop, *Z. Phys. A*, **320**, 151–153 (1985). Field Detachment of the Negatively Charged Water Dimer.

254. H. Haberland, C. Ludewigt, H.-G. Schindler, and D. R. Worsnop, *Phys. Rev. A*, **36**, 967–970 (1987). Field Detachment of $(H_2O)_2^-$ Clustered with Rare Gases.

255. J. H. Hendricks, H. L. de Clercq, S. A. Lyapustina, and K. H.Bowen, Jr., *J. Chem. Phys.*, **107**, 2962–2967 (1997). Negative Ion Photoelectron Spectroscopy of the Ground State, Dipole-Bound Dimeric Anion, $(HF)_2^-$.

256. P. Skurski, M. Gutowski, and J. Simons, *J. Chem. Phys.*, **114**, 7443–7449 (2001). *Ab Initio* Electronic Structure of HCN^- and HNC^- Dipole-Bound Anions and a Description of Electron Loss upon Tautomerization.

257. K. A. Peterson and M. Gutowski, *J. Chem. Phys.*, **116**, 3297–3299 (2002). Electron Binding Energies of Dipole-Bound Anions at the Coupled Cluster Level with Single, Double, and Triple Excitations: HCN^- and HNC^-.

258. T. Sommerfeld, A. DeFusco, and K. D. Jordan, *J. Phys. Chem. A*, **112**, 11021–11035 (2008). Model Potential Approaches for Describing the Interaction of Excess Electrons with Water Clusters: Incorporation of Long-Range Correlation Effects.

259. J. Xu and K. D. Jordan, *J. Phys. Chem. A*, **114**, 1364–1366 (2010). Application of the Diffusion Monte Carlo Method to the Binding of Excess Electrons to Water Clusters.

260. V. P. Vysotskiy, L. S. Cederbaum, T. Sommerfeld, V. K. Voora, and K. D. Jordan, *J. Chem. Theory Comput.*, **8**, 893–900 (2012). Benchmark Calculations of the Energies for Binding Excess Electrons to Water Clusters.

261. R. J. Bartlett and M. Musial, *Rev. Mod. Phys.*, **79**, 291–352 (2007). Coupled-Cluster Theory in Quantum Chemistry.

262. M. Nooijen and R. J. Bartlett, *J. Chem. Phys.*, **102**, 3629–3647 (1995). Equation of Motion Coupled Cluster Method for Electron Attachment.

263. J. F. Stanton and R. J. Bartlett, *J. Chem. Phys.*, **98**, 7029–7039 (1993). The Equation of Motion Coupled-Cluster Method. A Systematic Biorthogonal Approach to Molecular Excitation Energies, Transition Probabilities, and Excited State Properties.

264. V. G. Zakrezewski, O. Dolgounitcheva, A. V. Zakjevskii, and J. V. Ortiz, *Annu. Rep. Comput. Chem.*, **6**, 79–94 (2010). *Ab Initio* Electron Propagator Methods: Applications to Fullerenes and Nucleic Acid Fragments.

265. V. G. Zakrezewski, O. Dolgounitcheva, A. V. Zakjevskii, and J. V. Ortiz, *Adv. Quantum Chem.*, **62**, 105–136 (2011). *Ab Initio* Electron Propagator Calculations on Electron Detachment Energies of Fullerenes, Macrocyclic Molecules and Nucleotide Fragments.

266. O. Dolgounitcheva, V. G. Zakrzewski, and J. V. Ortiz, *Int. J. Quantum Chem.*, **112**, 184–194 (2012). *Ab Initio* Electron Propagator Calculations on Electron Detachment Energies of Nickel Phthalocyanine Tetrasulfonate Tetraanions.

267. G. Chałasiński and M. M. Szczęśniak, *Chem. Rev.*, **94**, 1723–1765 (1994). Origins of Structure and Energetics of van der Waals Clusters from ab Initio Calculations.

268. B. Jeziorski, R. Moszynski, and K. Szalewicz, *Chem. Rev.*, **94**, 1887–1930 (1994). Perturbation Theory Approach to Intermolecular Potential Energy Surfaces of van der Waals Complexes.

269. M. Gutowski, P. Skurski, K. D. Jordan, and J. Simons, *Int. J. Quantum Chem.*, **64**, 183–191 (1997). Energies of Dipole-Bound Anionic States.

270. J. M. Herbert and M. Head-Gordon, *Phys. Chem. Chem. Phys.*, **8**, 68–78 (2006). Accuracy and Limitations of Second-Order Many-Body Perturbation Theory for Predicting Vertical Detachment Energies of Solvated-Electron Clusters.

271. E. Fermi and E. Teller, *Phys. Rev.*, **72**, 399–408 (1947). The Capture of Negative Mesotrons in Matter.

272. A. D. Becke, *J. Chem. Phys.*, **98**, 1372–1377 (1993). A New Mixing of Hartree–Fock and Local Density-Functional Theories.

273. C. Lee, W. Yang, and R. G. Parr, *Phys. Rev. B*, **37**, 785–789 (1988). Development of the Colle-Salvetti Correlation-Energy Formula into a Functional of the Electron Density.

274. A. D. Becke, *Phys. Rev. A*, **38**, 3098–3100 (1988). Density-Functional Exchange-Energy Approximation with Correct Asymptotic Behavior.

275. J. Schirmer, *Phys. Rev. A*, **26**, 2395–2416 (1982). Beyond the Random-Phase Approximation: A New Approximation Scheme for the Polarization Propagator.

276. J. Schirmer, L. S. Cederbaum, and O. Walter, *Phys. Rev. A*, **28**, 1237–1259 (1983). New Approach to the One-Particle Green's Function for Finite Fermi Systems.

277. E. R. Davidson, S. A. Hagstrom, S. J. Chakravorty, V. M. Umar, and C. F. Fischer, *Phys. Rev. A*, **44**, 7071–7083 (1991). Ground-State Correlation Energies for Two- to Ten-Electron Atomic Ions.

278. G. K.-L. Chan and M. Head-Gordon, *J. Chem. Phys.*, **118**, 8551–8554 (2003). Exact Solution (within a Triple-Zeta, Double Polarization Basis Set) of the Electronic Schrödinger Equation for Water.

279. R. A. Kendall and H. A. Früchtl, *Theor. Chem. Acc.*, **97**, 158–163 (1997). The Impact of the Resolution of the Identity Approximate Integral Method on Modern ab Initio Algorithm Development.

280. H.-J. Werner, F. R. Manby, and P. J. Knowles, *J. Chem. Phys.*, **118**, 8149–8160 (2003). Fast Linear Scaling Second-Order Møller-Plesset Perturbation Theory (MP2) using Local and Density Fitting Approximations.

281. T. B. Pedersen, F. Aquilante, and R. Lindh, *Theor. Chem. Acc.*, **124**, 1–10 (2009). Density Fitting with Auxiliary Basis Sets from Cholesky Decomposition.

282. Y. Jung, A. Sodt, P. M. W. Gill, and M. Head-Gordon, *Proc. Natl. Acad. Sci. U.S.A.*, **102**, 6692–6697 (2005). Auxiliary Basis Expansions for Large-Scale Electronic Structure Calculations.

283. F. Weigend, M. Häser, J. Patzelt, and R. Ahlrichs, *Chem. Phys. Lett.*, **294**, 143–152 (1998). RI-MP2: Optimized Auxiliary Basis Sets and Demonstration of Efficiency.

284. R. Palangsuntikul, R. Polly, and B. Hartke, *Phys. Chem. Chem. Phys.*, **6**, 5456–5462 (2004). Global and Local Optimization of Auxiliary Basis Sets for RI-MP2 Calculations.

285. R. Polly, H.-J. Werner, F. R. Manby, and P. J. Knowles, *Mol. Phys.*, **102**, 2311–2321 (2004). Fast Hartree-Fock Theory using Local Density Fitting Approximations.

286. J. Bostrom, F. Aquilante, T. B. Pedersen, and R. Lindh, *J. Chem. Theory Comput.*, **5**, 1545–1553 (2009). Ab Initio Density Fitting: Accuracy Assessment of Auxiliary Basis Sets from Cholesky Decompositions.

287. R. P. Steele, R. A. DiStasio, Jr., Y. Shao, J. Kong, and M. Head-Gordon, *J. Chem. Phys.*, **125**(074108), 1–11 (2006). Dual-Basis Second-Order Møller-Plesset Perturbation Theory: A Reduced-Cost Reference for Correlation Calculations.

288. F. Weigend and R. Ahlrichs, *Phys. Chem. Chem. Phys.*, **1**, 4537–4550 (1999). *Ab Initio* Treatment of $(H_2O)_2^-$ and $(H_2O)_6^-$.

289. R. A. DiStasio, Jr. R. P. Steele, Y. M. Rhee, Y. Shao, and M. Head-Gordon, *J. Comput. Chem.*, **28**, 839–859 (2007). An Improved Algorithm for Analytical Gradient Evaluation in Resolution-of-the-Identity Second-Order Møller-Plesset Perturbation Theory: Application to Alanine Tetrapeptide Conformational Analysis.

290. J. Tomasi, B. Mennucci, and R. Cammi, *Chem. Rev.*, **105**, 2999–3093 (2005). Quantum Mechanical Continuum Solvation Models.

291. C. J. Cramer and D. G. Truhlar, *Acc. Chem. Res.*, **41**, 760–768 (2008). A Universal Approach to Solvation Modeling.

292. A. W. Lange and J. M. Herbert, *Chem. Phys. Lett.*, **509**, 77–87 (2011). Symmetric Versus Asymmetric Discretization of the Integral Equations in Polarizable Continuum Solvation Models.

293. D. M. Chipman, *Theor. Chem. Acc.*, **107**, 80–89 (2002). Comparison of Solvent Reaction Field Representations.

294. J. Tomasi, in *Continuum Solvation Models in Chemical Physics*, B. Mennucci and R. Cammi (Eds.), Wiley, Chichester, UK, 2007, pp. 1–28, Modern Theories of Continuum Models.

295. B. Mennucci, *WIREs Comput. Mol. Sci.*, **2**, 386–404 (2012). Polarizable Continuum Model.

296. J. D. Thompson, C. J. Cramer, and D. G. Truhlar, *J. Phys. Chem. A*, **108**, 6532–6542 (2004). New Universal Solvation Model and Comparison of the Accuracy of the SM5.42R, SM5.43R, C-PCM, D-PCM, and IEF-PCM Continuum Solvation Models for Aqueous and Organic Solvation Free Energies and for Vapor Pressures.

297. A. Klamt, B. Mennucci, J. Tomasi, V. Barone, C. Curutchet, M. Orozco, and F. J. Luque, *Acc. Chem. Res.*, **42**, 489–492 (2009). On the Performance of Continuum Solvation Methods. A Comment on "Universal Approaches to Solvation Modeling".

298. C. J. Cramer and D. G. Truhlar, *Acc. Chem. Res.*, **42**, 493–497 (2009). Reply to Comment on 'A Universal Approach to Solvation Modeling'.

299. A. V. Marenich, C. J. Cramer, and D. G. Truhlar, *J. Phys. Chem. B*, **113**, 4538–4543 (2009). Performance of SM6, SM8, and SMD on the SAMPL1 Test Set for the Prediction of Small-Molecule Solvation Free Energies.

300. A. Pomogaeva, D. W. Thompson, and D. M. Chipman, *Chem. Phys. Lett.*, **511**, 161–165 (2011). Modeling Short-Range Contributions to Hydration Energies with Minimal Parameterization.

301. R. A. Marcus, *J. Chem. Phys.*, **24**, 979–989 (1956). Electrostatic Free Energy and Other Properties of States Having Nonequilibrium Polarization. I.

302. M. M. Karelson and M. C. Zerner, *J. Phys. Chem.*, **96**, 6949–6957 (1992). Theoretical Treatment of Solvent Effects on Electronic Spectroscopy.

303. A. Klamt, *J. Phys. Chem.*, **100**, 3349–3353 (1996). Calculation of UV Vis Spectra in Solution.

304. H. Houjou, M. Sakurai, and Y. Inoue, *J. Chem. Phys.*, **107**, 5652–5660 (1997). Theoretical Evaluation of Medium Effects on Absorption Maxima of Molecular Solutes. I. Formulation of a New Method Based on the Self-Consistent Reaction Field Theory.

305. B. Mennucci, R. Cammi, and J. Tomasi, *J. Chem. Phys.*, **109**, 2798–2807 (1998). Excited States and Solvatochromatic Shifts within a Nonequilibrium Solvation Approach: A New

Formulation of the Integral Equation Formalism Method at the Self-Consistent Field, Configuration Interaction, and Multiconfiguration Self-Consistent Field Level.

306. M. Cossi and V. Barone, *J. Chem. Phys.*, **112**, 2427–2435 (2000). Solvent Effect on Vertical Electronic Transitions by the Polarizable Continuum Model.
307. M. Cossi and V. Barone, *J. Phys. Chem. A*, **104**, 10614–10622 (2000). Separation between Fast and Slow Polarizations in Continuum Solvation Models.
308. A. J. Cohen, P. Mori-Sanchez, and W. Yang, *Science*, **321**, 792–794 (2008). Insights into Current Limitations of Density Functional Theory.
309. P. Slavček, B. Winter, M. Faubel, S. E. Bradforth, and P. Jungwirth, *J. Am. Chem. Soc.*, **131**, 6460–6467 (2009). Ionization Energies of Aqueous Nucleic Acids: Photoelectron Spectroscopy of Pyrimidine Nucleosides and ab Initio Calculations.
310. J. P. Perdew and M. Ernzerhof, in *Electronic Density Functional Theory: Recent Progress and New Directions*, J. F. Dobson, G. Vignale, and M. P. Das (Eds.), Plenum, 1998, pp. 31–41, Density Functionals for Non-Relativistic Coulomb Systems.
311. R. Haunschild, T. M. Henderson, C. A. Jiménez-Hoyos, and G. E. Scuseria, *J. Chem. Phys.*, **133**, 134116:1–10 (2010). Many-Electron Self-Interaction and Spin Polarization Errors in Local Hybrid Density Functionals.
312. D. Lee and K. Burke, *Mol. Phys.*, **108**, 2687–2701 (2010). Finding Electron Affinities with Approximate Density Functionals.
313. M.-C. Kim, E.-J. Sim, and K. Burke, *J. Chem. Phys.*, **134**, 171103:1–4 (2011). Communication: Avoiding Unbound Anions in Density Functional Calculations.
314. J. P. Perdew and S. Kurth, in *Primer in Density Functional Theory*, C. Fiolhais, F. Nogueira, and M. A. L. Marques (Eds.), Vol. 620 of, *Lecture Notes in Physics*, Springer-Verlag, 2003, pp. 1–55, Density Functionals for Non-Relativistic Coulomb Systems in the New Century.
315. H. B. Shore, J. H. Rose, and E. Zaremba, *Phys. Rev. B*, **15**, 2858–2861 (1977). Failure of the Local Exchange Approximation in the Evaluation of the H^- Ground State.
316. K. Schwarz, *Chem. Phys. Lett.*, **57**, 605–607 (1978). Instability of Stable Negative Ions in the Xα Method or Other Local Density Functional Schemes.
317. F. Jensen, *J. Chem. Theory Comput.*, **6**, 2726–2735 (2010). Describing Anions by Density Functional Theory: Fractional Electron Affinity.
318. E. J. Baerends, O. V. Gritsenko, and R. van Meer, *Phys. Chem. Chem. Phys.*, **15**, 16408–16425 (2013). The Kohn–Sham Gap, the Fundamental Gap and the Optical Gap: The Physical Meaning of Occupied and Virtual Kohn–Sham Orbital Energies.
319. Y. Zhao, N. E. Schultz, and D. G. Truhlar, *J. Chem. Theory Comput.*, **2**, 364–382 (2006). Design of Density Functionals by Combining the Method of Constraint Satisfaction with Parameterization for Thermochemistry, Thermochemical Kinetics, and Noncovalent Interactions.
320. Y. Zhao and D. G. Truhlar, *Theor. Chem. Acc.*, **120**, 215–241 (2008). The M06 Suite of Density Functionals for Main Group Thermochemistry, Thermochemical Kinetics, Noncovalent Interactions, Excited States, and Transition Elements: Two New Functionals and Systematic Testing of Four M06-Class Functionals and 12 Other Functionals.
321. R. Peverati, Y. Zhao, and D. G. Truhlar, *J. Phys. Chem. Lett.*, **2**, 1991–1997 (2011). Generalized Gradient Approximation That Recovers the Second-Order Density-Gradient Expansion with Optimized Across-the-Board Performance.
322. R. Peverati and D. G. Truhlar, *J. Phys. Chem. Lett.*, **3**, 117–124 (2012). M11-L: A Local Density Functional That Provides Improved Accuracy for Electronic Structure Calculations in Chemistry and Physics.
323. A. W. Lange and J. M. Herbert, *J. Am. Chem. Soc.*, **131**, 3913–3922 (2009). Both Intra- and Interstrand Charge-Transfer Excited States in B-DNA are Present at Energies Comparable to, or Just above, the $^1\pi\pi^*$ Excitonic Bright States.
324. M. A. Rohrdanz, K. M. Martins, and J. M. Herbert, *J. Chem. Phys.*, **130**, 054112:1–8 (2009). A Long-Range-Corrected Density Functional That Performs Well for Both Ground-State

Properties and Time-Dependent Density Functional Theory Excitation Energies, Including Charge-Transfer Excited States.

325. R. Peverati and D. G. Truhlar, *J. Phys. Chem. Lett.*, **2**, 2810–2817 (2011). Improving the Accuracy of Hybrid Meta-GGA Density Functionals by Range Separation.
326. Y. Zhao and D. G. Truhlar, *J. Chem. Theory Comput.*, **4**, 1849–1868 (2008). Exploring the Limit of Accuracy of the Global Hybrid Meta Density Functional for Main-Group Thermochemistry, Kinetics, and Noncovalent Interactions.
327. R. Peverati and D. G. Truhlar, *J. Chem. Phys.*, **135**, 191102:1–4 (2011). Communication: A Global Hybrid Generalized Gradient Approximation to the Exchange-Correlation Functional That Satisfies the Second-Order Density-Gradient Constraint and Has Broad Applicability in Chemistry.
328. J. P. Perdew and A. Zunger, *Phys. Rev. B*, **23**, 5048–5079 (1981). Self-Interaction Correction to Density-Functional Approximations for Many-Electron Systems.
329. O. A. Vydrov and G. E. Scuseria, *J. Chem. Phys.*, **121**, 8187–8193 (2004). Effect of the Perdew-Zunger Self-Interaction Correction on the Thermochemical Performance of Approximate Density Functionals.
330. T. Frigato, J. VandeVondele, B. Schmidt, C. Schütte, and P. Jungwirth, *J. Phys. Chem. A*, **112**, 6125–6133 (2008). Ab Initio Molecular Dynamics Simulation of a Medium-Sized Water Cluster Anion: From an Interior to a Surface-Located Excess Electron via a Delocalized State.
331. O. Marsalek, F. Uhlig, T. Frigato, B. Schmidt, and P. Jungwirth, *Phys. Rev. Lett.*, **105**, 043002:1–4 (2010). Dynamics of Electron Localization in Warm Versus Cold Water Clusters.
332. M. d'Avezac, M. Calandra, and F. Mauri, *Phys. Rev. B*, **71**, 205210:1–5 (2005). Density Functional Theory Description of Hole-Trapping in SiO_2: A Self-Interaction-Corrected Approach.
333. J. VandeVondele and M. Sprik, *Phys. Chem. Chem. Phys.*, **7**, 1363–1367 (2005). A Molecular Dynamics Study of the Hydroxyl Radical in Solution Applying Self-Interaction-Corrected Density Functional Methods.
334. I. Frank, J. Hutter, D. Marx, and M. Parrinello, *J. Chem. Phys.*, **108**, 4060–4069 (1998). Molecular Dynamics in Low-Spin Excited States.
335. I. Okazaki, F. Sato, T. Yoshihiro, T. Ueno, and H. Kashiwagi, *J. Mol. Struct. (THEOCHEM)*, **451**, 109–119 (1998). Development of a Restricted Open Shell Kohn–Sham Program and Its Application to a Model Heme Complex.
336. M. Filatov and S. Shaik, *Chem. Phys. Lett.*, **304**, 429–437 (1999). A Spin-Restricted Ensemble-References Kohn-Sham Method and Its Application to Diradicaloid Situations.
337. M. Sodupe, J. Bertran, L. Rodrguez-Santiago, and E. J. Baerends, *J. Phys. Chem. A*, **103**, 166–170 (1999). Ground State of the $(H_2O)_2^+$ Radical Cation: DFT Versus Post-Hartree–Fock Method.
338. J. Gräfenstein, E. Kraka, and D. Cremer, *Phys. Chem. Chem. Phys.*, **6**, 1096–1112 (2004). Effect of the Self-Interaction Error for Three-Electron Bonds: On the Development of New Exchange-Correlation Functionals.
339. Y. A. Mantz, F. L. Gervasio, T. Laino, and M. Parrinello, *J. Phys. Chem. A*, **111**, 105–112 (2007). Charge Localization in Stacked Radical Cation DNA Base Pairs and the Benzene Dimer Studied by Self-Interaction Corrected Density-Functional Theory.
340. O. Marsalek, T. Frigato, J. VandeVondele, S. E. Bradforth, B. Schmidt, C. Schütte, and P. Jungwirth, *J. Phys. Chem. B*, **114**, 915–920 (2010). Hydrogen Forms in Water by Proton Transfer to a Distorted Electron.
341. H. Iikura, T. Tsuneda, T. Yanai, and K. Hirao, *J. Chem. Phys.*, **115**, 3540–3544 (2001). A Long-Range Correction Scheme for Generalized-Gradient-Approximation Exchange Functionals.
342. Y. Tawada, T. Tsuneda, S. Yanagisawa, T. Yanai, and K. Hirao, *J. Chem. Phys.*, **120**, 8425–8433 (2004). A Long-Range Corrected Time-Dependent Density Functional Theory.

343. J.-W. Song, T. Hirosawa, T. Tsuneda, and K. Hirao, *J. Chem. Phys.*, **126**, 154105:1–7 (2007). Long-Range Corrected Density Functional Calculations of Chemical Reactions: Redetermination of Parameter.

344. R. Baer, E. Livshits, and U. Salzner, *Annu. Rev. Phys. Chem.*, **61**, 85–109 (2010). Tuned Range-Separated Hybrids in Density Functional Theory.

345. T. M. Henderson, B. G. Janesko, and G. E. Scuseria, *J. Phys. Chem. A*, **112**, 12530–12542 (2008). Range Separation and Local Hybridization in Density Functional Theory.

346. A. Savin and H.-J. Flad, *Int. J. Quantum Chem.*, **56**, 327–332 (1995). Density Functionals for the Yukawa Electron–Electron Interaction.

347. T. Leininger, H. Stoll, H.-J. Werner, and A. Savin, *Chem. Phys. Lett.*, **275**, 151–160 (1997). Combining Long-Range Configuration Interaction with Short-Range Density Functionals.

348. R. D. Adamson, J. P. Dombroski, and P. M. W. Gill, *J. Comput. Chem.*, **20**, 921–927 (1999). Efficient Calculation of Short-Range Coulomb Energies.

349. T. M. Henderson, B. G. Janesko, and G. E. Scuseria, *J. Chem. Phys.*, **128**, 194105:1–9 (2008). Generalized Gradient Approximation Model Exchange Holes for Range-Separated Hybrids.

350. M. Chiba, T. Tsuneda, and K. Hirao, *J. Chem. Phys.*, **124**, 144106:1–11 (2006). Excited State Geometry Optimizations by Analytical Energy Gradient of Long-Range Corrected Time-Dependent Density Functional Theory.

351. T. Sato, T. Tsuneda, and K. Hirao, *J. Chem. Phys.*, **126**, 234114:1–12 (2007). Long-Range Corrected Density Functional Study on Weakly Bound Systems: Balanced Descriptions of Various Types of Molecular Interactions.

352. O. A. Vydrov, J. Heyd, A. V. Krukau, and G. E. Scuseria, *J. Chem. Phys.*, **125**, 074106:1–9 (2006). Importance of Short-Range Versus Long-Range Hartree-Fock Exchange for the Performance of Hybrid Density Functionals.

353. O. A. Vydrov and G. E. Scuseria, *J. Chem. Phys.*, **125**, 234109:1–9 (2006). Assessment of a Long-Range Corrected Hybrid Functional.

354. R. M. Richard and J. M. Herbert, *J. Chem. Theory Comput.*, **7**, 1296–1306 (2011). Time-Dependent Density-Functional Description of the ^1L_a State in Polycyclic Aromatic Hydrocarbons: Charge-Transfer Character in Disguise?

355. M. A. Rohrdanz and J. M. Herbert, *J. Chem. Phys.*, **129**, 034107:1–9 (2008). Simultaneous Benchmarking of Ground- and Excited-State Properties with Long-Range-Corrected Density Functional Theory.

356. A. W. Lange, M. A. Rohrdanz, and J. M. Herbert, *J. Phys. Chem. B*, **112**, 6304–6308 (2008). Charge-Transfer Excited States in a π-Stacked Adenine Dimer, as Predicted Using Lon-Range-Corrected Time-Dependent Density Functional Theory.

357. P. Mori-Sánchez, A. J. Cohen, and W. Yang, *J. Chem. Phys.*, **125**, 201201:1–4 (2006). Many-Electron Self-Interaction Error in Approximate Density Functionals.

358. L. D. Jacobson, C. F. Williams, and J. M. Herbert, *J. Chem. Phys.*, **130**, 124115:1–18 (2009). The Static-Exchange Electron–Water Pseudopotential, in Conjunction with a Polarizable Water Model: A New Hamiltonian for Hydrated-Electron Simulations.

359. T. Tsuneda, T. Suzumura, and K. Hirao, *J. Chem. Phys.*, **110**, 10664–10678 (2008). A New One-Parameter Progressive Colle–Salvetti-Type Correlation Functional.

360. J. P. Perdew and M. Levy, *Phys. Rev. B*, **56**, 16021–16028 (1997). Comment on "Significance of the Highest Occupied Kohn-Sham Eigenvalue".

361. M. E. Casida, *Phys. Rev. B*, **59**, 4694–4698 (1999). Correlated Optimized Effective-Potential Treatment of the Derivative Discontinuity and of the Highest Occupied Kohn-Sham Eigenvalue: A Janak-Type Theorem for the Optimized Effective-Potential Model.

362. T. Tsudeda, J.-W. Song, S. Suzuki, and K. Hirao, *J. Chem. Phys.*, **133**, 174101:1–9 (2010). On Koopmans' Theorem in Density Functional Theory.

363. E. Livshits, R. S. Granot, and R. Baer, *J. Phys. Chem. A*, **115**, 5735–5744 (2010). A Density Functional Theory for Studying Ionization Processes in Water Clusters.

364. K. U. Lao and J. M. Herbert, *J. Phys. Chem. Lett.*, **3**, 3241–3248 (2012). Accurate Intermolecular Interactions at Dramatically Reduced Cost: XPol+SAPT with Empirical Dispersion.

365. S. Jakobsen, K. Kristensen, and F. Jensen, *J. Chem. Theory Comput.*, **9**, 3978–3985 (2013). Electrostatic Potential of Insulin: Exploring the Limitations of Density Functional Theory and Force Field Methods.

366. M. F. Falcetta and K. D. Jordan, *J. Phys. Chem.*, **94**, 5666–5669 (1990). Assignments of the Temporary Anion States of the Chloromethanes.

367. M. F. Falcetta, Y. Choi, and K. D. Jordan, *J. Phys. Chem. A*, **104**, 9605–9612 (2000). Ab Initio Investigation of the Temporary Anion States of Perfluoroethane.

368. H.-Y. Cheng and C.-W. Chen, *J. Phys. Chem. A*, **115**, 10113–10121 (2011). Energy and Lifetime of Temporary Anion States of Uracil by Stabilization Method.

369. C.-Y. Juang and J. S.-Y. Chao, *J. Phys. Chem.*, **98**, 13506–13512 (1994). Splitting Energies of π^* Anion States of 1,4-Cyclohexadiene via the Exponent Stabilization Method.

370. J. Berdys, I. Anusiewicz, P. Skurski, and J. Simons, *J. Am. Chem. Soc.*, **126**, 6441–6447 (2004). Damage to Model DNA Fragments from Very Low-Energy (<1 eV) Electrons.

371. X. Li, M. D. Sevilla, and L. Sanche, *J. Am. Chem. Soc.*, **125**, 13668–13669 (2003). Density Functional Theory Studies of Electron Interaction with DNA: Can Zero eV Electrons Induce Strand Breaks?

372. I. Anusiewicz, J. Berdys, M. Sobczyk, P. Skurski, and J. Simons, *J. Phys. Chem. A*, **108**, 11381–11387 (2004). Effects of Base π-Stacking on Damage to DNA by Low-Energy Electrons.

373. T. Van Voorhis and M. Head-Gordon, *Mol. Phys.*, **100**, 1713–1721 (2002). A Geometric Approach to Direct Minimization.

374. P. Pulay, *Chem. Phys. Lett.*, **73**, 393–398 (1980). Convergence Acceleration of Iterative Sequences. The Case of SCF Iteration.

375. K. N. Kudin, G. E. Scuseria, and E. Cancès, *J. Chem. Phys.*, **116**, 8255–8261 (2002). A Black-Box Self-Consistent Field Convergence Algorithm: One Step Closer.

376. A. T. B. Gilbert, N. A. Besley, and P. M. W. Gill, *J. Phys. Chem. A*, **112**, 13164–13171 (2008). Self-Consistent Field Calculations of Excited States Using the Maximum Overlap Method (MOM).

377. N. A. Besley, A. T. B. Gilbert, and P. M. W. Gill, *J. Chem. Phys.*, **130**, 124308:1–7 (2009). Self-Consistent-Field Calculations of Core Excited States.

378. C. Zener, *Proc. R. Soc. London A*, **137**, 696–702 (1932). Non-Adiabatic Crossing of Energy Levels.

379. C. Wittig, *J. Phys. Chem. B*, **109**, 8428–8430 (2005). The Landau–Zener Formula.

380. E. E. Nikitin, *Annu. Rev. Phys. Chem.*, **50**, 1–21 (1999). Nonadiabatic Transitions: What We Learned from Old Masters and How Much We Owe Them.

381. W. Qian and S. Krimm, *J. Comput. Chem.*, **32**, 1025–1033 (1992). Vibrational Studies of the Disulfide Group in Proteins. VI. General Correlations of SS and CS Stretch Frequencies with Disulfide Bridge Geometry.

382. W. P. Reinhardt, *Annu. Rev. Phys. Chem.*, **33**, 223–255 (1982). Complex Coordinates in the Theory of Atomic and Molecular Structure and Dynamics.

383. E. Balslev and J. M. Combes, *Commun. Math. Phys.*, **22**, 280–294 (1971). Spectral Properties of Many-Body Schrödinger Operators with Dilatation-Analytic Interactions.

384. N. Moiseyev, *Phys. Rep.*, **302**, 211–293 (1998). Quantum Theory of Resonances: Calculating Energies, Widths and Cross-Sections by Complex Scaling.

385. N. Moiseyev, P. R. Certain, and F. Weinhold, *Mol. Phys.*, **36**, 1613–1630 (1978). Resonance Properties of Complex-Rotated Hamiltonians.

386. P. Žd'ánská and N. Moiseyev, *J. Chem. Phys.*, **123**, 194105:1–8 (2005). Hartree-Fock Orbitals for Complex-Scaled Configuration Interaction Calculation of Highly Excited Feshbach Resonances.

387. D. L. Yeager and M. K. Mishra, *Int. J. Quantum Chem.*, **104**, 871–879 (2005). Algebraic Modifications to Second Quantization for Non-Hermitian Complex Scaled Hamiltonians with Applications to a Quadratically Convergent Multiconfigurational Self-Consistent Field Method.

388. A. J. Krueger and N. T. Maitra, *Phys. Chem. Chem. Phys.*, **11**, 4655–4663 (2009). Autoionizing Resonances in Time-Dependent Density Functional Theory.

389. P. Elliott, S. Goldson, C. Canahui, and N. T. Maitra, *Chem. Phys.*, **391**, 110–119 (2011). Perspective on Double-Excitations in TDDFT.

390. C. W. McCurdy, Jr. and T. N. Rescigno, *Phys. Rev. Lett.*, **41**, 1364–1368 (1978). Extension of the Method of Complex Basis Functions to Molecular Resonances.

391. B. Simon, *Phys Lett. A.*, **71**, 211–214 (1979). The Definition of Molecular Resonance Curves by the Method of Exterior Complex Scaling.

392. N. Rom, E. Engdahl, and N. Moiseyev, *J. Chem. Phys.*, **93**, 3413–3419 (1990). Tunneling Rates in Bound Systems Using Smooth Exterior Complex Scaling within the Framework of the Finite Basis Set Approximation.

393. N. Moiseyev, *J. Phys. B*, **31**, 1431–1441 (1998). Derivations of Universal Exact Complex Absorption Potentials by the Generalized Complex Coordinate Method.

394. P. Balanarayan, Y. Sajeev, and N. Moiseyev, *Chem. Phys. Lett.*, **524**, 84–89 (2012). Ab-Initio Complex Molecular Potential Energy Surfaces by the Back-Rotation Transformation Method.

395. A. Ghosh, N. Vaval, and S. Pal, *J. Chem. Phys.*, **136**, 234110:1–6 (2012). Equation-of-Motion Coupled-Cluster Method for the Study of Shape Resonances.

396. E. Epifanovsky, I. Polyakov, B. Grigorenko, A. Nemukhin, and A. I. Krylov, *J. Chem. Theory Comput.*, **5**, 1895–1906 (2009). Quantum Chemical Benchmark Studies of the Electronic Properties of the Green Fluorescent Protein Chromophore. 1. Electronically Excited and Ionized States of the Anionic Chromophore in the Gas Phase.

397. A. Lange and J. M. Herbert, *J. Chem. Theory Comput.*, **3**, 1680–1690 (2007). Simple Methods to Reduce Charge-Transfer Contamination in Time-Dependent Density-Functional Calculations of Clusters and Liquids.

398. X. Chen and S. E. Bradforth, *Annu. Rev. Phys. Chem.*, **59**, 203–231 (2008). The Ultrafast Dynamics of Photodetachment.

399. A. Bernas, D. Grand, and E. Amouyal, *J. Phys. Chem.*, **84**, 1259–1262 (1980). Photoionization of Solutes and Conduction Band Edge of Solvents. Indole in Water and Alcohols.

400. A. U. Hazi and H. S. Taylor, *Phys. Rev. A*, **1**, 1109–1120 (1970). Stabilization Method of Calculating Resonance Energies: Model Problem.

401. C.-S. Chen, T.-H. Feng, and J. S.-Y. Chao, *J. Phys. Chem.*, **99**, 8629–8632 (1995). Stabilized Koopmans' Theorem Calculations on the π^* Temporary Anion States of Benzene and Substituted Benzenes.

402. M. Venuti and A. Modelli, *J. Chem. Phys.*, **113**, 2159–2167 (2000). Low-Energy Electron Attachment to Fused 1,4-Cyclohexadiene Rings by Means of Electron Transmission Spectroscopy and Exponent Stabilization Calculations.

403. K. D. Jordan, *Chem. Phys.*, **9**, 199–204 (1975). Construction of Potential Energy Curves in Avoided Crossing Situations.

404. A. D. Isaacson and D. G. Truhlar, *Chem. Phys. Lett.*, **110**, 130–134 (1984). Single-Root, Real-Basis-Function Method with Correct Branch-Point Structure for Complex Resonance Energies.

405. R. F. Frey and J. Simons, *J. Chem. Phys.*, **84**, 4462–4469 (1986). Resonance State Energies and Lifetimes via Analytic Continuation of Stabilization Graphs.

406. J. S.-Y. Chao, M. F. Falcetta, and K. D. Jordan, *J. Chem. Phys.*, **93**, 1125–1135 (1990). Application of the Stabilization Method to the $N_2^-(1\,^2\Pi_g)$ and $Mg^-(1\,^2P)$ Temporary Anion States.

407. K. Aflatooni, G. A. Gallup, and P. D. Burrow, *J. Phys. Chem. A*, **102**, 6205–6207 (1998). Electron Attachment Energies of the DNA Bases.

408. M. F. Falcetta and K. D. Jordan, *J. Phys. Chem.*, **113**, 2903–2999 (1991). Stabilization Calculations on the π^* Anion States of 1,4-Cyclohexadiene: Confirmation of the π^*_- and π^*_+ Orbital Ordering.

409. H.-Y. Cheng, C.-W. Chen, J.-T. Chang, and C.-C. Shih, *J. Phys. Chem. A*, **115**, 84–93 (2011). Application of the Stabilization Method to Temporary Anion States of CH_3CN, CH_3NC, CH_3SCN, and CH_3NCS in Density Functional Theory with Asymptotically Corrected Potentials.

410. J.-D. Chai and M. Head-Gordon, *Phys. Chem. Chem. Phys.*, **10**, 6615–6620 (2008). Long-Range Corrected Hybrid Density Functionals with Damped Atom–Atom Dispersion Corrections.

411. S. Grimme, *J. Chem. Phys.*, **124**, 034108:1–16 (2006). Semiempirical Hybrid Density Functional with Perturbative Second-Order Correction.

412. B. Nestmann and S. D. Peyerimhoff, *J. Phys. B*, **18**, 615–626 (1985). Calculation of the Discrete Component of Resonance States in Negative Ions by Variation of Nuclear Charges.

413. B. M. Nestmann and S. D. Peyerimhoff, *J. Phys. B*, **18**, 4309–4319 (1985). CI Method for Determining the Location and Width of Resonances in Electron–Molecule Collision Processes.

414. A. Whitehead, R. Barrios, and J. Simons, *J. Chem. Phys.*, **116**, 2848–2851 (2002). Stabilization Calculation of the Energy and Lifetime of Metastable SO_4^{2-}.

415. K. M. Ervin, I. Anusiewicz, P. Skurski, J. Simons, and W. C. Lineberger, *J. Phys. Chem. A*, **107**, 8521–8529 (2003). The Only Stable State of O_2^- is the $X\,^2\Pi_g$ Ground State and It (Still!) Has an Adiabatic Electron Detachment Energy of 0.45 eV.

416. S. Feuerbacher, T. Sommerfeld, and L. S. Cederbaum, *J. Chem. Phys.*, **121**, 6628–6633 (2004). Extrapolating Bound State Data of Anions into the Metastable Domain.

417. A. Modelli, A. Foffani, M. Guerra, D. Jones, and G. Distefano, *Chem. Phys. Lett.*, **99**, 58–65 (1983). Electron Transmission Spectroscopy and MSXα Study of Closed-Shell and Open-Shell Metallocenes.

418. M. Guerra, *J. Phys. Chem.*, **94**, 8542–8547 (1990). Boxing Procedure for Estimating Shape Resonance Energies from Stabilization Graphs with the MSXα Method.